



A MULTIREFERENCE DENSITY FUNCTIONAL
APPROACH TO THE CALCULATION OF THE EXCITED
STATES OF URANIUM IONS

DISSERTATION

Eric V. Beck, Major, USAF

AFIT/DS/ENP/07-01

DEPARTMENT OF THE AIR FORCE
AIR UNIVERSITY

AIR FORCE INSTITUTE OF TECHNOLOGY

Wright-Patterson Air Force Base, Ohio

APPROVED FOR PUBLIC RELEASE; DISTRIBUTION UNLIMITED.

The views expressed in this thesis are those of the author and do not reflect the official policy or position of the United States Air Force, Department of Defense, or the United States Government.

AFIT/DS/ENP/07-01

A MULTIREFERENCE DENSITY FUNCTIONAL
APPROACH TO THE CALCULATION OF THE EXCITED
STATES OF URANIUM IONS

DISSERTATION

Presented to the Faculty
Department of Engineering Physics
Graduate School of Engineering and Management
Air Force Institute of Technology
Air University
Air Education and Training Command
In Partial Fulfillment of the Requirements for the
Degree of Doctor of Philosophy

Eric V. Beck, B.S., M.S.

Major, USAF

March 2007

APPROVED FOR PUBLIC RELEASE; DISTRIBUTION UNLIMITED.

A MULTIREFERENCE DENSITY FUNCTIONAL
APPROACH TO THE CALCULATION OF THE EXCITED
STATES OF URANIUM IONS

Eric V. Beck, B.S., M.S.

Major, USAF

Approved:

Larry W. Burggraf (Chairman)

Date

Jean-Philippe Blaudeau (Member)

Date

Eric A. Stahlberg (Member)

Date

David E. Weeks (Member)

Date

William P. Baker (Member)

Date

Anthony N. Palazotto
(Dean's Representative)

Date

Accepted:

Marlin U. Thomas
Dean, Graduate School of Engineering and Management

Date

Abstract

An accurate and efficient hybrid Density Functional Theory (DFT) and Multireference Configuration Interaction (MRCI) model for computing electronic excitation energies in atoms and molecules was developed. The utility of a hybrid method becomes apparent when ground and excited states of large molecules, clusters of molecules, or even moderately sized molecules containing heavy element atoms are desired. In the case of large systems of lighter elements, the hybrid method brings to bear the numerical efficiency of the DFT method in computing the electron-electron dynamic correlation, while including non-dynamical electronic correlation via the Configuration Interaction (CI) calculation. Substantial reductions in the size of the CI expansion necessary to obtain accurate spectroscopic results are possible in the hybrid method. Where heavy element compounds are of interest, fully relativistic calculations based upon the Dirac Hamiltonian rapidly become computationally prohibitive, as the basis set requirements in four-component calculations increase by a factor of two or more in order to satisfy kinetic balance between the large electronic components and small positronic components, while the size of the MRCI Hamiltonian quadruples with respect to a non-relativistic calculation. In this hybrid method, applications to heavy element compounds such as bromine and uranium were accomplished through the use of relativistic effective core potentials, allowing for the first time both scalar relativistic and spin-orbit effect treatment necessary for the accurate calculation of electronic excitation energies in heavy elements in a Density Functional Theory Multireference Configuration Interaction Hybrid Model (DFT/MRCI) method. This implementation of the original hybrid method, developed by Grimme and Waletzke, was modified to remove inherent spin-multiplicity limitations, as well as reduce the number of free parameters used in the method from five to three.

The DFT portion of the hybrid method used 100% Hartree-Fock (HF) exchange and an electron correlation-only density functional as the basis for a modified Graphical Unitary Group Approach (GUGA) based CI calculation. The CI algorithm was modified to exponentially scale the off-diagonal matrix elements of the CI Hamiltonian in order to reduce the double counting of electronic correlation computed by both the DFT correlation functional and the CI calculation. The scaling applied to the interaction between states in the CI calculation exponentially decreased to zero as the energy difference between states grew. This algorithm left interactions between degenerate or nearly degenerate states unscaled, while rapidly scaling to zero interactions between states widely separated in energy.

The two empirical parameters which controlled this off-diagonal matrix element scaling were determined through the use of a training set of light atoms and molecules consisting of H₂, He, Li, Be, B, C, N, O, F, Ne, and Be₂. The average DFT/MRCI errors with respect to exact Full Configuration Interaction (FCI) results on this training set was 9.0559 milli Hartrees (mH) over 11 atomic and molecular systems. CI expansion length tailoring through virtual orbital freezing. Consistently favorable results were obtained when virtual orbitals 30-40 electron Volts (eV) above the highest occupied molecular orbital were frozen, providing the best trade off between method accuracy and reduction in CI expansion length. Using this approach to paring the CI expansion length, reductions in the size of the CI expansions of a factor of 25-64 were achieved.

The values of the two off-diagonal scaling parameters were determined by minimizing the average absolute error between the DFT/MRCI and exact FCI calculations for all test atoms and molecules combined. The values of the parameters obtained for the 100% HF exchange and Perdew Burke and Ernzerhof (PBE) 1996 Generalized Gradient Approximation (GGA) correlation functional combination were $p_1=0.96$ and $p_2=2.5$.

After the scaling parameters were determined using the training suite of atoms and molecules, the method was applied to carbon monoxide, boron fluoride, the bromine atom, the uranium 5+ and 4+ ions, and the uranyl (UO_2^{2+}) ion. In all cases, the correct ordering of ground and excited states was obtained using the DFT/MRCI model. In CO, a reduction in overall error of 26% with respect to Time Dependent Density Functional Theory (TDDFT) was observed over 6 ground and excited states. A reduction in overall error of 42% with respect to TDDFT was observed in 5 ground and excited states of BF, while an accuracy with respect to experiment of 11-22% for electronic excitation energies for the first excited states of the bromine atom and uranium 5+ and 4+ ions was observed. Final application of the model to the uranyl ion compared favorably with observed uranyl fluorescent series in crystals, and was obtained with an order of magnitude reduction in the computational effort with respect to a traditional, wave function based quantum chemistry approach.

Acknowledgements

Many people, my wife and family especially, are directly responsible for my successes here at AFIT, in my career, and in my life. While the list is far too long to mention each individual specifically, rest assured, your presence in my life was and is appreciated.

Eric V. Beck

Table of Contents

	Page
Abstract	iv
Acknowledgements	vii
List of Figures	xi
List of Tables	xiii
I. Introduction	1
1.1 Statement of Problem	4
1.2 Research Objectives	10
1.3 Boundary Conditions	10
1.4 Research Overview	11
II. Uranium Ion Calculations	13
2.1 Relativistic Effects in Chemistry	15
2.2 Theory	18
2.2.1 The Dirac Equation	19
2.2.2 Relativistic Effective Core Potentials	23
2.2.3 Basis Sets for Use with Shape-consistent RECPs	25
2.3 Methodology	26
2.3.1 Selection of the Reference Space	28
2.4 Results	29
2.5 Analysis	34
III. The COLUMBUS-based DFT/MRCI Model	38
3.1 Theory	38
3.1.1 Non-relativistic Quantum Theory	38
3.1.2 The Kohn-Sham Approach to DFT	41
3.1.3 Configuration Interaction and the Graphical Unitary Group Approach	45
3.1.4 Hybrid DFT/MRCI Model	58
3.2 DFT/MRCI Model Implementation with COLUMBUS	66
3.2.1 Density Functional Theory Interface to COLUMBUS	67
3.2.2 Correlation Energy in the Repartitioned Hamiltonian	75
3.2.3 CIUDG Based DFT/MRCI	76

	Page	
3.2.4	Testing the DFT/MRCI Model Implementation within CIUDG	83
3.3	Using the COLUMBUS DFT/MRCI Model	87
3.4	Results and Analysis	94
3.4.1	Carbon Monoxide	94
3.4.2	Boron Fluoride	97
3.4.3	Bromine Atom	99
3.4.4	Uranium +5 Ion	102
3.4.5	Uranium +4 Ion	104
3.4.6	Uranyl Ion, UO_2^{2+}	106
IV.	Conclusions	109
4.1	Uranium Shape-Consistent RECP Accuracy Assessment	109
4.2	DFT/MRCI Model	112
4.3	Research Objective Successes and Failures	120
4.4	Future Work	124
4.4.1	DFT/MRCI with Other Correlation Density Functionals	124
4.4.2	Integration of DFT Within SCFPQ using Abelian Point Groups	125
4.4.3	Hybrid Exchange-Correlation Density Functional Implementation	126
4.4.4	Investigations into the Theoretical Basis of the DFT/MRCI Method	127
4.5	Summary	128
Appendix A.	List of Acronyms	131
Appendix B.	DFT/MRCI Damping Parameter Selection	133
B.1	Hydrogen Molecule, cc-pVDZ Basis	134
B.2	Hydrogen Molecule, cc-pVTZ Basis	136
B.3	Helium Atom, cc-pVDZ Basis	138
B.4	Helium Atom, cc-pVTZ Basis	140
B.5	Lithium Atom, cc-pVDZ Basis	142
B.6	Lithium Atom, cc-pVTZ Basis	144
B.7	Beryllium Atom, cc-pVDZ Basis	147
B.8	Beryllium Atom, cc-pVTZ Basis	150
B.9	Boron Atom, cc-pVDZ Basis	152
B.10	Carbon Atom, cc-pVDZ Basis	156
B.11	Nitrogen Atom, cc-pVDZ Basis	159
B.12	Oxygen atom, cc-pVDZ Basis set	162

List of Figures

Figure		Page
1.	Distinct Row Table Graph for Multi Reference Single and Double Excitation Configuration Interaction Expansion [122]	49
2.	One Body Loop Segments [124]	56
3.	Non-zero Loop Contributions to the CI Hamiltonian [120, 92]	57
4.	Eigenvalue Symmetry Breaking in Two-electron Spin Coupling Example	64
5.	Effect of Exponent on Eigenvalue	64
6.	Density Plot of Absolute Error Between Exact ΔE and Damped ΔE	66
7.	DFT/MRCI Averaged, Absolute Error with Respect to Full Configuration Interaction Results (mH)	93
8.	H ₂ cc-pVDZ basis DFT/MRCI Absolute Error (mH) with Respect to FCI Results	135
9.	H ₂ cc-pVTZ basis DFT/MRCI Absolute Error (mH) with Respect to FCI Results	137
10.	He Atom, cc-pVDZ basis DFT/MRCI Absolute Error (mH) with Respect to FCI Results	139
11.	He Atom, cc-pVTZ Basis DFT/MRCI Absolute Error (mH) with Respect to FCI Results	141
12.	Li Atom, cc-pVDZ Basis DFT/MRCI Absolute Error(mH) with Respect to FCI Results	143
13.	Li Atom, cc-pVTZ Basis DFT/MRCI Absolute Error (mH) with Respect to FCI Results	146
14.	Be Atom, cc-pVDZ Basis DFT/MRCI Absolute Error (mH) with Respect to FCI Results	149
15.	Be Atom, cc-pVTZ Basis DFT/MRCI Absolute Error (mH) with Respect to FCI Results	152

Figure	Page
16. B Atom, cc-pVDZ Basis DFT/MRCI Absolute Error (mH) with Respect to FCI Results	155
17. C Atom, cc-pVDZ Basis DFT/MRCI Absolute Error (mH) with Respect to FCI Results	158
18. N Atom, cc-pVDZ Basis DFT/MRCI Absolute Error (mH) with Respect to FCI Results	161
19. O Atom, cc-pVDZ Basis DFT/MRCI Absolute Error (mH) with Respect to FCI Results	164
20. F Atom, cc-pVDZ Basis DFT/MRCI Absolute Error (mH) with Respect to FCI Results	166
21. Ne Atom, cc-pVDZ Basis DFT/MRCI Absolute Error (mH) with Respect to FCI Results	168
22. Be Dimer, cc-pVDZ Basis DFT/MRCI Absolute Error (mH) with Respect to FCI Results	171
23. Uranium cc-pVDZ 68 Electron RECP 3 <i>sd</i> and Converted 1 <i>s</i> Orbitals	175
24. Uranium cc-pVDZ 68 Electron RECP 3 <i>sd</i> and Converted 1 <i>s</i> Orbital Radial Probability Densities	175
25. Uranium cc-pVDZ 68 Electron RECP 3 <i>sd</i> and Converted 1 <i>s</i> Radial Probability Density Difference	176

List of Tables

Table		Page
1.	Valence Electrons Included in Uranium PAC-RECPs	28
2.	Basis Sets for Use With Uranium PAC-RECPs	28
3.	U ⁵⁺ Results, 5 <i>f</i> ¹ Reference Space	30
4.	U ⁵⁺ Results, (5 <i>f</i> 6 <i>d</i>) ¹ Reference Space	30
5.	U ⁴⁺ Results, 5 <i>f</i> ² Reference Space	32
6.	U ⁴⁺ Results,(5 <i>f</i> 6 <i>d</i>) ² Reference Space	33
7.	U ⁴⁺ Ionization Potential, 5 <i>f</i> ^{<i>n</i>} References	33
8.	U ⁴⁺ Ionization Potential, (5 <i>f</i> 6 <i>d</i>) ^{<i>n</i>} References	34
9.	Optimized DFT/MRCI Parameters for the BHLYP Functional for Singlet and Triplet States [63]	60
10.	SCFPQ + <i>V_{xc}</i> and NWChem DFT Energies, CPBE96 Correlation Functional	74
11.	DFT/MRCI Testing Cases	85
12.	Testing Results	86
13.	Carbon Monoxide cc-pVTZ DFT/MRCI Results	96
14.	BF cc-pVTZ DFT/MRCI Results	98
15.	Bromine Atom cc-pVTZ DFT/MRCI Results	101
16.	U ⁵⁺ DFT/MRCI Results, (5 <i>f</i> 6 <i>d</i>) ¹ Reference Space	103
17.	U ⁴⁺ DFT/MRCI and MR-SOCISD Results, 5 <i>f</i> ² Reference Space	104
18.	UO ₂ ²⁺ DFT/MRCI results	106
19.	UO ₂ ²⁺ Calculated and Measured Fluorescent Series	107
20.	MR-CISD Hartree-Fock Configuration Coefficients For Systems Used for Damping Parameter Determination	133
21.	Hydrogen Molecule, cc-pVDZ Basis Set, Full CI Results	134
22.	DFT/MRCI Error Analysis for Hydrogen Molecule, cc-pVDZ Basis	134
23.	Full CI Results for Hydrogen Molecule, cc-pVTZ Basis	136
24.	DFT/MRCI Error Analysis for Hydrogen Molecule, cc-pVTZ Basis	137
25.	Full CI Results for Helium Atom, cc-pVDZ Basis	138
26.	DFT/MRCI Error Analysis for Helium Atom, cc-pVDZ Basis	139
27.	Full CI Results for Helium Atom, cc-pVTZ Basis	140
28.	DFT/MRCI Error Analysis for Helium Atom, cc-pVTZ Basis	141

Table	Page
29. Full CI Results for Lithium Atom, cc-pVDZ Basis	142
30. DFT/MRCI Error Analysis for Li Atom, cc-pVDZ Basis	143
31. Full CI Results for Lithium Atom, cc-pVTZ Basis	145
32. DFT/MRCI Error Analysis for Li Atom, cc-pVTZ Basis	145
33. Full CI Results for Beryllium Atom, cc-pVTZ Basis	147
34. DFT/MRCI Error Analysis for Be Atom, cc-pVDZ Basis	148
35. Full CI Results for Beryllium Atom, cc-pVTZ Basis	150
36. DFT/MRCI Error Analysis for Be Atom, cc-pVTZ Basis	151
37. Full CI Results for Boron Atom, cc-pVDZ Basis	153
38. DFT/MRCI Error Analysis for Boron Atom, cc-pVDZ Basis	154
39. Full CI results for Carbon Atom, cc-pVDZ Basis	157
40. DFT/MRCI Error Analysis for Carbon Atom, cc-pVDZ Basis	157
41. Full CI Results for Nitrogen Atom, cc-pVDZ Basis	159
42. DFT/MRCI Error Analysis for Nitrogen Atom, cc-pVDZ Basis	160
43. Full CI Results for Oxygen Atom, cc-pVDZ Basis	162
44. DFT/MRCI Error Analysis for Oxygen Atom, cc-pVDZ Basis	163
45. Full CI Results for Fluorine Atom, cc-pVDZ Basis	165
46. DFT/MRCI Error Analysis for Fluorine Atom, cc-pVDZ Basis	165
47. Full CI Results for Neon Atom, cc-pVDZ Basis	167
48. DFT/MRCI Error Analysis for Neon Atom, cc-pVDZ Basis	167
49. Full CI Results for Beryllium Dimer, cc-pVDZ Basis	169
50. DFT/MRCI Error Analysis for Beryllium Dimer, cc-pVDZ Basis	170
51. U ⁵⁺ Results From Both 3 <i>sd</i> and 1 <i>s</i> Converted Basis Set, 5 <i>f</i> ¹ Reference Space	178
52. U ⁵⁺ Results From Both 3 <i>sd</i> and 1 <i>s</i> Converted Basis Set, (5 <i>f</i> 6 <i>d</i>) ¹ Reference Space	179

A MULTIREFERENCE DENSITY FUNCTIONAL APPROACH TO THE CALCULATION OF THE EXCITED STATES OF URANIUM IONS

I. Introduction

Actinide chemistry, in particular, the chemistry of uranium, continues to be of intense interest in many applications. Design, performance, aging, and disposal of nuclear fuel components, the environmental transport of uranium compounds lingering in mines and ore processing waste, as well as material delivered through depleted uranium munitions all require a thorough understanding of the chemistry of uranium. Furthermore, the nuclear weapon stockpile stewardship program¹ demands a thorough understanding of the processes by which uranium components age, as well as the effect aging has on the reliability and performance of nuclear weapons. A cornerstone of the stockpile stewardship program is theoretical modeling and simulation of the basic physics and chemistry involved in the design, manufacture, maintenance, and operation of a nuclear weapon. Non-invasive electronic spectroscopic methods may be used to diagnose the extent of nuclear weapon component aging [66].

Of particular importance in the underlying chemistry of these uranium compounds is the oxidation state of the uranium atom. Uranium, like most early actinides, can possess a wide range of oxidation states, ranging from +3 to +6, due in part to chemical activation of the uranium $5f$ orbitals via relativistic effects which will be described shortly. The oxidation state of uranium can be influenced by its local chemical environment, which in turn influences the geometry of the uranium oxide compounds. The uranium oxidation state can be inferred through spectroscopic measurements studies, which are useful in nuclear forensics and environmental monitoring.

¹<http://www.nrsa.doe.gov/>

Structural studies performed using x-ray or neutron diffraction on uranates concur that uranium oxides tend to occur in either an elongated or flattened octahedral geometry in uranium compounds. The consensus of these studies show that uranyl-like configurations dominate, where the tightly bound, linear UO_2^{2+} ion is present, surrounded by three to five equatorial ligands, with axial uranium-oxygen bonds lengths ranging from 1.7-2.0 Å. Equatorial bond lengths cluster in the range of 2.0-2.4 Å, depending on the ligand species [40] [49] [27] [38] [128] [134] [116] [141]. Particularly thorough reviews of the structure of uranium oxide are given in papers by Burns *et al* [26] [27], Miller [89], and by Katz [75] as well as in the Gmelin Handbook [29] and Rabinowitch [111]. Rare distorted tetrahedral configurations of uranium oxides have been reported, with uranium-oxygen bond lengths on the order of 1.9 Å [69].

X-ray photoelectron spectroscopy, a particular method of high energy electronic spectroscopy, provides insight into the electronic structure of these uranium oxides, however, the resolution to probe, in detail, the electronic structure of the valence region below 5 eV makes such methods insensitive to uranium bonding. Despite this lack of sensitivity, x-ray photoelectron studies have proven useful in probing the electronic structure of inner valence and core-like electrons in uranium oxide compounds [60] [132] [44] [133]. Electronic transition energies to and from the uranium $5d$, $6p$, and $6s$ levels are typically probed in these studies, yielding insight into the nature of these higher energy transitions.

Most insight into lower energy valence transitions in uranium oxides, where photoluminescence originates, has been gained from electronic photoluminescence measurements of uranium doped crystal studies. It is in the valence region where x-ray studies lack the sensitivity or resolution to fully characterize the electronic structure of the bonding. In these crystal studies, a distorted octahedral coordination with a tightly bound, central, linear uranyl ion is typically found [84] [129] [130] [5] [22] [18] [19] [93] [80]. Photoluminescence in these compounds, attributed to ligand to metal charge transfer transitions from uranium in a +6 oxidation state to oxygen ligands results in a yellow-green fluorescence peaking at 18,000 to 21,000 cm^{-1} . Crystal field

and ligand effects lead to relatively modest perturbations to this fluorescence spectra, typically on the order of 1000 cm^{-1} . Lifetimes vary, but are typically of the order of microseconds. Excellent overviews are contained in [61] [29] and [111]. One of the most detailed analyses of the electronic and vibrational spectra of the uranyl ion was performed by Denning based on a series of experimental work performed in the 1970s [43] [45] [42]. In his study, Denning verified earlier analysis [111] that the linear uranyl ion is particularly stable, with bond dissociation energies for the uranyl ion of 700 kilo Joule (kJ) per mole. He also finds that the uranyl ion is chemically inert. Isotopic oxygen exchange in uranyl has a lifetime of over 40,000 hours. Denning's examination of uranyl spectra in CsUO_2Cl_4 show that the $5f$ electron shell lies below the $6d$, with f and d separation increasing as with increasing uranium oxidation state. The uranium $5f$ shell is responsible for most of the ligand interactions, and the nature of the characteristic green-yellow luminescence in uranium compounds appears to be from the presence of low-lying, non-bonding orbitals in the $5f$ shell. Denning's examination of the polarized, low temperature crystal spectroscopy shows that the luminescence origins can be attributed to the first two bands in the absorption spectra, and that the the low-lying excited states have even parity. Transitions from these even-parity excited states to the even-parity ground state are parity forbidden, and thus are magnetic dipole or electric quadrupole transitions [41]. A few studies [99] [94] report a red luminescence which is attributed to fluorescence originating from a distorted tetrahedral coordination of uranium with energies in the neighborhood of $15,000\text{ cm}^{-1}$.

More recently, laser spectroscopic techniques have been applied to the analysis of uranium oxides. Time resolved laser induced fluorescence characterization of uranium contamination at Hanford was performed by Wang *et al* [136]. Additionally, laser spectroscopy studies on uranium in frozen matrices have been performed by Lue [83] and [3].

1.1 *Statement of Problem*

While there is a large amount of experimental data on the various thermo chemical properties of uranium [75] [137], theoretical modeling of the spectra of this element has progressed more slowly. *Ab initio* quantum mechanical theoretical techniques have made great strides in understanding molecules consisting of lighter elements, and computational methods have been quite successful in predicting thermodynamic and spectroscopic properties of these compounds. There are two main reasons for this disproportionate difficulty in predicting the electronic spectra for heavy element compounds.

The first difficulty is that relativistic effects for actinides are significant enough that perturbation treatments are inadequate, thus requiring a method that incorporates these effects throughout the calculation. This is in stark contrast to lighter molecules where relativistic effects can be neglected in all but high-precision theoretical calculations [108, 3787-3788] [7, 1-27].

There are three main relativistic effects in atomic and molecular chemistry, each roughly the same magnitude, all of which scale approximately as Z^4 , where Z is the nuclear charge [108]. The first main relativistic effect is considered a direct effect, consisting of a radial contraction of atomic orbitals, along with a stabilization of the energy level of the electronic state. This effect is due primarily to the relativistic mass increase as electron velocities near the nucleus become appreciable fractions of the speed of light. Electron orbitals having high densities near the nucleus, where electron speeds are largest, experience the largest contraction. For example, in uranium this relativistic contraction is roughly 26% when compared with the non-relativistic Bohr radius. All atomic orbitals have some density near the nucleus, therefore, all atomic orbitals experience some contraction. However, the inner s - and p - orbitals nearest the nucleus experience the most contraction [108]. In light-element molecules, this orbital contraction is small and negligible in all but the highest precision calculations, but the effect becomes large in actinide elements such as uranium. The

second relativistic effect is an indirect effect, and it consists of a radial expansion and destabilization in the electronic energy levels of outer atomic orbitals. This is due to increased effective nuclear charge screening by the inner, contracted orbitals, reducing the effective nuclear charge experienced by the outer electrons. Additionally, relativistic contraction of the inner s - and p - electron shells increase the electron density near the nucleus, crowding out the outer d - and f - electron shells. This is due to the fact that there is a decrease in electron density near the nucleus for orbitals with increasing orbital angular momentum. Thus, the direct orbital contraction competes with the indirect orbital expansion. The orbital expansions and contractions can affect bond lengths and force constants [108], which in turn affect molecular vibrational frequencies. The final relativistic effect that falls naturally out of the Dirac Lorentz covariant theory for the electron, described in more detail in chapter two, is spin-orbit splitting of states. Spin-orbit splitting of states is responsible for the most pronounced deviations of heavy elements in the period table from lighter elements in the same column. The yellowish color of gold, while silver is colorless is one striking example. Silver, a lighter element with less pronounced relativistic effects, has an absorption spectra in the ultraviolet, while gold, a heavier element, has an absorption spectra in the visible spectrum, a direct result of a combination of all three relativistic effects. The inert pair effect observed in the ionization potential of lead versus tin is another example of spin-orbit splitting producing chemically relevant effects. In lead the relativistic effects stabilize and split the $6p$ electron shell into a $6p_{\frac{1}{2}}$ and a $6p_{\frac{3}{2}}$ shell, resulting in a full and relatively inert $6p_{\frac{1}{2}}$ shell. The effect is much less pronounced in tin, resulting in a much lower ionization potential.

For lighter elements, relativistic effects are typically done through perturbative corrections based on the Dirac covariant theory of the electron to the non-relativistic solutions to the Schrödinger equation, because the magnitude of the relativistic effects for elements in the first two rows are small. For these lighter elements, the electron-electron interactions are much larger than the relativistic corrections, which accounts for the success of perturbative approaches. Unfortunately, such perturbative methods

fail on heavy elements such as uranium, as the relativistic effects can be of the same magnitude as the electron-electron interaction. Successfully incorporating relativistic effects in heavy element calculations are all based on solving the fully-relativistic, many electron Dirac equation. Because the Dirac theory results in a coupling between the electron and positron, each with two spin components, the wave function involved is four dimensional for a one-electron system, and $4N$ dimensional for a N electron system. State-of-the-art calculations using the full Dirac model involve single heavy atoms, or very small molecules, and at present are incapable of computing excited states of these systems, because such calculations require multi reference methods which rapidly become computationally prohibitive within a four-component fully relativistic framework. One additional complication in using a fully-relativistic Dirac model for computational chemistry is that there must be kinetic balance between the electronic and positronic basis sets. The reason for this is that the electronic and positronic components in the Dirac four-component model are not independent, but they are related by the expression

$$\psi_{SC} = \frac{\vec{\sigma} \cdot \vec{p}}{E + m} \psi_{LC}, \quad (1)$$

where ψ_{SC} and ψ_{LC} are the small and large component wave functions, respectively, $\vec{\sigma}$ is a Pauli spin-matrix, \vec{p} is the momentum, E is the total energy and m is the electron rest mass. The speed of light in Equation 1 is set to unity. The result of this kinetic-balance requirement is that for every basis electronic basis function used, there needs to be at least two positronic basis functions, one with angular momentum quantum number $L + 1$ and one with angular momentum quantum number $L - 1$. Thus, a four-component, fully relativistic calculation uses a basis set three times larger than a corresponding, non-relativistic calculation.

A second computational difficulty is the sheer number of electrons to deal with in actinide compounds. Common uranium oxide compounds such as UO_2 have 108 electrons, while more complex oxides such as U_3O_8 has 340 electrons. The most common

approach for calculating excited states of atoms and molecules is CI, which will be discussed in more detail in chapter three. Briefly, CI is a computational method where the electronic wave function is expanded in terms of an orbital basis that includes both ground and excited state electronic configurations. By including all possible combinations of electron occupation in the orbital expansion basis, a FCI calculation is achieved, which is an exact solution to the non-relativistic Schrödinger wave equation within the approximation of the finite basis set. Despite this fact, CI has some serious limitations, namely, that CI calculations quickly scale to computational impracticality on modern computers. For a calculation with K basis functions and N electrons, the FCI calculation scales roughly as $(\frac{2K}{N})^N$ [127]. Taking the U_3O_8 example with $N = 340$ and a modest, cc-pVDZ basis set with two contracted basis functions per shell results in 196 electronic basis functions. Kinetic balance requirements add an additional 392 positronic basis functions, for a total of $K = 588$ basis functions. Thus, in the fully-relativistic, four-component FCI calculation, there are roughly $(\frac{1176}{340})^{340}$ possible N -electron configurations. Even a non-relativistic treatment, with only 196 electronic basis functions is impractical, with $(\frac{392}{340})^{340}$ or 10^{21} possible configurations in a FCI Hamiltonian. Accurately treating such large numbers of electrons with an all-electron FCI method is computationally prohibitive today. Truncating the CI calculation to a lower excitation level, say single and double excitations only, is a more tractable computational problem. Truncated Configuration Interaction Singles and Doubles (CISD) scales roughly as $(2K)^2 N^2$ [127]. Even then, in the case of the four-component calculation, the truncated CI yields a Hamiltonian with dimension over 10^{11} , still too large for modern computers. The non-relativistic, truncated calculation is smaller yet, with a Hamiltonian with dimension of the order of 10^{10} configurations, barely within reach of modern computers and algorithms. These examples illustrate the computational problem one encounters with all-electron methods, and the additional complexity added by accounting for relativistic effects. A popular way around these problems is through the use of Relativistic Effective Core Potentials (RECPs).

The Relativistic Effective Core Potential (RECP) approach is a compromise between the full Dirac description, and the non-relativistic model. RECPs are covered in greater detail in chapter two. Briefly, the RECP approach begins with atomic calculations using the full Dirac equation. An artificial separation between core electrons and valence electrons is selected, frequently based on hypotheses on which valence shell electrons are most important in chemical bonding. Those electrons selected to be in the core are replaced in the Hamiltonian by a potential energy term, leaving only the valence electrons to be explicitly modeled. This approach incorporates relativistic effects from a Dirac description of the atom directly into the core electrons, and has the added utility in reducing the large number of electrons present in heavy elements. These relativistic effective core potentials are then used in non-relativistic calculations, which can be used to compute excited states of atoms and molecules. Because the core electrons experience the most pronounced relativistic effects, calculations performed using these core potentials can produce results within a few percent of experimental measurements of electronic spectra. Armed with these relativistic effective core potentials, one can incorporate relativistic effects accurately and efficiently into non-relativistic calculations. With this freedom, one can then search for the most efficient non-relativistic algorithms available for calculating ground and excited states of atoms and molecules.

DFT is another successful alternative alternative to CI. DFT is a computational algorithm for solving the time independent, the Schrödinger wave equation, [35, 245] [106, 26-29] [127, 40]

$$\hat{H}\psi(\vec{x}_1, \vec{x}_2, \dots, \vec{x}_n) = E\psi(\vec{x}_1, \vec{x}_2, \dots, \vec{x}_n), \quad (2)$$

with E being the energy. A more thorough discussion of DFT is undertaken in chapter three, only a brief overview is given here. Unlike more traditional methods for solving equation 2, DFT is not based on N -dimensional abstract wave functions in Hilbert space, but on the physically realizable, 3-dimensional electron density. The success

of DFT is based on the accuracy inherent in the electron density functional responsible for the electron-electron exchange and correlation energies. While DFT is exact, in principle, for the ground state, current research has produced approximations for this exact exchange-correlation density functional. An additional attractive feature of DFT is the fact that it can produce remarkably accurate results for ground state geometries and vibrational frequencies very efficiently. DFT algorithms scale computationally on the order of (K^4) at a maximum, with some methods approaching linear scaling in the number of basis functions. Unfortunately, no method is known by which a DFT calculation, using a particular density functional approximation, can be systematically improved by improvements in the basis set or through perturbative corrections to the effective Hamiltonian. Extensions of DFT to solve the time-dependent Schrödinger equation exist, known as TDDFT, but the accuracy of TDDFT is poor when applied to calculated excited states of atomic and molecular systems where open-electron shells with large degeneracies can produce a range of spin-multiplicity states that are close in energy. Despite these drawbacks, DFT remains a computationally efficient way to compute electronic-electron correlation in atoms and molecules with excellent computational scaling, unlike the FCI or truncated CI.

Grimme [62] and Grimme and Waletzke [63] proposed a model which addressed the accuracy of DFT in open-shell and degenerate cases as well as calculating excited states. Their model combined a DFT calculation to the CI computational framework, resulting in a hybrid method which is designed to address the deficiencies of DFT with nearly degenerate states of multiple spin-multiplicities that are close in energy. By forming a hybrid DFT and CI method for computing excitation energies, Grimme and Waletzke found they could dramatically reduce the size of the CI expansion necessary to achieve results that were more accurate than TDDFT results. Their method demonstrated accurate calculations on excited states in their hybrid model with reductions in the CI expansion sizes on the order of a factor of hundreds to thousands.

1.2 *Research Objectives*

The goal of this research is to design, implement, and test a hybrid DFT/MRCI algorithm within the COLUMBUS relativistic quantum chemistry program suite. Final validation of the research goal will be through application of the DFT/MRCI model to the uranium +5 and +4 ions, as well as the uranyl (UO_2^{2+}) ion. The U^{5+} ion will demonstrate the ability of this modeling implementation to effectively compute the excitation energy of an odd-electron heavy element with both scalar relativistic and spin-orbit coupling of non-singlet and triplet spin multiplicities. The U^{4+} ion calculation will demonstrate the same capability, but on an even-electron heavy element, with spin-orbit coupling between singlet, triplet and higher multiplicities. These DFT/MRCI calculations will be assessed against equivalent Multi-reference Spin-Orbit Configuration Interaction Singles and Doubles (MR-SOCISD) calculations and experimental measurements of the excitation energies. Calculations of the uranyl ion will demonstrate this implementation of the DFT/MRCI model for a even-electron molecule containing a heavy element, with spin-orbit coupling between singlet, triplet, and higher multiplicities. The uranyl DFT/MRCI calculations will be compared with equivalent MR-SOCISD calculations and various crystallographic measurements of uranyl fluorescent series. In addition to spin-orbit effects, all heavy element calculations, including uranium, will model scalar relativistic effects as well, a capability absent in the most recent work by Kleinschmidt *et al* [77].

1.3 *Boundary Conditions*

In order to determine two free parameters crucial to the hybrid DFT/MRCI method, focus was placed on small, light atoms with modest basis sets, where full configuration interaction results were obtainable. This limited the damping parameter training set to the first two rows of the period table, with relatively small double- and triple- ζ quality basis sets.

To assess of the performance of the model following determination of the damping parameters, several well studied systems were chosen. The carbon monoxide

molecule was selected from the published results of Grimme and Waletzke to validate the new code by comparison with their implementation results. The boron fluoride molecule was chosen to reproduce published spin-orbit coupling results obtained by Kleinschmidt *et al* [76]. The boron fluoride molecule has a small spin-orbit splitting on the order of 20 cm^{-1} . The bromine atom, which exhibits a spin-orbit splitting of the ground state on the order of 3600 cm^{-1} , was chosen to assess the performance of this model on a heavy, odd-electron doublet atom with relatively large relativistic effects.

The uranium +5 and +4 ions were chosen since MR-SOCISD results as well as measured experimental excitation energies were available for comparison. The uranyl ion was also chosen because of its importance in uranium chemistry, and its electronic spectra has been thoroughly studied, both experimentally and theoretically.

1.4 Research Overview

Chapter two describes the underlying theory, methodology and results of traditional *ab initio* Multi-reference Configuration Interaction, Single and Double Excitations (MR-CISD) calculations on the excited states of the U^{5+} and U^{4+} ions. The excited states of these ions are calculated and assessed versus measured experimental excitation energies using a cc-pVDZ quality basis set and a series of shape-consistent RECP with spin-orbit potentials. Accuracy of the 60 electron, 68 electron, and 78 electron RECPs was compared to measured experimental values in order to determine the most effective core-valence choice when using shape-consistent core potentials in uranium calculations.

Chapter three describes the theory underlying the hybrid DFT/MRCI method, as well as the implementation of the model within the COLUMBUS quantum chemistry program suite. The results of the testing and validation of the model implementation are described, as are the results from calculations using the COLUMBUS-based DFT/MRCI hybrid model to carbon monoxide, boron fluoride, bromine, uranium +5 and +4 ions, and the uranyl ion.

Finally, an overall discussion of conclusions, both for the MR-SOCISD results on the U^{4+} and U^{5+} ions, as well as the performance of the DFT/MRCI model as implemented in this research is in chapter four. Success in achieving the research objectives will be examined, and final suggestions for future research will be made.

II. Uranium Ion Calculations

Assessment of the accuracy of calculations involving actinide elements is difficult, because of a sparsity of well-characterized, gas-phase experimental measurements. Part of the problem lies in the fact that interpretation of measured spectra can be complicated by the fact that many actinide compounds can be difficult to prepare in the gas-phase. Interpretation of condensed phase measurements can be complicated by crystal field effects or by the purity of the samples involved.

For example, the uranyl ion, UO_2^{2+} , has received intense theoretical scrutiny, and it is often used to benchmark theoretical methods involving uranium. A large, but hardly exhaustive list of recent calculations are contained in the references [34] [32] [105] [33] [85] [39] [64] [57] [74] [72] [142]. The chemical stability of the uranyl ion, and its presence in a majority of uranium compounds found in nature, as well as the relative insensitivity of its electronic spectra to its chemical environment make it an excellent candidate for these benchmarking studies. However, the lack of precise gas-phase measurements of the spectra of the uranyl ion limits its usefulness in assessing the accuracy of calculated electronic spectra. Variations on the order of 1000 cm^{-1} in the uranyl ion fluorescent spectra occur due to ligand influences [111], limiting the precision of comparisons with theoretical models. Attempts have been made to calculate the electronic spectra of uranyl in crystalline environments [86] [105] [8].

One solution is to perform calculations using atomic systems, for which gas-phase measurements have been performed and the resulting spectroscopic states are well characterized. For uranium, numerous experimental measurements of the electronic spectra of the neutral atom [90] [91] [36], as well as charged ions [17] [46] [100] [117] [139] [13] [23] exist in the literature. All these gas-phase studies of the neutral uranium atom and the +2, +3, +4 and +5 ionic species indicate that the low lying electronic transitions are predominately due to $5f$ to $5f$ electronic excitations, which are parity forbidden. These selection rule forbidden transitions result in faint yet sharp line spectra that are relatively unaffected when examined in uranium doped crystals or aqueous solutions, indicating that the $5f$ orbitals in uranium are not dom-

inant in ligand bonding. A search through the literature reveals surprisingly few computational studies of atomic uranium species. A brief summary of more recent calculations include predictions of the second through fourth ionization potential of neutral uranium was performed by Cao and Dolg [28], a Dirac-Hartree Fock investigation of dipole radiative parameters for uranium VI [15] by Biémont *et al*, and an investigation by Barandiaran *et al* of the bond lengths of f^n and $f^{n-1}d^1$ states of U^{4+} as defects in chloride hosts [8] using Complete Active Space Self Consistent Field (CASSCF) with a spinfree relativistic *Ab Initio* Model Potential Hamiltonian. Barandiaran *et al* found that the $5f$ electrons are shielded by the $6p$ electrons, which determine the bond lengths in f^n configurations, while in $f^{n-1}d^1$ configurations, an f electron penetrates the shielding effects of the $6p$ electrons and interacts with the ligands, causing a shortening of bond lengths in general. Seoju and Barandiaran investigated the structure and spectroscopy of U^{3+} defects in Cs_2NaYCl_6 [118], and their findings supported the conclusions reached by Denning *et al*, in that $5f$ to $6d$ transitions are responsible for the photoluminescence in the 14,000 to 21,000 cm^{-1} range. Fedorov *et al* performed an in-depth *ab initio* study of the excited states of uranium [55] using a transformed two-component Douglas-Kroll all electron method and spin-orbit multi configuration perturbation theory. Using this method, they calculated 48 odd-parity states of neutral uranium to within 1000-2000 cm^{-1} accuracy with respect to experiment. An older Dirac-Hartree Fock calculation by Eliav *et al* [53] used a coupled cluster method in order to predict ionization potentials and excitation energies in the uranium +4 ion. The excited states they computed using this four-component method with single and double coupled cluster excitations predicted the ordering of the U^{4+} states correctly with a reported average error in the excitation energies of 114 cm^{-1} .

Using the experimental measurements, as well as the theoretical results found in the calculations described above, an accurate assessment of the theoretical method can be performed and be used to guide the choice of *ab initio* methods, and active spaces. In addition, understanding the uranium ion atomic systems can yield greater insight

into the molecular structure of uranium compounds, since the low-lying excited states are dominated by $f \rightarrow f$ electronic transitions which are fairly insensitive to ligand influences. One of the major challenges to accurate quantum chemical calculations on heavy element atoms is a result of the importance of relativity in the electronic structure of high- Z elements.

2.1 Relativistic Effects in Chemistry

Relativistic effects in chemistry have been studied since the 1970s, with pioneering work by Pitzer [107], Pyykkö and Desclaux [109]. Many reviews of relativistic effects in chemistry can be found in the literature [109] [107] [108] [101] [73] [6] .

There are three main relativistic effects in atomic and molecular chemistry, all of which are roughly the same magnitude, and they scale approximately as Z^4 [108]. The first main relativistic effect is considered a direct effect, consisting of a radial contraction of atomic orbitals, along with a stabilization of the energy level of the electronic state. This effect is due primarily to the relativistic mass increase as electron velocities near the nucleus become appreciable fractions of the speed of light. Replacing the electron mass with its relativistic mass in the expression for the hydrogen Bohr radius formula yields

$$a_0 = \frac{4\pi\epsilon_0\hbar^2\sqrt{1 - \left(\frac{v}{c}\right)^2}}{m_0e^2} \quad (3)$$

Here, \hbar is Planck's constant divided by 2π , ϵ_0 is the permit

$$\alpha = \frac{e^2}{4\pi\epsilon_0\hbar c} \approx \frac{1}{137}. \quad (4)$$

For uranium, $Z\alpha$ is 0.67, yielding a $1s$ orbital radial contraction of roughly 26%. All atomic orbitals have some density near the nucleus, therefore, all atomic orbitals experience some contraction. However, the inner s - and p - orbitals nearest the nucleus experience the most contraction [108]. In light-element molecules, this orbital con-

traction is small and negligible in all but the highest precision calculations, but the effect becomes large in actinide elements such as uranium.

The second relativistic effect is an indirect effect, consisting of a radial expansion and destabilization in the electronic energy levels of outer atomic orbitals. This is due to increased effective nuclear charge screening by the inner, contracted orbitals, reducing the effective nuclear charge experienced by the outer electrons. Additionally, relativistic contraction of the inner s - and p - electron shells increase the electron density near the nucleus, crowding out the outer d - and f - electron shells. This results in a decrease in electron density near the nucleus for orbitals with increasing orbital angular momentum. The direct orbital contraction competes with the indirect orbital expansion, which can affect bond lengths and force constants [108]. These effects are observed in the spectra of heavy-element molecules. Spin-orbit coupling is another important spectroscopic effect which arises naturally from a Lorentz covariant description of the electron.

Intrinsic electron spin is a natural result of a Lorentz-covariant description of the quantum mechanical wave equation [7, 76-78,116]. This spin angular momentum couples with the electron orbital angular momentum, lifting degeneracy in atomic orbitals with angular momentum. Of the three effects, spin-orbit coupling has the largest impact in atomic and molecular spectra, even for low- Z atoms and molecules. For light atoms, a perturbative treatment of spin-orbit coupling known as Russell-Sanders coupling, or L - S coupling, often yields sufficient accuracy for electronic transition energies. This coupling scheme treats magnetic spin-orbit coupling as a small perturbation to the electron-electron electrostatic interaction. Orbital angular momentum and spin angular momentum are still approximately constant quantum numbers in this coupling scheme, where the total orbital angular momentum, L , total spin angular momentum, S , and total angular momentum, J commute with the many-electron Hamiltonian in Russell-Sanders coupling scheme. Atomic states are described by term symbols $^{2S+1}L_J$. Traditional spectroscopic notation is used for the total orbital angular momentum, with S representing zero total orbital angular

momentum, P representing one unit of orbital angular momentum and so on. J is the total angular momentum of the electron, given by the sum of orbital and spin angular momenta [58, 69-74] [140].

On the other end of the perturbation spectrum, more appropriate for very heavy atoms, the electron-electron electrostatic interaction is treated as a perturbation to the magnetic spin-orbit coupling. This coupling scheme is known as j - j coupling. In this coupling scheme, neither L nor S commute with the Hamiltonian. However, the total angular momentum, J , still commutes with the atomic Hamiltonian [58, 74-76] [140]. Most elements on the periodic table fall between these two perturbation extremes, and so intermediate coupling is more appropriate than either perturbative treatment. Intermediate coupling is not a separate coupling scheme, but occurs as deviations from the separate perturbative treatments given by L - S and j - j coupling [58, 77] [140].

Electron spin additionally has an important affect on the symmetry of molecules. Under the assumption that the total electronic wave function can be separated into the product of a spatial and spin wave functions, each wave function may possess separate symmetry, and the total, observable state symmetry is given by the direct product of the spatial and spin symmetries. For example, singlet spin states are completely symmetric, while triplet spin states transform like the components of the angular momentum operator. A completely symmetric spatial wave function multiplied by a triplet spin wave function will not be totally symmetric. For systems with a spin-orbit Hamiltonian, the symmetry point groups can have twice the number of symmetry operations, and are called double point groups. This doubling of the order of the symmetry point groups is due to the introduction of half-integral angular momentum values. Systems possessing an even number of electrons obey Bose-Einstein statistics, and the total wave function of these bosonic systems is symmetric with respect to rotations by 2π . Systems possessing an odd number of electrons obey Fermi-Dirac statistics, and fermionic wave functions change sign upon the exchange of two particles. This exchange is equivalent to a rotation by 2π , and so a rotation of 4π returns a fermionic system to its original state. While bosonic systems transform according

to the irreducible representations of the single point groups, where a rotation by 2π is equivalent to the identity operation, the rotation by 2π is a new symmetry operation for fermionic systems, doubling the order of the symmetry point group. For example, rotations of an even-electron system, such as the U^{4+} ion, transforms according to the normal irreducible representations of the $O(3)^+$ point group. Rotating the molecule by 2π leaves the wave function unchanged. An odd-electron system, such as U^{5+} , transforms according to the extra irreducible representations generated by a rotation of 2π . A rotating of the U^{5+} molecule by 2π changes the sign of the total electronic wave function. A rotation by 4π in this case returns the wave function to its original configuration [4, 22-28].

These three main effects, orbital contraction and energy stabilization, orbital expansion and energy destabilization, and spin-orbit coupling, along with the double group symmetry constitute the chemically relevant relativistic effects in atoms and molecules. The most important, from a spectroscopic standpoint is spin-orbit coupling, even in the spectra of the lightest elements. A quantum mechanical treatment of the electron must account for the intrinsic magnetic moment of the electron, and the Dirac equation accomplishes this quite elegantly.

2.2 Theory

Attempts at finding a Lorentz invariant form for the time dependent Schrödinger's equation,

$$\hat{H}\Psi(\vec{x}_1, \vec{x}_2, \dots, \vec{x}_n, t) = i\hbar \frac{\partial \Psi(\vec{x}_1, \vec{x}_2, \dots, \vec{x}_n, t)}{\partial t}, \quad (5)$$

led to two Lorentz-covariant equations: the Klein-Gordon equation, and the Dirac equation [138]. In equation 5, \hat{H} is the Hamiltonian operator, while $\Psi(\vec{x}_1, \vec{x}_2, \dots, \vec{x}_n)$ represents an N electron wave function. Each \vec{x}_i represents the electronic coordinates of the i th electron. Equation 5, because of the non-equivalent treatment of the spatial and temporal variables, is not Lorentz invariant, and therefore is limited to non-relativistic phenomena. Early attempts at making a Lorentz-covariant equation began

by quantizing the Lorentz-covariant relativistic energy expression [138],

$$E^2 = p^2c^2 + m_0^2c^4. \quad (6)$$

Here, p is the electron momentum, c is the speed of light, m_0 is the electron rest-mass, and E is the electron energy. Replacing the energy and momentum expressions with their quantized operator counterparts leads to the Klein-Gordon wave equation for a free particle [7, 99-101] [88, 884-888] [16, 4-6,198-206],

$$-\hbar^2 \frac{\partial^2 \Psi}{\partial t^2} = -\hbar^2 c^2 \nabla^2 \Psi + m_0^2 c^4 \Psi. \quad (7)$$

While this scalar wave function is Lorentz-covariant, in that both space and time variables are treated equivalently, it has several undesirable properties, making it unacceptable as a wave function for the electron. First, the probability density associated with it is not positive definite, resulting in the possibility of negative probability densities. Additionally, both positive and negative energy solutions to this equation exist, which complicated early interpretation of the solutions to this wave equation. The negative energy solutions were eventually understood to represent antimatter. The fact that the probability density is not positive definite makes this equation a poor choice for an electronic wave function; however, the Klein-Gordon turns out to be a valid relativistic wave equation for spin-free fields, such as π -mesons [88, 888] [7, 108] [138].

2.2.1 The Dirac Equation. Dirac took a different approach in formulating a Lorentz-covariant equation for a free electron [47] [48] [7, 110-119] [138]. Beginning with equation 7, one can obtain a nonlinear Hamiltonian, given by

$$\hat{H}_{Dirac} = \pm \sqrt{p^2c^2 + m_0^2c^4}. \quad (8)$$

Quantizing this expression by the usual substitutions for the energy and momentum operators yields a Hamilton that involves a first-order time derivative. However, the square root in the operator makes application problematic and hopelessly complicated. Dirac circumvented this problem by introducing a new degree of freedom into the Hamiltonian. This yields a tractable, linear operator,

$$\hat{H}_{Dirac} = c(\hat{\alpha}_1\vec{p}_1 + \hat{\alpha}_2\vec{p}_2 + \hat{\alpha}_3\vec{p}_3) + \hat{\beta}m_0c^2. \quad (9)$$

Requiring solutions to equation 9 to simultaneously satisfy the Klein-Gordon equation in equation 7 places restrictions on the components of the $\hat{\alpha}_i$ and $\hat{\beta}$ matrices,

$$\hat{\alpha}_i\hat{\alpha}_j + \hat{\alpha}_j\hat{\alpha}_i = 2\delta_{ij}, \quad (10)$$

$$\hat{\beta}^2 = \hat{1}, \quad (11)$$

$$\text{and} \quad (12)$$

$$\hat{\alpha}_k\hat{\beta} + \hat{\beta}\hat{\alpha}_k = 0. \quad (13)$$

In order to satisfy these restrictions both the $\hat{\alpha}_i$ and $\hat{\beta}$ must be at least four-by-four matrices, which operate on a four-component, spinor wave function. The Dirac equation is a set of four, coupled, first order partial differential equations in space and time. The four-component wave function solution to this equation has two positive energy components, corresponding to an electron with spin-up and spin-down, and two negative energy components, corresponding to a positron with a spin-up and spin-down component.

In the presence of an external field, the Dirac Hamiltonian, \hat{H}_D , becomes

$$\hat{H}_D = e\phi + \sum_i c\hat{\alpha}_i \cdot \left(\vec{p}_i - \frac{e\vec{A}_i}{c} \right) + \hat{\beta}m_0c^2, \quad (14)$$

where e is the electron charge, c is the speed of light, ϕ is the electrostatic potential, and \vec{A}_i is the i th component of the magnetic vector potential.

For the hydrogen atom, with no external magnetic field, this equation reduces to

$$\hat{H}_D = e\phi + \sum_i c\hat{\alpha}_i \cdot \vec{p}_i + \hat{\beta}m_0c^2, \quad (15)$$

While it is possible to construct an exact solution to this equation in terms of spherical harmonics for the angular coordinates and hyper geometric functions for the radial coordinate, such a construction does not shed much light on the nature of the bound energy states. The details of the solution can be found in various sources [88] [7, 119-129,159-175] [14, 63-70] [138]. The electronic energy levels for the Dirac hydrogen atom are given by [14, 68] [138] [7, 167-168]

$$E_{nj} = \frac{m_0c^2}{\sqrt{1 + \left(\frac{Z\alpha}{n-j+\frac{1}{2} + \sqrt{(j+\frac{1}{2})^2 - Z^2\alpha^2}} \right)^2}}. \quad (16)$$

Here, α is the fine structure constant, defined in equation 4, and the total angular momentum quantum number, j , takes on the values

$$j = l + \frac{1}{2}, \left| l - \frac{1}{2} \right|. \quad (17)$$

The binding energy of the hydrogen atom is given by $E_{nj} - E_0$, where $E_0 = m_0c^2$. Expanding $E_{nj} - E_0$ in powers of $(Z\alpha)^2$, assuming $Z\alpha \ll 1$, yields [14, 84]

$$E_{nj} = -\frac{Z\alpha}{2n^2} + \frac{(3 + 6j - 8n)(Z\alpha)^4}{8(1 + 2j)n^4}. \quad (18)$$

The first term is the non-relativistic energy for the bound electronic states of the hydrogen atom. Higher order corrections involve both the principle quantum number n , as well as the total angular momentum quantum number j . This illustrates the importance of a relativistic picture of the hydrogenic atom. Corrections to the non-

relativistic energy increase roughly as $(Z\alpha)^4$. Note that this Taylor series expansion in powers of $(Z\alpha)^2$ is appropriate for $(Z\alpha) \ll 1$. This expansion leads to the Russell-Sanders spin-orbit coupling scheme. Such an approximation is not valid for uranium, where $Z\alpha \approx 0.7$. In this case, the electrostatic electron-electron interaction can be treated as a perturbation to the magnetic interaction between the electron and the field of the nucleus. This approximation leads to the j - j spin-orbit coupling scheme, which is more appropriate for very heavy elements. However, for most elements on the periodic table, including uranium, neither perturbation regime is appropriate. Instead, an intermediate coupling scheme that exhibits features of both Russell-Sanders and $j - j$ coupling is what is observed.

Detailed examination of the negative energy component solutions to the Dirac equation for the free electron shows in the non-relativistic limit where $E - m_0c^2 \ll m_0c^2$, the amplitude of the positive energy components are much larger than the negative energy component amplitudes, especially in the valence region [7, 143-144]. The four-component Dirac wave function separates into two large and two small components. Rewriting the Dirac equation in terms of two, coupled differential equations with two, two-component wave functions yields the Pauli approximation to the Dirac Hamiltonian in the absence of an external magnetic field [7, 145-147]

$$\hat{H}_{Pauli} = E + e\phi + \frac{1}{2m_0}\nabla^2 + \frac{1}{2m_0c^2}(E + e\phi)^2 + i\frac{\mu_0}{2m_0c}\vec{E} \cdot \vec{p} - \frac{\mu_0}{2m_0c}\left[\hat{\sigma} \cdot (\vec{E} \times \vec{p}) - \mu_0(\hat{\sigma} \cdot \vec{H})\right]. \quad (19)$$

In this equation, \vec{H} is the magnetic field, \vec{E} is the electric field, and μ_0 is the Bohr magneton, defined by

$$\mu_0 = \frac{e\hbar}{2m_0c}. \quad (20)$$

Each separate term has a simple interpretation. The first three terms form the non-relativistic Hamiltonian. The next term is the mass-velocity correction that accounts for the variation in electron mass with speed. The fifth term is known as the Darwin

term, and is a result of zitterbewegung, or trembling motion. It is a result of the Heisenberg uncertainty principle. Non-relativistically, the uncertainty in the location of an electron can be measured to any accuracy using higher and higher energy photons. Relativistically, there is a limit to photon energy used to locate the electron, because at photon energies above $2m_0c^2$, pair production can occur. This results in an effective smearing of the charge of the electron [7, 186]. The final two terms account for the spin-orbit coupling between the intrinsic electron magnetic moment and the orbital angular momentum. The successes of the Dirac equation is the prediction of electron spin as an observable property in the non-relativistic limit, as well as accounting for the correct value for the electron magnetic moment. Thus, the inclusion of electronic spin in the non-relativistic theory as an additional assumption is validated and explained in the non-relativistic limit of the Dirac equation.

2.2.2 Relativistic Effective Core Potentials. Many methods exist for treating relativity in *ab initio* calculations, ranging from fully relativistic four-component calculations to two-component calculations using transformed versions of the Dirac Hamiltonian, as well as density function theory methods, but one particularly effective and popular choice is to use RECPs. Their utility comes from the fact that they introduce the most important relativistic effects in the form of an additional set of terms in the Hamiltonian which replace one or more core electrons. Using an RECP not only allows relativistic effects to be taken into account, but the number of electrons that need to be treated in a *ab initio* calculation is reduced as well. Several reviews of RECPs exist in the literature [51] [92] [68] [126] [50].

Several different types of RECPs exist. All are developed based on a fully relativistic, four-component theory such as Dirac-Hartree-Fock. Energy and shape consistent RECPs are similar in that both use pseudo-orbitals, which are designed to go smoothly and nodelessly to zero in the core region. Energy consistent RECPs incorporate experimentally measured atomic electronic excitation energies in the construction of both the RECP and accompanying pseudo orbital basis. Shape-consistent

RECPs and their accompanying pseudo orbitals do not include these semi empirical corrections and are based on fits to the four-component relativistic calculation alone.

Shape-consistent core potentials and pseudo-orbitals are generated from the two-component spinor resulting from a Dirac-Fock calculation [54]. Two forms are frequently encountered, a spin-free, averaged RECP,

$$U^{AREP} = U_L^{AREP}(r) + \sum_{l=0}^{L-1} \sum_{m=-l}^l [U_l^{AREP}(r) - U_L^{AREP}(r) |lm\rangle \langle lm|]. \quad (21)$$

Here, $U_L^{AREP} = U_L^{AREP}(r)$, is given by a weighted average of spinor components with the same J value,

$$U_L^{AREP}(r) = \frac{1}{2l+1} [lU_{l,l-\frac{1}{2}}^{REP}(r) + (l+1)U_{l,l+\frac{1}{2}}^{REP}(r)], \quad (22)$$

and a spin-dependent term,

$$H^{SO} = \vec{s} \cdot \sum_{l=1}^L \left[\frac{2}{2l+1} \right] \Delta U_L^{REP}(r) \cdot \sum_{m'=-l}^l \sum_{m=-l}^l |lm'\rangle \langle lm' | \vec{l} | lm\rangle \langle lm|, \quad (23)$$

with $\Delta U_l^{REP}(r) = U_{l,l+\frac{1}{2}}^{REP}(r) - (l+1)U_{l,l-\frac{1}{2}}^{REP}(r)$. Both U_L^{AREP} and H^{SO} potentials are fit to Gaussian-type functions of the form

$$U_l^{AREP} = \frac{1}{r^2} \sum_i C_{li} r^{n_{li}} \exp(-\zeta_{li} r^2). \quad (24)$$

The averaged relativistic effective core potentials described above are widely encountered in quantum chemical calculations, due to the ease of inclusion of these one component pseudo potentials into existing one component algorithms. The spin-orbit potential, however, is a two-component operator, which requires a two-component

wave function. This requirement for a two-component wave function is the main reason why spin-orbit potentials are infrequently used in quantum chemistry calculations. Shape-consistent pseudo potentials and pseudo orbitals are particularly attractive for two reasons. One reason is that the shape-consistent pseudo potentials are completely *ab initio*, meaning they are derived from first principles without empirical fits to experimental data, as is done with energy-consistent RECPs. A second reason to use shape-consistent pseudo potentials is that a spin-orbit operator can be derived along with the RECP.

2.2.3 Basis Sets for Use with Shape-consistent RECPs. Correlation-consistent double- ζ quality basis sets are generated using restricted open-shell Hartree-Fock atomic calculations. This procedure results in a shell-averaged description of a particular spin-state of the atom. Because exponent collapse can be a frequent occurrence when using $1s$ primitives in optimization of the exponents for heavy-element atom basis sets [20], Cartesian d functions are frequently used, with an additional linear combination added to represent the $3s$ functions. Such functions vanish at the origin, making them quite useful with shape-consistent pseudo potentials, which go smoothly and nodelessly to zero at the origin. Exponent collapse can occur during the development of $2p$ basis functions, though not as often. In this case Cartesian f functions can be used to circumvent the exponent collapse that can occur in the exponent optimization in larger basis sets. When $2p$ function primitives are used, an extra primitive is typically added to ensure the vanishing of the derivative of the contracted function at the origin [31]. When Cartesian functions of higher principle quantum number are used ($3sd$, $4pf$, etc.), the resulting contracted functions need not have their functional behavior at the origin compensated with an additional primitive, as they already go smoothly and nodelessly to zero at the origin. Polarization functions are added, and the exponents are hand optimized using MR-SOCISD calculations, typically involving correlation of the $5f$ electrons for uranium.

2.3 Methodology

There is no single, correct determination of the appropriate core-valence electron cutoff point when constructing RECPs. Other authors have investigated RECP accuracy in various atomic and molecular systems, exploring the various effects of basis set and core-valence cutoff using energy- and shape-consistent RECPs in comparison with experiment.

One such study by Stoll compared calculated bonding properties in the gold dimer (Au_2) using both large-, medium- and small-core energy-consistent pseudo potentials [125]. His definitions of core size in gold included the $1s - 4s$, $2p - 4p$, $3d - 4d$ and $4f$ electron shells for the small-core, medium-core to include small-core electrons plus $5sp$ electrons, and finally a large core definition of small-core plus $5spd$ electrons. Stoll found that in an energy-consistent pseudo potential, the medium core does not yield a good spatial separation between the core and valence electron shells, and the large-core choice interferes with bonding contributions from the $5d$ shell. Stoll concluded that some supplemental information from an all-electron or small-core calculation is essential when performing large-core calculations on molecular systems with significant overlap. He also found that core-valence and even core-core interaction corrections were necessary to supplement large-core calculations on equilibrium geometries, dissociation energies, and vibrational frequencies.

Another important study involving RECPs by de Jong thoroughly investigated the bond lengths and vibrational frequencies of the uranyl ion (UO_2^{2+}) using a number of four-component, all-electron Dirac-Hartree-Fock, Dirac-Hartree-Fock with second order perturbation corrections, and Dirac-Hartree Fock with singles, doubles, and perturbative triple coupled cluster contributions [39]. He compared these fully-relativistic, all-electron results to calculations using large- and small-core shape- and energy-consistent RECPs in conjunction with HF, HF plus second-order perturbation theory, and DFT calculations using both a Local Density Approximation (LDA) and hybrid GGA density functionals. He concluded that inclusion of the uranium $5d$

electron shell in the small-core RECP valence space was necessary to obtain favorable comparisons with the four-component benchmark calculations. He found that the best results were obtained with small-core, energy-consistent RECPs, and that g basis functions were necessary when using a correlated method such as second order perturbation theory. He also found that the hybrid GGA density functional performed better than the LDA functional when compared with the four-component, correlated benchmark calculations.

The effect of varying the core-valence cutoff using P. A. Christiansen *et al* shape-consistent RECPs to examine the ground and low-lying excited states of the U^{4+} and U^{5+} atomic cations were calculated. These species were chosen because of the tractable sizes of the MR-SOCISD expansions when using Correlation Consistent Valence Double- ζ with Polarization Functions (cc-pVDZ) quality basis sets. Three RECP core sizes were investigated for both cations: a 60 electron core, a 68 electron core, and a 78 electron core. The 78 electron core produces the valence electronic configuration for U^{5+} the valence electron configuration of $6s^2 6p^6 5f^1$. All other electrons with principle quantum number 5 and below are included in the core. The 68 electron core promotes the $5d$ shell from the core to the valence space, while the 60 electron core also frees the $5s$ and $5p$ shells from the core into the valence space. The 62 electron core choice was not investigated in this study. Its performance was assumed to be similar to the 60 electron core, in that the inclusion of the $5s^2$ together with the $5p^6$ was important, and that there would be minimal savings in computational effort in neglecting the $5s$ shell. For these ionic uranium species, electronic spectroscopic measurements find the lowest energy electronic transitions to be weak and sharp, which is characteristic of electric dipole forbidden $f \rightarrow f$ transitions. This suggests that at a minimum, the $5f$ electrons must be present in the valence space. Table 1 lists the valence electrons for each RECP for the ground state neutral uranium atom.

The COLUMBUS 6.0beta program suite [110] [82] was used to compute MR-SOCISD ground and excited electronic states of the U^{5+} and U^{4+} atomic uranium

Table 1: Valence Electrons Included in Uranium PAC-RECPs

PAC-RECP	Valence Electrons
60e	$5s^2 5p^6 5d^{10} 6s^2 6p^6 5f^3 6d^1 7s^2$
68e	$5d^{10} 6s^2 6p^6 5f^3 6d^1 7s^2$
78e	$6s^2 6p^6 5f^3 6d^1 7s^2$

cations. Calculations were performed using the D_{2h} Abelian point group. The uranium shape-consistent relativistic effective core potentials [54] were obtained from P. Christiansen [56]. Calculations on the both uranium cations were performed using cc-pVDZ quality basis set developed for use with the various shape-consistent RECPs by Dr. Scott Brozell for the uranium +2 ion from Restricted-Open Hartree Fock (ROHF) $6s^2 6p^6 6d^2 5f^2$ configuration averaged calculations. The cc-pVDZ basis sets are summarized in Table 2. In all basis sets, a p contraction was added in order to force the derivative of the p -functions be zero at the origin [31].

Table 2: Basis Sets for Use With Uranium PAC-RECPs

Core size	cc-pVDZ basis
60e	$(7sd5p4f1g)/[5sd3p2f1g]$
68e	$(5sd4p4f1g)/[4sd2p2f1g]$
78e	$(4sd4p4f1g)/[3sd2p2f1g]$

2.3.1 Selection of the Reference Space. Both $(5f6d)^1$ and $5f^1$ reference spaces were used. The occupied molecular orbitals were obtained from restricted open shell Hartree–Fock average-of-configuration calculations. In all calculations, the core electrons of the effective core potentials ($5s$, $5p$, $5d$) were frozen at the Hartree–Fock level in subsequent CI calculations. The $6s$ electrons, being core-like in the cc-pVDZ basis set, were also frozen. The $6p$ electrons were constrained to remain doubly occupied in all references, however, single and double excitations from the $6p$ shell were allowed. For U^{5+} only two MR-SOCISD calculations of 15 eigenvalues each were necessary in D_{2h} point-group symmetry to fully characterize the ground

and excited states, one for odd states, the other for even states. States of this odd-electron system transform like the double-valued irreducible representations of the double-group. State assignment (J , L , and S) was made through analysis of the degeneracy and parity of the computed eigenvalues.

All 91 even states arising from the $5f^2$ electron configuration were computed, but only the first few low-lying odd states were listed. Dr. Scott Brozell performed the calculations on the U^{4+} cation listed in Tables 5 and 6 [25]. The resulting states obtained for the even-electron U^{4+} system transform according to the appropriate single-valued irreducible representations of the double-group. The spherical symmetry of the atomic calculation was verified by investigating the degeneracy in the A_g , B_{3g} , A_u , and B_{3u} states. Again, state assignment (J , L , and S) was made via analysis of the degeneracy and parity of the eigenvalues. Results of the above calculations were compared with experimental measurements of the excited states of the uranium systems compiled and available on line [17].

2.4 Results

Results for the U^{5+} calculations are summarized in Tables 3 and 4.

Table 3 lists the results for those calculations on U^{5+} using all seven references arising from a $5f^1$ active space. The 2F states exhibit relative errors of roughly 10% when compared with experiment, except for the 78 electron cc-pVDZ case, where the relative error was nearly 20%, the 2D and 2S states show large relative errors of 10 to 30% with respect to experimental measurements. The 4F states were not reported in the experimental references. In the cc-pVDZ 78 electron RECP U^{5+} calculation, the ordering of the 2D and 4F states was reversed. Without experimental measurements for the 4F states, however, the qualitatively correct ordering of the 2D and 4F states can not be resolved at this time.

Table 3: U^{5+} Results, $5f^1$ Reference Space

J	Principle LS Component	60e PAC-RECP cc-pVDZ (cm^{-1})	68e PAC-RECP cc-pVDZ (cm^{-1})	78e PAC-RECP cc-pVDZ ¹ (cm^{-1})	Experiment [17] (cm^{-1})
$\frac{5}{2}u$	${}^2F_{\frac{5}{2}}^o$	0	0	0	0
$\frac{7}{2}u$	${}^2F_{\frac{7}{2}}^o$	7977(+4.8)	7560(-0.6)	6598(-13.3)	7608.6
$\frac{3}{2}g$	${}^2D_{\frac{3}{2}}$	102642(+12.8)	103246(+13.5)	114999(+26.4)	90999.6
$\frac{5}{2}g$	${}^2D_{\frac{5}{2}}$	112459(+11.9)	112030(+11.5)	125463(+24.8)	100510.5
$\frac{5}{2}u$	${}^4F_{\frac{5}{2}}^o$	124443	116683	117376	
$\frac{7}{2}u$	${}^4F_{\frac{7}{2}}^o$	129006	121025	121261	
$\frac{1}{2}g$	${}^2S_{\frac{1}{2}}$	154042(+8.9)	156038(+10.3)	166266(+17.5)	141447.5
RMS deviation		10.1%	10.2%	21.2%	

 Table 4: U^{5+} Results, $(5f6d)^1$ Reference Space

J	Principle LS Component	60e PAC-RECP cc-pVDZ (cm^{-1})	68e PAC-RECP cc-pVDZ (cm^{-1})	78e PAC-RECP cc-pVDZ ¹ (cm^{-1})	Experiment [17] (cm^{-1})
$\frac{5}{2}u$	${}^2F_{\frac{5}{2}}^o$	0	0	0	0
$\frac{7}{2}u$	${}^2F_{\frac{7}{2}}^o$	7990(+5.0)	7578(-0.4)	6641(-12.7)	7608.6
$\frac{3}{2}g$	${}^2D_{\frac{3}{2}}$	87760(-3.6)	92570(+1.7)	115240(+26.6)	90999.6
$\frac{5}{2}g$	${}^2D_{\frac{5}{2}}$	97593(-2.9)	101403(+0.9)	125704(+25.1)	100510.5
$\frac{5}{2}u$	${}^4F_{\frac{5}{2}}^o$	124554	116809	117588	
$\frac{7}{2}u$	${}^4F_{\frac{7}{2}}^o$	129116	121471	121471	
$\frac{1}{2}g$	${}^2S_{\frac{1}{2}}$	140841(-0.4)	146989(+3.9)	166507(+17.7)	141447.5
RMS deviation		3.4%	2.2%	21.3%	

The 68 electron RECP cc-pVDZ performs nearly as well as the 60 electron core calculation overall, however, the relative error for the first excited state is much more favorable in the 68 electron core calculation, on the order of 1% for the 68 electron core versus nearly 5% for the 60 electron core. Table 4 lists the results for those calculations on U^{5+} resulting from the 12 possible references arising from a $(5f6d)^1$ active space. Including the five references arising from $6d^1$ electronic configurations improves the relative errors in the 2D and 2S states. Additionally, using the larger, 12 orbital active space produces consistent ordering of the 2D and 4F states in all calculations. The 68 electron calculation results in the lowest relative and RMS errors overall.

Table 5 lists the results for those calculations on U^{4+} resulting from an $5f^2$ reference space, while Table 6 lists the U^{4+} results from a $(5f6d)^2$ active space.

In the $5f^2$ active space calculation, the 68 electron core, cc-pVDZ calculation outperforms the 60 electron core cc-pVDZ calculation in both relative and Root Mean Square (RMS) error. The relative and RMS errors observed in the 78 electron core, cc-pVDZ calculation on U^{4+} are an order of magnitude improved over the U^{5+} results, rivaling the results obtained using the 68 electron core. In the $(5f6d)^2$ active space calculation, the 68 electron core, cc-pVDZ calculation outperforms the 60 electron core cc-pVDZ calculation in both relative and RMS error. Using a larger active/reference space had little impact on the overall results for the event U^{4+} states, all of which arise from $5f \rightarrow 5f$ transitions. Again, the 78 electron core results are roughly equivalent in magnitude to the 68 electron core results, both in relative error and overall RMS error.

Finally, the ionization potential in eV is computed from the uranium +5 and uranium +4 data for each RECP, with results listed in Tables 7 and 8. No experimental measurement of this ionization potential was found in the literature.

Table 5: U^{4+} Results, $5f^2$ Reference Space

J	Principle LS Component	60e PAC-RECP cc-pVDZ (cm^{-1})	68e PAC-RECP cc-pVDZ (cm^{-1})	78e PAC-RECP cc-pVDZ (cm^{-1})	Experiment [17] (cm^{-1})
4g	3H_4	0	0	0	0
2g	3F_2	5221(+25.5)	4210(+1.2)	4097(-1.5)	4160.65
5g	3H_5	6731(+9.7)	6316(+2.9)	5518(-10.1)	6136.88
3g	3F_3	10290(+14.5)	9075(+1.0)	8291(-7.7)	8983.53
4g	3F_4	10536(+11.7)	9697(+2.8)	8692(-7.9)	9433.76
6g	3H_6	12724(+10.5)	11950(+3.8)	10480(-9.0)	11514
2g	1D_2	19892(+20.8)	17152(+4.2)	16146(-1.9)	16465
4g	1G_4	18413(+10.5)	17097(+2.6)	15177(-8.9)	16656
0g	3P_0	21134(+23.4)	18153(+6.0)	17572(+2.6)	17128
1g	3P_1	24157(+21.9)	20903(+5.5)	20022(+1.0)	19819
6g	1I_6	26955(+21.0)	25411(+14.1)	23316(+4.7)	22276
2g	3P_2	29231(+18.6)	25794(+4.6)	24124(-2.1)	24653
0g	1S_0	51162(+17.3)	48851(+12.0)	45112(+3.4)	43614
RMS deviation (even states only)		17.9%	6.4%	6.0%	
4u	$^3H_4^o$	75242(+27.1)	73734(+24.6)	81507(+37.7)	59183.36
2u	$^3F_2^o$	75856(+27.2)	74421(+24.8)	84586(+41.8)	59639.66
3u	$^3G_3^o$	79550(+26.2)	78560(+24.6)	90788(+44.0)	63052.78
4u	$^1G_4^o$	81699(+24.7)	79748(+21.7)	88999(+35.8)	65538.11
RMS deviation (all states)		26.3%	24.0%	40.0%	

Table 6: U^{4+} Results, $(5f6d)^2$ Reference Space

J	Principle LS Component	60e PAC-RECP cc-pVDZ (cm^{-1})	68e PAC-RECP cc-pVDZ (cm^{-1})	78e PAC-RECP cc-pVDZ (cm^{-1})	Experiment [17] (cm^{-1})
4g	3H_4	0	0	0	0
2g	3F_2	5186(+24.6)	4180(+0.5)	4007(-3.7)	4160.65
5g	3H_5	6764(+10.2)	6357(+3.6)	5606(-8.7)	6136.88
3g	3F_3	10287(+14.5)	9085(+1.1)	8291(-7.7)	8983.53
4g	3F_4	10510(+11.4)	9678(+2.6)	8640(-8.4)	9433.76
6g	3H_6	12776(+11.0)	12017(+4.4)	10622(-7.7)	11514
2g	1D_2	19793(+20.2)	17088(+3.8)	15183(-4.1)	16465
4g	1G_4	18405(+10.5)	17096(+2.6)	15973(-7.8)	16656
0g	3P_0	20983(+22.5)	18068(+5.5)	17296(+1.0)	17128
1g	3P_1	24052(+21.4)	20854(+5.2)	19841(+0.1)	19819
6g	1I_6	26975(+21.1)	25463(+14.3)	23385(+5.0)	22276
2g	3P_2	29139(+18.2)	25753(+4.5)	23999(-2.7)	24653
0g	1S_0	50373(+15.5)	48194(+10.5)	43855(+0.6)	43614
RMS deviation					
(even states only)		17.5%	6.2%	5.7%	
4u	$^3H_4^o$	56722(-4.2)	59993(+1.4)	60036(+1.4)	59183.36
2u	$^3F_2^o$	57143(-4.2)	60389(+1.3)	62316(+4.5)	59639.66
3u	$^3G_3^o$	60382(-4.2)	64082(+1.6)	68396(+8.5)	63052.78
4u	$^1G_4^o$	63070(-3.8)	65889(+0.5)	67033(+2.3)	65538.11
RMS deviation					
(all states)		4.1%	1.3%	5.0%	

 Table 7: U^{4+} Ionization Potential, $5f^n$ References

60e PAC-RECP cc-pVDZ (eV)	68e PAC-RECP cc-pVDZ (eV)	78e PAC-RECP cc-pVDZ (eV)
46.47	46.86	47.51

Table 8: U⁴⁺ Ionization Potential, (5f6d)ⁿ References

60e PAC-RECP cc-pVDZ (eV)	68e PAC-RECP cc-pVDZ (eV)	78e PAC-RECP cc-pVDZ (eV)
46.50	46.89	47.57

2.5 Analysis

Two factors impacting the relative and overall errors in the calculation of the electronic excitation energies of the U⁵⁺ and U⁴⁺ cations are the sizes of the relativistic effective potential core and the reference space. The effect of the core size in the uranium cation calculations shows that the 68 electron core performs well in both the small 5fⁿ and (5f6d)ⁿ reference spaces. States that arise from electron configurations not included in the reference space were poorly modeled in all calculations, and skew the overall RMS error accordingly. These states are the ²D and ²S states in the U⁵⁺ calculations, which arise from 6d¹ and 7s¹ electron configurations, respectively. Similarly, the odd states in the U⁴⁺ calculations, arising from 5f¹6d¹ electron configurations are not modeled well using only the 5f² references. The larger error in those states can be explained by the fact that excitations from electron configurations specifically in the reference space represent excitation levels higher than single and double excitations. For example, states produced by 6d¹ configurations are computed at the single and double excitation level when using a smaller 5f¹ reference space, however, these same states contain selected contributions of higher order (triple and quadruple) excitations from the larger (5f6d)¹ active space. Thus, the ²D states are computed at excitation levels higher than singles and doubles when computed using the larger active space.

In both uranium cation calculations, the 68 electron core produced the lowest relative and RMS errors, on the order of 1-2% for those states included in the reference space in the U⁵⁺ calculations. The 78 electron core produces large relative and RMS

errors in the U^{5+} calculation. The 60 electron core produces better results in terms of overall RMS and relative error when compared with the 78 electron core, however, the accuracies produced by the 60 electron shape-consistent RECP do not warrant the larger computational effort involved in its use, which involve CI expansions larger by roughly a factor of two to five over the 68- and 78-electron RECP. For the +4 cation, however, different results were obtained. When examining only the even states arising from the $5f^2$ configurations, both the 68 and 78 electron core calculations produced roughly equivalent results, both of which outperform the 60 electron core. Inclusion of the odd states arising from $5f^1 6d^1$ electronic configurations skew the overall errors in favor of the 68 electron core.

One possible explanation for the relative success of the 68 electron core RECP in the U^{5+} calculation may lie in the nature of the core and valence electron shell treatments. Recall the various valence electrons included in each RECP listed in table 1. Incorporation of an electron shell in the core allows for a relativistic treatment (relativistic contraction and expansion, as well as spin-orbit splitting) of those electrons, while relativity is treated indirectly, via interaction with the core potential, in the valence electrons. Electrons in the core p -shells are known to exhibit the largest spin-orbit splitting, so inclusion of the uranium $5p$ shell in the core in order for an accurate relativistic description seems warranted, as is done in the 68 and 78 electron core potentials. Removal of the uranium $5d$ shell from the valence space, as is done in the 78 electron shape-consistent core potential, does not allow for polarization of the $5d$ electron shell. The 68 electron core RECP strikes one possible compromise between relativity and polarization, with a relativistic treatment of the $5p$ shell, and a valence treatment of the $5d$ shell. The near degeneracy of the $5f$ and $6d$ shells in many uranium atomic species seems to require an accurate treatment of the $6d$ electronic excitations, which can be facilitated by freeing the $5d$ shell from the core and into the valence electron space.

The similar performance of the 78 and 68 electron cores in the even-state U^{4+} calculations seems to counter the argument presented above. One possible source of

this result is the fact that in this core potential treatment, there are no core-valence interactions possible, so the shape-consistent core potential method does not include any way for the core region to polarize. Thus, while the 68 electron core allows polarization of the $5d$ electrons, while only incorporating relativistic effects indirectly, through interaction with the core potential, the 78 electron core allows a relativistic treatment of the $5d$ electrons, but no relaxation of the $6d$ shell to occur. One possible explanation of the observed results is that these treatments are roughly the same magnitude, and that a higher order description of the core-valence interaction may be necessary to resolve the near degeneracy in the 68 and 78 electron core results. The fact remains, however, that the 78 electron core calculations represent a lower computation cost, and give reasonably accurate results, in the even-state U^{4+} calculations. It should be noted that even the 2% RMS error obtained in the 68-electron RECP calculation on U^{5+} is poor when compared with the precision obtainable in experimental measurements photoluminescence spectroscopy. The presence of a trend may be established by examining the U^{3+} and U^{2+} cations. The similar performance in the 68 and 78 electron cores does not carry over to the odd-states in the uranium +4 cation above the $4u$ state. This could be a result of significant contribution of the $7s$ references to the $2u$ states and above, which are not present in the reference spaces examined here. Marked improvement in the odd-states is observed in going from the $5f^2$ to the $(5f6d)^2$ reference space calculations.

Overall, applying Christiansen *et al* shape-consistent relativistic effective core potentials in MR-SOCISD calculations of the ground and excited states of U^{5+} and U^{4+} ions shows that the 68 electron PAC-RECP, along with a cc-pVDZ basis set, yields relative errors with respect to experimental measurements of 1 to 3% of experiment for each calculated state, part of which may be due to a fortuitous cancellation of error based on analysis of results obtained using double- ζ quality basis sets. The lowest relative errors in excitation energies were achieved when the reference space included all the electron configurations spawning the states of interest. Inclusion of the

spin-orbit interaction is crucial in these calculations, as the lowest energy electronic transitions in U^{5+} and U^{4+} arise from $5f \rightarrow 5f$ transitions.

III. The COLUMBUS-based DFT/MRCI Model

This chapter details the theoretical basis underlying the DFT/MRCI model, as well as detailed analysis of critical aspects of the model. The implementation, testing, and validation of the DFT/MRCI model is presented in detail, followed by applications of the model to various atomic and molecular systems and a discussion of the results obtained.

3.1 Theory

The theoretical foundation behind this hybrid DFT/MRCI model lies in the union of two distinct theoretical approaches to quantum chemistry: the Kohn-Sham approach to DFT and GUGA CI.

3.1.1 Non-relativistic Quantum Theory. The main goal of non-relativistic computational quantum chemistry revolves around the need to solve, exactly if possible, the time dependent Schrödinger wave equation for many-electron atoms and molecules. The time dependent equation is [35, 211]

In Equation 5, \hat{H} is the Hamiltonian operator, while $\Psi(\vec{x}_1, \vec{x}_2, \dots, \vec{x}_n)$ represents an N electron wave function. Each \vec{x}_i represents the electronic coordinates of the i th electron. For time independent states, the Schrödinger wave equation reduces to [35, 245] [106, 26-29] [127, 40]

$$\hat{H}\psi(\vec{x}_1, \vec{x}_2, \dots, \vec{x}_n) = E\psi(\vec{x}_1, \vec{x}_2, \dots, \vec{x}_n). \quad (25)$$

This representation assumes the Born-Oppenheimer approximation is valid, where the nuclear and electronic wave functions are uncoupled and treated separately. In this approximation, the electronic Hamiltonian operator, \hat{H} can be written using atomic units [127, 41-42] [106, 155-156] as

$$\hat{H} = -\frac{1}{2} \sum_{i=1}^N \nabla_i^2 - \sum_{i=1}^N \sum_{a=1}^M \frac{Z_a}{r_{ia}} + \frac{1}{2} \sum_{i=1}^N \sum_{j=1}^N \frac{1}{r_{ij}}. \quad (26)$$

where r_{ia} is the distance between the electron i and nucleus a , Z_a is the charge on the a -th nucleus, and r_{ij} is the distance between electron i and electron j . The first term is the electronic kinetic energy operator, the second term is the electronic-nuclear attraction potential energy, while the last term represents the electron-electron repulsion potential energy.

One approach to solving Equation 25 is to expand the electronic wave function, ψ in a product of N independent, one-electron wave functions, $\psi = \prod_{i=1}^N \varphi_i(\vec{x}_i)$, with each φ_i is a one-electron wave function called an orbital. The Pauli Exclusion Principle requires that this wave function be antisymmetric upon the exchange of any two electrons. A Slater determinant is one useful mathematical construct that results in a properly antisymmetric wave function, defined by

$$\Psi = \frac{1}{\sqrt{N!}} \begin{vmatrix} \varphi_1(\vec{x}_1) & \varphi_2(\vec{x}_1) & \cdots & \varphi_N(\vec{x}_1) \\ \varphi_1(\vec{x}_2) & \varphi_2(\vec{x}_2) & \cdots & \varphi_N(\vec{x}_2) \\ \vdots & \vdots & \ddots & \vdots \\ \varphi_1(\vec{x}_n) & \varphi_2(\vec{x}_n) & \cdots & \varphi_N(\vec{x}_n) \end{vmatrix}, \quad (27)$$

where each determinant represents a particular electron configuration in the many-electron system [78]. Wave functions can be formed from either a single Slater determinant, as is the case in the Kohn-Sham or Hartree-Fock approximations, or by linear combinations of Slater determinants.

3.1.1.1 The Hartree-Fock Approximation. The Hartree-Fock method finds the set of orthogonal molecular orbitals, that, when antisymmetrized using a single-determinant, yields the lowest possible energy. The Hartree-Fock approximation is a variational method, in that the Hartree-Fock energy obtained is guaranteed to be bounded from below by the exact energy of the system. The Hartree-Fock approximation is a mean-field approximation, where each electron experiences the average field of all other electrons, with the wave function written as a single Slater deter-

minant of one-electron orbitals. The difference between the exact, non-relativistic energy and the Hartree-Fock energy is defined as the correlation energy.

Correlation energy, which comes from two sources, is not modeled by the Hartree-Fock approximation by definition. The first source of correlation energy, non-dynamic correlation, is a result of the failure of the single Slater determinant model to adequately model the correlation between electrons with opposite spins. The second source of correlation energy, dynamic correlation, is from electron-electron coulombic interactions not modeled accurately by the mean-field approximation [127, 231-232] [106, 284-288] [37, 541-542].

The Hartree-Fock energy is given by [37, 37-96] [127, 108-151] [106, 269-307]

$$E_{HF} = \sum_{i=1}^N \left(i | \hat{h} | i \right) + \frac{1}{2} \sum_{i=1}^N \sum_{j=1}^N [(ii|jj) - (ij|ji)], \quad (28)$$

where the first term includes the one-electron kinetic and potential energies given by

$$\left(i | \hat{h} | i \right) = \sum_a \int \varphi_i^*(\vec{x}_1) \left(-\nabla^2 - \frac{Z_a}{r_{ia}} \right) \varphi_i(\vec{x}_1) d^3 x_1. \quad (29)$$

The second term the electron-electron Coulomb repulsion, modeling the local interaction between two charge densities, given by the integral [127, 113]

$$(ii|jj) = \left\langle \varphi_i(\vec{x}_1) | \hat{J}_j | \varphi_j(\vec{x}_2) \right\rangle = \int |\varphi_i(\vec{x}_1)|^2 \frac{1}{r_{12}} |\varphi_j(\vec{x}_2)|^2 d^3 x_2 d^3 x_1, \quad (30)$$

where $|\varphi_i(\vec{x}_1)|^2$ is the probability density for the i^{th} electron.

The third term in Equation 28 the electron-electron exchange interaction energy, which is a non-local interaction between an electron at a particular position and all the other electrons with identical spin over all space. This term correlates the motions between electrons with parallel spin. The energy is given by the integral [127, 113]

$$(ij|ji) = \left\langle \varphi_i(\vec{x}_1) | \hat{K}_j | \varphi_j(\vec{x}_2) \right\rangle = \int \varphi_i^*(\vec{x}_1) \varphi_j(\vec{x}_1) \frac{1}{r_{12}} \varphi_j^*(\vec{x}_2) \varphi_i(\vec{x}_2) d^3 x_2 d^3 x_1. \quad (31)$$

In operator form, the Hartree-Fock equation is given by [127, 114]

$$\hat{F}\varphi_i(\vec{x}_1) = \left[\hat{h}(\vec{x}_1) + \sum_{j \neq i}^N \hat{J}_j(\vec{x}_1) - \hat{K}_j(\vec{x}_1) \right] \varphi_i(\vec{x}_1) = \varepsilon_i \varphi_i(\vec{x}_1), \quad (32)$$

where \hat{F} is the Fock operator defined in Equation 32, and J_j is defined by [127, 113]

$$\hat{J}_j(\vec{x}_1)\varphi_i(\vec{x}_1) = \left[\int \varphi_j^*(\vec{x}_2) \frac{1}{r_{12}} \varphi_j(\vec{x}_2) d^3x_2 \right] \varphi_i(\vec{x}_1) \quad (33)$$

and K_j is defined by [127, 113]

$$\hat{K}_j(\vec{x}_1)\varphi_i(\vec{x}_1) = \left[\int \varphi_j^*(\vec{x}_2) \frac{1}{r_{12}} \varphi_i(\vec{x}_2) d^3x_2 \right] \varphi_j(\vec{x}_1). \quad (34)$$

This molecular orbital basis representation of the Fock operator is diagonalized, and the total Hartree-Fock energy is then given by

$$E_0 = \sum_i^N \langle i | \hat{h} | i \rangle + \frac{1}{2} \sum_i^N \sum_j^N \langle ij || ij \rangle, \quad (35)$$

with $\langle ij || ij \rangle$ given by

$$\langle i | \hat{J}_j | i \rangle - \langle i | \hat{K}_j | i \rangle \quad (36)$$

Correlation effects can contribute roughly 1 eV (23 kcal/mol) to the total electronic energy per electron pair [112]. An accurate treatment of electronic correlation is critical in order to perform meaningful comparisons between theoretical and experimental spectra. The Kohn-Sham approach to DFT is an elegant method for computing dynamic correlation energy using a single-determinant model.

3.1.2 The Kohn-Sham Approach to DFT. An alternative approach to solving Equation 25 using an electronic wave function is to use the electron density in two famous theorems. Hohenberg and Kohn proved that an exact solution to Equation 25 could be obtained using the electron density [70].

The first Hohenberg-Kohn theorem states that the potential is a unique functional of the density, neglecting a trivial constant factor. This simple theorem proves that the electron density completely determines the external potential, which, in turn, completely specifies the Hamiltonian. Hohenberg and Kohn's second theorem proves that this energy functional of the electron density is a minimum only when the exact ground-state density is used. Moreover, the only part of the energy functional that is system dependent is the external potential, $V_{ext}(\vec{r})$. For atomic and molecular systems, this external potential is $\frac{1}{r_{ij}}$. This implies that there exists a universal kinetic energy and electron-electron interaction functional, valid for any electronic system. Thus,

$$E_0[\rho] = \int V_{ext}(\vec{r})\rho(\vec{r})d\vec{r} + F_{HK}[\rho], \quad (37)$$

$$F_{HK}[\rho] = T[\rho] + V_{ee}[\rho].$$

In equation 37, T is the kinetic energy density functional, and V_{ee} is the electron-electron interaction potential. Here, $V_{ee}[\rho]$ can be split into classical and non-classical terms,

$$V_{ee}[\rho] = \frac{1}{2} \int \frac{\rho(\vec{r}_1)\rho(\vec{r}_2)}{|\vec{r}_1 - \vec{r}_2|} d\vec{r}_1 d\vec{r}_2 + V_{non-classical}[\rho]. \quad (38)$$

Hohenberg and Kohn's second theorem outlines a procedure for finding this exact ground state density. The theorem states that the exact energy can be determined via the variational principal, and that the exact density yields the lowest, exact energy. The only drawback is that the universal functional, $F_{HK}[\rho]$, is not known. However, the existence of such a functional is guaranteed, and once it is found, the non-relativistic Schrödinger wave equation can be solved exactly for the ground state electron density. While the Hohenberg-Kohn theorems proved the existence of a unique, exact energy functional of the electron density which would variationally yield the exact ground state energy of an atom or molecule, it did not proscribe a method for finding this density. In 1965, Kohn and Sham introduced a set of self-consistent equations which provided a means for computing the density efficiently [79],

very similar to the linear combination of atomic orbital method of Roothaan equations [114] [115] for the Hartree-Fock model. The Kohn-Sham approach introduced a fictitious, non-interacting system built from one-electron orbitals. However, unlike the Hartree-Fock model, where the one-electron orbitals are variationally optimized to yield the lowest total energy, the Kohn-Sham orbitals are chosen in order to reproduce the exact ground state density. In the Hartree-Fock approximation, the kinetic energy can be exactly written as

$$T_{HF} = -\frac{1}{2} \sum_{i=1}^N \langle \varphi_i | \nabla^2 | \varphi_i \rangle, \quad (39)$$

exact because of the exact treatment of the non-local exchange potential in the Hartree-Fock formulation. In the Kohn-Sham approach, a non-interacting reference system is introduced, creating an effective Hamiltonian given by

$$\hat{H}_{KS} = \frac{-1}{2} \sum_{i=1}^N \nabla^2 + \sum_{i=1}^N V_s(\vec{r}_i), \quad (40)$$

where $V_s(\vec{r}_i)$ is an effective, local potential. The Kohn-Sham approach then consists of choosing $V_s(\vec{r}_i)$ in order to yield the exact, ground state density from

$$\rho(\vec{r}) = \sum_{i=1}^N f_i |\varphi_{KS}(\vec{r})|^2. \quad (41)$$

Here, the f_i are Kohn-Sham orbital electron occupations numbers, while the ϕ_{KS} are the Kohn-Sham molecular orbitals. The main idea behind the Kohn-Sham approach is to take the universal functional of Hohenberg and Kohn, F_{HK} in Equation 37, and approximate it by separating out the energy of a non-interacting system, which accounts for the majority of the total energy of a system. Thus,

$$F_{HK}[\rho] = T_s[\rho] + E_c[\rho], \quad (42)$$

where $T_s[\rho]$ represents the strictly local kinetic energy functional of a non-interacting system of electrons with density $\rho(\vec{r})$, and $E_c[\rho]$ is defined as the exchange and correlation energy of the interacting system of electrons. $E_c[\rho]$ includes the kinetic energy of the interacting electronic system, as well as Coulomb electron-electron correlation and non-classical fermionic exchange. All these density functionals are all local, in that electron density at a point in space can only affect the energy in a small region of space. The fermionic exchange interaction described earlier is a non-local interaction, in that the electron density over all space affects the energy locally. This non-local aspect of the exchange interaction is a major challenge in the development of approximate density functionals, and it is the foundation of the Taylor expansion approach in exchange functional development.

Varying the energy functional with respect to the density yields the Kohn-Sham equations [79]

$$\left\{ -\frac{1}{2}\nabla^2 + [\varphi(\vec{r}) + \mu_{xc}[\rho]] \right\} \varphi_i^{KS}(\vec{r}) = \varepsilon_i \varphi_i^{KS}(\vec{r}), \quad (43)$$

with

$$\varphi(\vec{r}) = v(\vec{r}) + \int \frac{\rho(\vec{r}')}{|\vec{r} - \vec{r}'|} d\vec{r}'. \quad (44)$$

Here, $v(\vec{r})$ is the Coulomb potential, and $\mu_{xc}[\rho]$ is the correlation (and interacting kinetic energy) density functional. Together, $\varphi(\vec{r}) + \mu_{xc}[\rho]$ form an effective potential, $v_{eff}(\vec{r})$.

The main reason for the popularity of DFT as a computational tool today is that the same computational code developed and optimized for HF Self-Consistent Field (SCF) calculations could be immediately used for DFT calculations, the only difference being the need for evaluation of integrals over the correlation density functional. This allows introduction of electron-electron correlation to be included in a calculation with nearly the same computational cost as a Hartree-Fock calculation. DFT provides an inexpensive method to compute electron-electron dynamic correlation energy using an efficient one-body correlation operator.

A number of approximations to the universal functional give by Equation 42 exist, with the most successful based upon numerical fits to quantum mechanical Monte Carlo calculations on the ground state of a homogeneous electron gas by Ceperley and Alder [30]. Accurate hybrid functionals have also been developed that include some mixture of exact HF exchange, including B3LYP [12], PBE [102], and PBE0 [2].

More accurate modeling the non-local aspects of the exchange operator, through the inclusion of higher order Taylor expansions of the electron density, also known as Jacob’s Ladder [87] [131], has lead to the development of modern density functionals . Local density functionals involve only the electron density, while a GGA functional uses both the electron density and the gradient of the electron density. Modern functionals incorporate the Lapacian of the electron density, resulting in meta-GGA density functionals.

3.1.3 Configuration Interaction and the Graphical Unitary Group Approach.

A conceptually simple and popular method to compute electron-electron correlation energy is CI. In a CI calculation, the many-electron wave function is expanded in a series of states that differ from the ground state by exciting one or more electrons from a ground-state occupied molecular orbital to an unoccupied virtual orbital. Including all states that differ from the ground state by a single excitation is known as Configuration Interaction Singles (CIS), while including all possible single and double excitations is known as CISD. A FCI calculation is obtained if all possible excitations were included in the expansion. In the limit of a complete basis set, the full CI calculation yields the exact solution to the many-electron, non-relativistic Schrödinger equation. The CI approach does not require additional physics beyond the one-electron orbital model of Hartree-Fock, it simply corrects for deficiencies in the orbital basis chosen.

The CI wave function is written

$$\Psi = c_0\Psi_0 + \sum_{a,i} c_i^a\Psi_i^a + \sum_{a,b,i,j} c_{ij}^{ab}\Psi_{ij}^{ab} + \sum_{a,b,c} c_{ijk}^{a,b,c}\Psi_{ijk}^{abc} + \dots \quad (45)$$

The first term is the HF wave function, the second term is a sum over all singly excited states from the HF ground state, the third term consists of a sum over all doubly excitations, and so on. Additionally, the expansion coefficients, c_{ijk}^{abc} , are variationally optimized. In practice, this CI expansion must be truncated at some point, typically at single and double excitations. Brillouin’s theorem [127, 233-236] proves that there is no direct mixing between the HF ground state and singly excited states. However, the HF ground state does mix with the doubly excited states, which in turn couples to the singly excited states. The first logical place to truncate the CI expansion in order to obtain an improvement of the HF wave function is to truncate Equation 45 at single and double excitations.

The CISD method, while conceptually simple, can be very computationally demanding. It is known to exhibit slow convergence to the exact total electron correlation energy. In an N -electron system using K basis functions, the number of all possible double excitations is given by [127, 232] [37, 543].

$$\binom{N}{2} \binom{2K - N}{2}. \quad (46)$$

The number of configurations involved in the CISD method scales roughly as $(2K)^2 N^2$. An additional drawback to truncated CI expansion calculations is the fact that the truncation is not size extensive. A size extensive calculation scales linearly with the number of component parts of the system. For example, a size extensive calculation on the system AB, and two calculations on A and B separately provide the same accuracy both on the combined system as well as the individual component parts. Size extensivity is important when calculating certain molecular properties, such as dissociation energies. One result of non-size extensivity in truncated CI calculations is that a calculation on the system AB contains excitations not present in the component calculations on either A or B separately. Full CI calculations are size extensive, however, they are only possible using relatively small atomic or molecular systems with modest basis sets.

CI calculations provide a conceptually simple, yet computationally demanding way to compute both dynamic and non dynamic electron correlation energy. CIS calculations can not change the HF ground state, as a result, they do not model dynamic electron correlation. They do, however, model some of the multi determinant nature of the electronic wave function and can model some of the non dynamic electron correlation energy. CISD calculations model a portion of both dynamic and non dynamic electron correlation.

Two different approaches to performing CI calculations exist, determinant-based CI and GUGA-based CI. The first approach uses computes the complete CI Hamiltonian in a Slater determinant basis, where each Slater determinant is formed through excitation of electrons from some reference determinant or determinants. It is relatively straightforward to generate arbitrary excitation levels within a determinant basis, up to the full CI excitation levels of N excitations in an N electron system. This is achieved through simple substitution of virtual for occupied orbitals in the appropriate Slater determinant. Once the CI Hamiltonian is formed in the determinant basis, it is stored, either in memory or on disk, and then diagonalized. In general, Slater determinants are not spin eigenfunctions, and linear combinations of Slater determinants must be formed in order to construct states with well-defined spin multiplicity. This approach faces disk access bottlenecks, as large numbers of one- and two-electron integrals necessarily need to be accessed, essentially randomly, in order to construct the CI Hamiltonian. Once constructed, this Hamiltonian must be stored in some fashion in order to apply some large, sparse, symmetric matrix diagonalization routine in order to find the eigenvalues. These requirements can become quite demanding for large molecules, large basis sets, or both [120, 86-88].

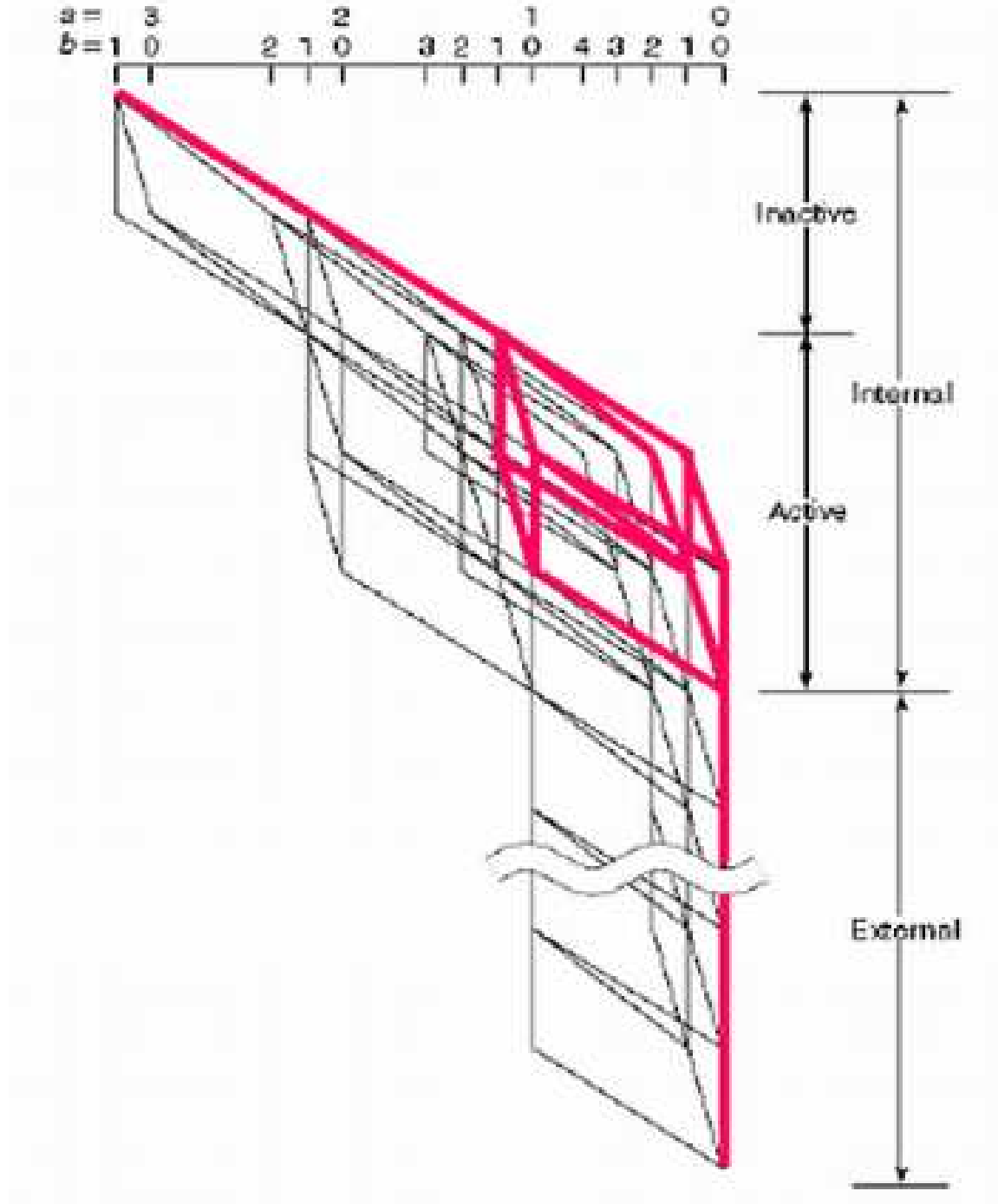
One way around this limitation is to use a direct method. In a direct method, the appropriate Hamiltonian matrix elements are constructed as needed, then discarded. This can reduce the disk access requirements, in that a relatively small subset of information need be stored. An effective way to determine which Hamiltonian matrix

elements need to be computed for the eigenvalue of interest, and from these, the one- and two-electron integrals and the coupling coefficients involved [120, 86-88].

The GUGA direct CI [113] [52] approach accomplishes just that. The technical details of GUGA are examined in detail in the literature [119] [120] [121].

Using unitary group techniques, a compact representation of the CI orbital basis is possible in the form of a Distinct Row Table (DRT). Using this DRT, one can efficiently construct all possible Configuration State Functions (CSFs) arising from some reference electronic configuration, or set of reference configurations. CSFs, which are spin eigenfunctions, can be efficiently defined in terms of molecular orbitals using the DRT, taking into account both spin-multiplicity and spatial symmetry. Not only does the DRT allow compact and efficient organization of the orbital basis functions into CSFs, it also provides, through the graphical representation, insight into the structure of the CI Hamiltonian. Figure 1 [122] shows the graphic depiction of a distinct row table for a MR-CISD calculation. The reference CSFs are shown in red. The MR-CISD graph is broken up into two distinct regions, internal (active and inactive), and external spaces. The internal space consists of those orbitals that are occupied in the reference configurations. Inactive orbitals are doubly occupied in all references, while active orbitals can be either doubly, singly, or unoccupied in the reference space. External orbitals, or virtual orbitals, are unoccupied in the reference space. The structure of the graph of the external space is relatively simple, and independent of the size of the number of external orbitals. The MR-CISD graph is arranged in this fashion due to the regular structure of the external space, and inactive internal space [122].

Figure 1: Distinct Row Table Graph for Multi Reference Single and Double Excitation Configuration Interaction Expansion [122]



3.1.3.1 The Unitary Group and the Repartitioning of the Hamiltonian.

The utility of the GUGA approach so far has been to compactly and efficiently index all possible CSFs arising from some arbitrary excitation level within an orbital basis. Truncation of this CI expansion is easily achieved, removing individual CSFs, groups of CSFs, or even entire excitation levels. The real power behind the GUGA approach lies in its ability to describe the coupling between CSFs, allowing the efficient computation of the CI Hamiltonian matrix elements between CSFs [120, 65-69].

There is a direct correspondence between the CI Hamiltonian matrix elements between CSFs and the matrix elements of the unitary group generators, \hat{E}_{ij} . These unitary group matrix elements can be constructed from generator operators, which satisfy the commutation relation [120, 69-70] [123]

$$\left[\hat{E}_{ij}, \hat{E}_{kl} \right] = \delta_{jk} \hat{E}_{il} - \delta_{il} \hat{E}_{kj}, \quad (47)$$

corresponding to

$$\hat{E}_{ij} \hat{E}_{kl} - \delta_{jk} \hat{E}_{il} = \hat{E}_{kl} \hat{E}_{ij} - \delta_{il} \hat{E}_{kj}. \quad (48)$$

This generator operating on a Configuration State Function (CSF) has the effect of moving an electron from orbital j to orbital i without changing the overall spin-state. This is useful because the generators of the unitary group satisfy the same commutation relation as the second-quantization substitution operators [124],

$$\hat{E}_{ij} = \hat{X}_{i\alpha}^\dagger \hat{X}_{j\alpha} + \hat{X}_{i\beta}^\dagger \hat{X}_{j\beta}, \quad (49)$$

where the \hat{X}^\dagger are creation operators, and the \hat{X} are annihilation operators, creating or annihilating an electron in spatial orbital i or j with spin α or β . In second-quantization form, the Hamiltonian is [120, 65-66]

$$\hat{H} = \sum_{ij} \sum_{\sigma} h_{ij} \hat{X}_{i\sigma}^\dagger \hat{X}_{j\sigma} + \frac{1}{2} \sum_{ijkl} \sum_{\sigma\tau} [ij; kl] \hat{X}_{i\sigma}^\dagger \hat{X}_{k\tau}^\dagger \hat{X}_{l\tau} \hat{X}_{j\sigma}, \quad (50)$$

where

$$h_{ij} = \langle i | h | j \rangle, \quad (51)$$

and

$$[ij; kl] = \left\langle i(1)k(2) \left| \frac{1}{r_{12}} \right| j(1)l(2) \right\rangle. \quad (52)$$

In Equation 50, σ and τ run over electron spin states α and β .

It is useful to repartition the CI Hamiltonian so that states are described not relative to the vacuum state, but instead states are described relative to some reference state or states. A particularly useful choice is to select a reference occupancy, μ_k , corresponding to the most common orbital occupancy in the reference space. A new set of modified one- and two-body unitary group operators can be defined by [120, 66-69]

$$\hat{F}_{ij} = \hat{E}_{ij} - \mu_i \delta_{ij}, \quad (53)$$

$$\hat{f}_{ij,kl} = \hat{e}_{ij,kl} - \quad (54)$$

$$\left(\mu_i \delta_{ij} \hat{E}_{kl} + \mu_k \delta_{kl} \hat{E}_{ij} - \mu_i \mu_k \delta_{ij} \delta_{kl} \right) + \quad (55)$$

$$\frac{1}{2} \left(\mu_i \delta_{il} \hat{E}_{kj} + \mu_k \delta_{kj} \hat{E}_{il} - \mu_i \mu_k \delta_{il} \delta_{kj} \right) + \quad (56)$$

$$\frac{1}{2} (2 - \mu_i) \delta_{ij} \delta_{kl} \delta_{kj}. \quad (57)$$

This definition removes reference occupancy contributions from terms in Equation 50.

Introducing a modified Fock operator [120, 68]

$$\hat{u} = \hat{h} + \sum_k \mu_k \left(\hat{J}_k - \frac{1}{2} \hat{K}_k \right), \quad (58)$$

with \hat{J}_k and \hat{K}_k being the normal Coulomb and exchange operators. Using the definitions presented in equations 53 through 58, along with modified one-electron integrals

defined by [120, 68-69]

$$u_{ij} = h_{ij} + \sum_k \mu_k \left([ij; kk] - \frac{1}{2} [ik; kj] \right), \quad (59)$$

one can recast the second quantized form of the Hamiltonian, Equation 50, into a repartitioned form,

$$\hat{H} = E_0 + \sum_{ij} u_{ij} \hat{F}_{ij} + \frac{1}{2} \sum_{ijkl} [ij; kl] \hat{f}_{ij,kl}. \quad (60)$$

In this repartitioned form, the reference energy, E_0 is given by

$$E_0 = \frac{1}{2} \sum_i [\mu_i (h_{ii} + \epsilon_i) - \mu_i (2 - \mu_i) g_{ii}], \quad (61)$$

where $g_{ij} = [ii; jj] - \frac{1}{2} [ij; ji]$ and $\epsilon_i = u_{ii} = h_{ii} + \sum_k \mu_k g_{ik}$.

3.1.3.2 Matrix Elements of the Repartitioned Hamiltonian. Now that

the repartitioned Hamiltonian has been suitably defined in Equation 60, the next step in order to perform a GUGA based CI calculation is to compute the matrix elements between arbitrary CSFs.

Matrix elements between two CSFs, m and m' , are obtained from [124]

$$\langle m' | \hat{H} | m \rangle = \sum_{ij} \sum_{\sigma} h_{ij} \langle m' | \hat{E}_{ij} | m \rangle + \frac{1}{2} \sum_{ijkl} \sum_{\sigma\tau} [ij; kl] \langle m' | \hat{e}_{ij,kl} | m \rangle, \quad (62)$$

with \hat{E}_{ij} the unitary group generator, and $\hat{e}_{ij,kl}$ given by

$$\hat{E}_{ij} \hat{E}_{kl} - \delta_{jk} \hat{E}_{il} = \hat{e}_{ij,kl} = \hat{e}_{kl,ij}. \quad (63)$$

The matrix elements of the generator \hat{E}_{ij} and $\hat{e}_{ij,kl}$ are coupling coefficients between two CSFs. For diagonal, or weight, generators, \hat{E}_{ii} , the matrix elements are particu-

larly simple, given by [124].

$$\langle m' | E_{ii} | m \rangle = \delta_{m'm} n_i(m). \quad (64)$$

Here, $n_i(m)$ is the occupancy of orbital i in the CSF m . The one-body raising and lowering generators are adjoint, $\hat{E}_{ij} = \hat{E}_{ji}^\dagger$, resulting in [120, 70] [124]

$$\langle m' | \hat{E}_{ij} | m \rangle = \langle m | \hat{E}_{ij} | m' \rangle. \quad (65)$$

Because of 65, matrix elements over the raising generators, \hat{E}_{ij} need only be computed. An additional identity

$$\langle m' | \hat{E}_{ij} | m \rangle = 0, \quad (66)$$

further simplifies things, provided $i < j$ and $m' \geq m$. Outside of the range (i, j) , the two CSF orbital occupancies and spin coupling must coincide. Inside the range (i, j) , a loop in the DRT graph is formed. Vertices of the m and m' branches of the loop must be related by [120, 70-72] [124]

$$N'_k = N_k + 1 \quad (67)$$

and

$$S'_k = S_k \pm \frac{1}{2}, \quad (68)$$

in order for a non-vanishing matrix element, $\langle m' | E_{ij} | m \rangle$ to be non-vanishing, where N_k and S_k are the electron occupation and spin-multiplicity at the k -th level of the DRT respectively. This limits the possible relationships between two vertices in the DRT graph at each level k . The value of the matrix element can be constructed from the product of individual segment values within the loop [120, 73] [124]

$$\langle m' | E_{ij} | m \rangle = \prod_{k=(i,j)} \omega(Q_k; d'_k d_k, \Delta b_k, b_k). \quad (69)$$

Here, Q_k is a segment type symbol, with possible values $Q_k = W, R, L, \overline{R}, \overline{L}, \underline{R},$ or \underline{L} . By defining $T_k = (Q_k; d'_k d_k, \Delta b_k)$ as a segment shape symbol, one obtains [120, 73] [124]

$$\langle m' | E_{ij} | m \rangle = \prod_{k=(i,j)} \omega(T_k, b_k), \quad (70)$$

where T_k is now dependent only on the shape of the segment interaction, and all segment interactions with the same shape are equivalent. These T_k are one-body segments. The end result is that the GUGA CI matrix element between two interacting CSFs depends only on the difference in electron occupation and spin-multiplicity over a limited range of orbitals. In the graphical representation, these interacting CSFs form a loop over a narrow range of levels on the DRT, with a limited number of possible arc interactions. The CI matrix element can be constructed as a factored product of separate loop interactions over the range of orbitals where the two CSFs differ, either by occupation, spin-multiplicity, or both. All possible one body loop segment shapes are shown in Figure 2. Step numbers are shown in red, along with relative b values. The loop values are also listed below each segment shape [124].

A similar treatment of the matrix elements of the two-body generators yields [120, 76-86] [124]

$$\langle m' | e_{ij,kl} | m \rangle = \prod_{p \in S_1} \omega(T_p, b_p) \sum_{x=0,1} \prod_{p \in S_2} \omega_x(T_p, b_p), \quad (71)$$

where $S_1 = (i, j) \cup (k, l) - S_2$ and $S_2 = (i, j) \cap (k, l)$. S_1 is the non-overlapping region between the two CSFs, while S_2 is the overlapping region. S_1 and S_2 range over $i, j, k,$ and $l,$ inclusive. Again, the result is that the matrix element can be factored into shape dependent factors, which are equivalent as long as segment shapes are the same, and level dependent factors, b_p . Through a careful definition of the various T_k segment shape symbols, matrix elements over one-body and two-body unitary group generators can be computed. These matrix elements are then the coupling coefficients between CSFs in both the Hamiltonian and the repartitioned Hamiltonian,

and facilitate an efficient, loop-driven [24] direct CI calculation [120, 86-96] [124]. All non-zero contributing loop segment shapes to the CI Hamiltonian are shown in Figure 3.

Figure 2: One Body Loop Segments [124]

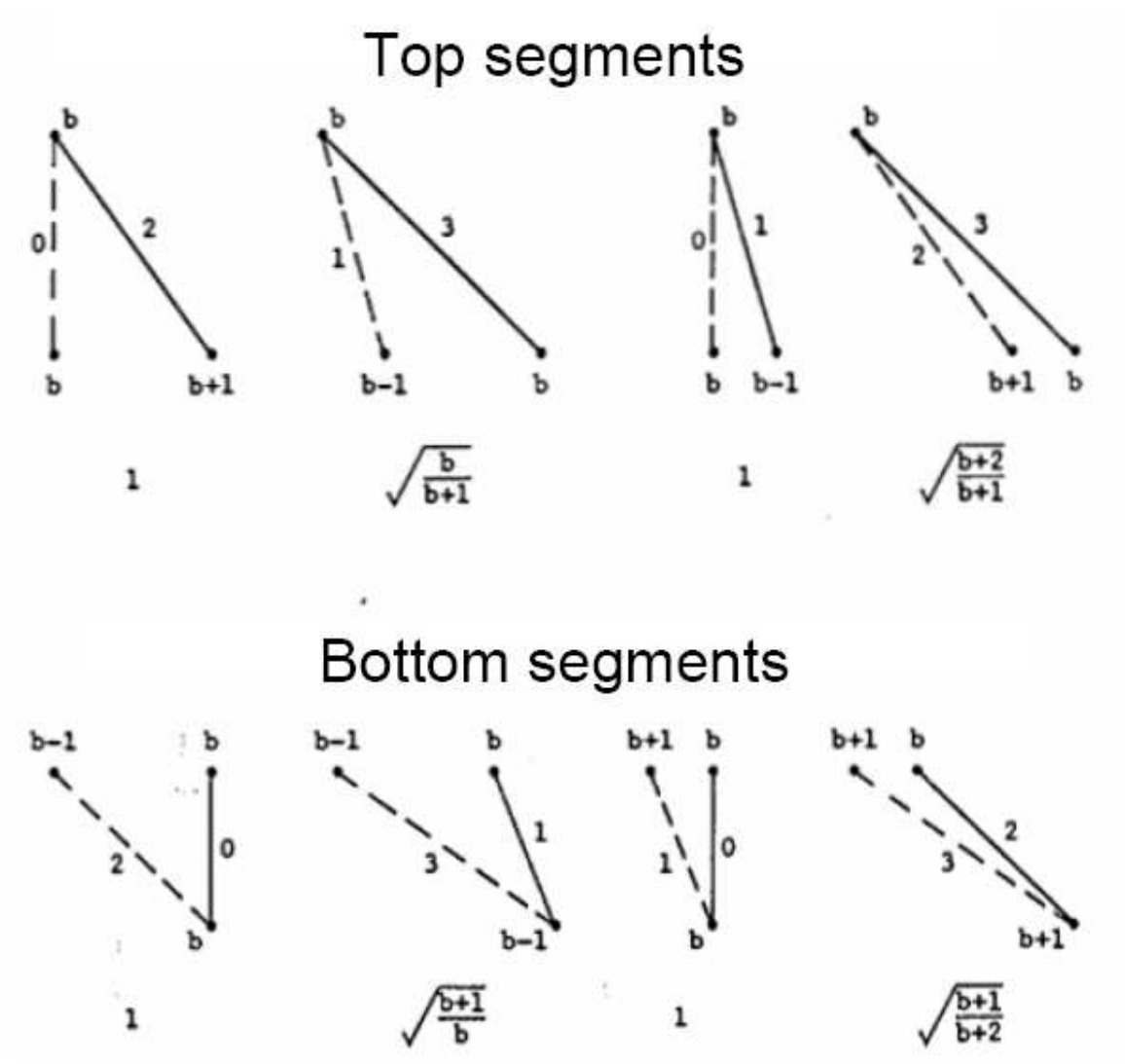
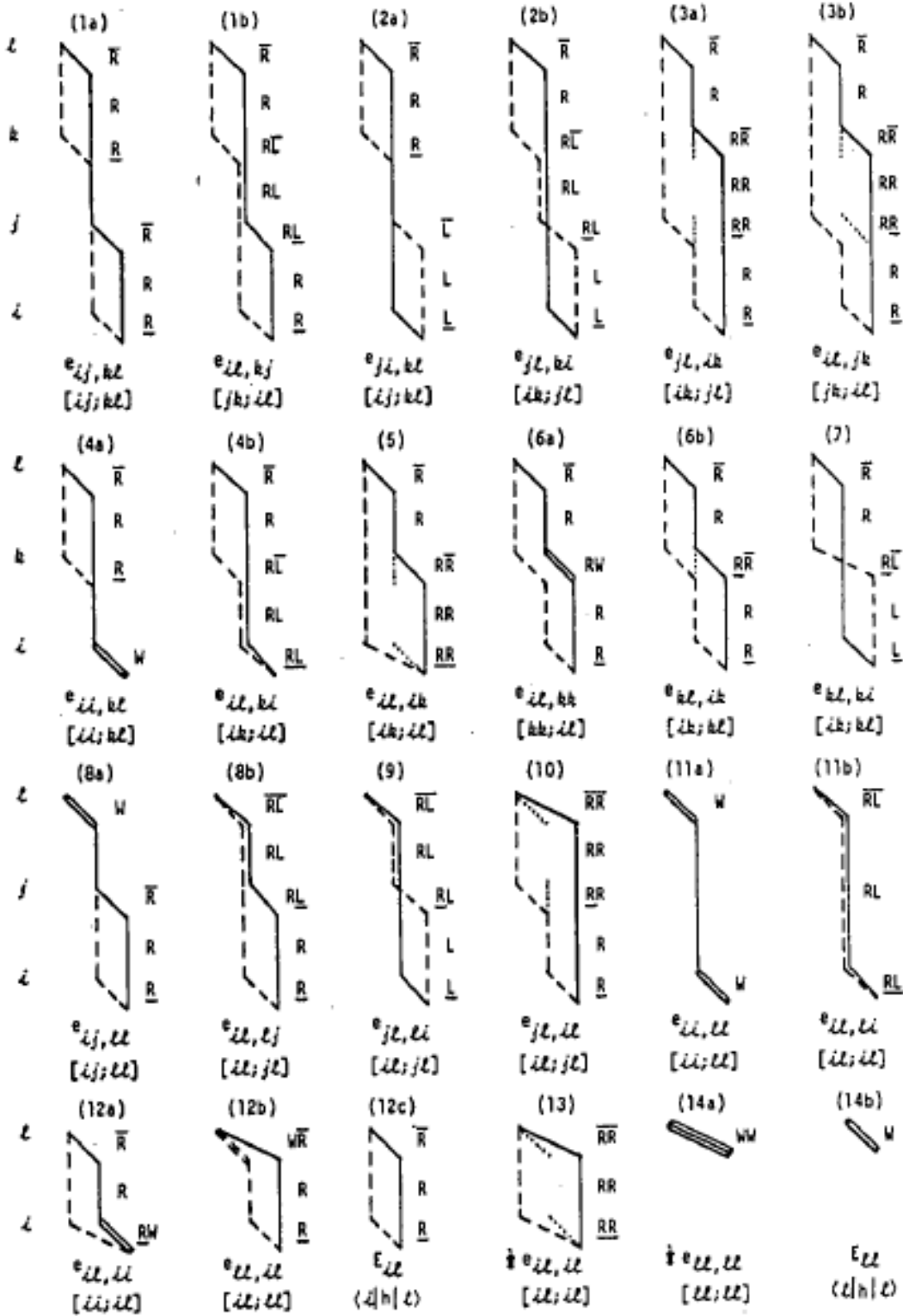


Figure 3: Non-zero Loop Contributions to the CI Hamiltonian [120, 92]



3.1.4 *Hybrid DFT/MRCI Model.* While DFT accounts for dynamic electron-electron correlation via an approximate correlation density functional, it has difficulty in modeling atomic and molecular systems with significant multi determinant character. This is not necessarily a failing of the theory, which, in principle, is exact if the exact universal density functional was known and used, but a failing of the approximate density functionals developed to date.

One possible way to model this multi reference, non-dynamic electron-electron correlation was proposed by Grimme [62]. His approach was to use the Kohn-Sham molecular orbitals generated by a DFT calculation as the expansion basis for a relatively small CIS calculation. His idea was that the CI calculation would provide a way to compute the multi determinant non-dynamic correlation, while the single reference DFT calculation modeled the dynamical electron-electron correlation via the approximate correlation density functional.

By performing CIS in his first paper, and later CISD with Walteske [63], Grimme was able to compute electronic excitation energies of several systems known to have significant non-dynamic electron correlation accurately when compared with experiment and more traditional, wave function based approaches. During the construction of the CI Hamiltonian, Grimme and Waletske construct an effective DFT/CI Hamiltonian using the following construction for diagonal matrix elements [63]

$$\begin{aligned} \langle \omega w | \hat{H}^{DFT} - E^{DFT} | \omega w \rangle = & \langle \omega w | \hat{H} - E^{HF} | \omega w \rangle - \sum_c^{n_{exc}} F_{cc}^{HF} - F_{cc}^{KS} + \\ & \sum_a^{n_{exc}} \hat{F}_{aa}^{HF} - \hat{F}_{aa}^{KS} + \frac{1}{n_{exc}} \sum_a^{n_{exc}} \sum_c^{n_{exc}} p_J (aa|cc) - p [N_0] (ac|ac), \end{aligned} \quad (72)$$

where F_{ij}^{KS} is the matrix element of the Kohn-Sham effective Hamiltonian given by

$$F_{ij}^{KS} = h_{ij} + (i|V_c(\rho)|j) + \sum_k n_k (ij|kk), \quad (73)$$

and ω and w represent spin-coupling pattern and spacial occupation vector, respectively.

Grimme and Waletske replace the HF orbitals with their Kohn-Sham counterparts, then they scale the two electron contributions to the excitation energy by empirically determined constants, p_j and $p[N_0]$. According to their research, the scale factor p_J depends on the amount of exact HF exchange used in the computation of the Kohn-Sham orbitals, and is given in this case by

$$p_J = 1 - x_{HF}, \quad (74)$$

where x_{HF} is the amount of exact HF exchange used in the DFT calculation, taking the value of zero if no Hartree-Fock exchange was included, and one if no exchange functional was used. The second parameter, $p[N_0]$, depends on the number of open shells, N_0 in the state $|\omega w\rangle$. They observed a systematic increase in $p[N_0]$ as the number of open shells increased in their calculations, and they assumed a linear relationship between $p[N_0]$ and N_0 . For singlet states, they assumed the relationship

$$p[N_0] = {}^1p[0] + N_0^1\alpha, \quad (75)$$

while for triplet states,

$$p[N_0] = N_0^3\alpha. \quad (76)$$

Note that their method did not allow any spin coupling aside from single or triplet states. Any new spin coupling state would require additional empirical parameters in their method. For off-diagonal elements $\langle\omega w|\hat{H}^{DFT}|\omega'w'\rangle$, where DFT can provide no information about the coupling between states, Grimme and Waletske use a damping factor dependent on the difference in energy between the diagonal matrix elements for each configuration state function.

$$\langle\omega w|\hat{H}^{DFT} - E^{DFT}|\omega'w'\rangle = p_1 e^{-p_2 \Delta E_{\omega w'}^4} \langle\omega w|\hat{H} - E^{HF}|\omega'w'\rangle \quad (77)$$

Table 9 lists the values obtained by Grimme and Waletske for empirical parameters, optimized for use with the Becke half-and-half hybrid exchange correlation functional (BHLYP) density functional. This scaling factor reduces the double count-

Table 9: Optimized DFT/MRCI Parameters for the BHLYP Functional for Singlet and Triplet States [63]

<u>Multiplicity</u>	p_1	p_2	p_J	$p[0]$	α
singlet	0.619	3.27	0.510	0.595	0.106
triplet	0.619	3.27	0.493	-	0.056

ing of dynamic electronic correlation by both the DFT correlation functional and the CI calculation, and it also ensures that only those states energetically close to each other can couple strongly, which accounts for the bulk of the non-dynamic electronic correlation. No scaling is applied to off-diagonal elements between states with the same spatial part.

Another advantage of the Grimme-Waletzke DFT/MRCI method is that the size of the CI expansion can be significantly reduced, in some cases, by several orders of magnitude. For relatively large systems with a large number of electrons, a full CI expansion can be quite large, on the order of hundreds of millions of CSFs or more. However, because the DFT calculation captures so much of the dynamic correlation, such large CI expansions are unnecessary. Since only the non-dynamic correlation is desired from the CI calculation, Grimme and Waletzke proposed a CSF selection procedure based upon the orbital energy difference between occupied and virtual orbitals [63]. By ignoring CSFs between states that differ by more than some arbitrarily determined cutoff energy, δE , the size of the CI expansion was reduced from several million or even billion CSFs, to several thousand CSFs. Grimme and Waletzke’s implementation of their model was based upon a selected CI algorithm, where individual CSFs can be selectively included or excluded from the CI Hamiltonian.

3.1.4.1 Analysis of Off-diagonal Damping in the Effective DFT/MRCI Hamiltonian. The scaling factor applied to the off-diagonal matrix elements in the

hybrid CI Hamiltonian serves to adjust the coupling between CSFs in the CI orbital expansion. This is analogous to damping in a system of coupled mechanical or electrical oscillators. As the coupling between modes is reduced, energy is removed from the system. This is not necessarily the case in the hybrid DFT/MRCI model, however. This is because both the DFT and the CI both model the dynamic correlation energy. Including both sources of this energy results in an overestimate of the dynamic correlation energy in the hybrid CI Hamiltonian. Introducing the off-diagonal scaling serves to damp out, or remove dynamic correlation energy contribution from the CI calculation. By using a damping factor that depends on the energy difference between CSFs, the hybrid model leaves interactions between degenerate or nearly degenerate CSFs intact, which forms the bulk of the non-dynamic correlation energy contributions. Interactions between CSFs widely separated in energy, which contribute almost solely to the dynamic correlation energy in the CI calculation are removed. The hybrid DFT/MRCI model damps out the dynamic correlation energy contribution from the CI calculation in an effort to remove the double contribution to this energy from both the DFT and CI models.

The effect of the damping of off-diagonal matrix elements in the effective CI Hamiltonian in the Grimme and Waletzke approach can be examined through analysis of a few simple systems with known analytical solutions. The effect of scaling on the eigenvalues, in particular, on the degeneracy between eigenvalues can be illustrated by examining one 4-by-4 matrix arising from the coupling of angular momentum between two electrons. The effect of variation of the two independent damping parameters, p_1 and p_2 on the absolute error between the approximate eigenvalues and exact eigenvalues can be explored by examining a fictitious two level system. The off-diagonal damping inherent to the Grimme and Waletzke approach can be generalized by the function

$$D(p_1, p_2, \omega, w, \omega', w') = p_1 e^{-p_2 \Delta E_{ww'}^q} \langle \omega w | \hat{H} - E^{HF} | \omega' w' \rangle, \quad (78)$$

Here, q was added as an additional parameter in the exponent in Equation 78 to investigate the behavior of the damping as the exponent was varied. Examining p_1 , it is apparent that it can range from zero to one. If $p_1 = 0$, then the off-diagonal matrix elements are eliminated, and one is left with only the diagonal matrix elements for the eigenvalues. For $p_1 > 1$, the CI Hamiltonian can become ill-conditioned, resulting in divergence in the iterative diagonalization method. Regardless of the value of p_2 , p_1 governs the damping applied even when the two interacting CSFs are degenerate. Examining p_2 , it is apparent that in the limit that $p_2 \rightarrow 0$, the damping is governed solely by the value of p_1 . For large values of p_2 , the matrix element will be damped out unless the CSFs are degenerate, or nearly so.

3.1.4.2 Effect of the Damping Term on Eigenvalue Degeneracies. The angular momentum coupling between two electrons is a simple problem that can be used to illustrate the effect the exponent in Equation 78 on the eigenvalues of the system. In the uncoupled angular momentum basis, the operator \hat{S}^2 has the representation, in units of \hbar^2 , of

$$\begin{pmatrix} 2 & 0 & 0 & 0 \\ 0 & 1 & 1 & 0 \\ 0 & 1 & 1 & 0 \\ 0 & 0 & 0 & 2 \end{pmatrix}.$$

Diagonalizing this representation, one obtains

$$\begin{pmatrix} 2 & 0 & 0 & 0 \\ 0 & 2 & 0 & 0 \\ 0 & 0 & 2 & 0 \\ 0 & 0 & 0 & 0 \end{pmatrix},$$

representing a triplet and singlet state. The three eigenvalues for the triplet state are degenerate. Now, applying damping to the off-diagonal elements, of the form

$$f(a) = e^{-a^q}, \quad (79)$$

one can examine the effect the damping has on the eigenvalues. With this damping applied to the first matrix, the analytic form of the diagonalized representation is

$$\begin{pmatrix} 2 & 0 & 0 & 0 \\ 0 & 1+f(a) & 0 & 0 \\ 0 & 0 & 1-f(a) & 0 \\ 0 & 0 & 0 & 2 \end{pmatrix}.$$

Figure 4 shows the values of the eigenvalues $1 + f(a)$ and $1 - f(a)$ as a function of a . For values of $a < 0.5$, the eigenvalues are approximately equal to their unperturbed values, while for large values of a , they revert to the over damped case of zero off-diagonal elements. Varying the exponent affects the step-like nature of the transition between the over damped eigenvalue, where the off-diagonal term is eliminated, and the approximate eigenvalue. Large exponents result in a more step-like transition, smaller exponents result in a smoother transition. A large transition region is less desirable than a smaller one, because one would like the region where the damped eigenvalues are approximately equal to the exact eigenvalues over a large range in the parameter a . It is obvious the exponent necessarily be positive, or severe matrix ill-conditioning could occur. If $q = 0$, the damping is independent of the diagonal integrals of the interacting CSFs, which is undesirable. For $q = 2$, there is almost no region where the eigenvalue degeneracies are approximately maintained. For $q = 4$ and above, there exists a region where eigenvalue degeneracy is maintained, with a rapid, step-like transition to over damping. It must be noted that the DFT/MRCI method will only be able to reproduce eigenvalue degeneracy in an approximate fashion. This will introduce error in electronic excitation energies, as states consisting of multiple,

Figure 4: Eigenvalue Symmetry Breaking in Two-electron Spin Coupling Example

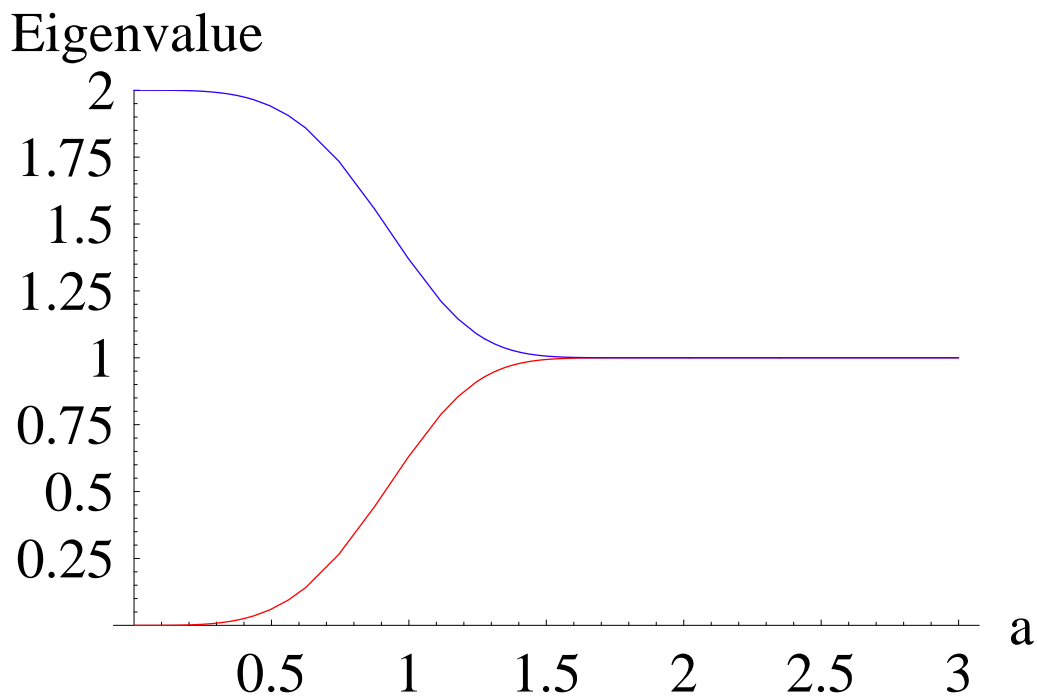
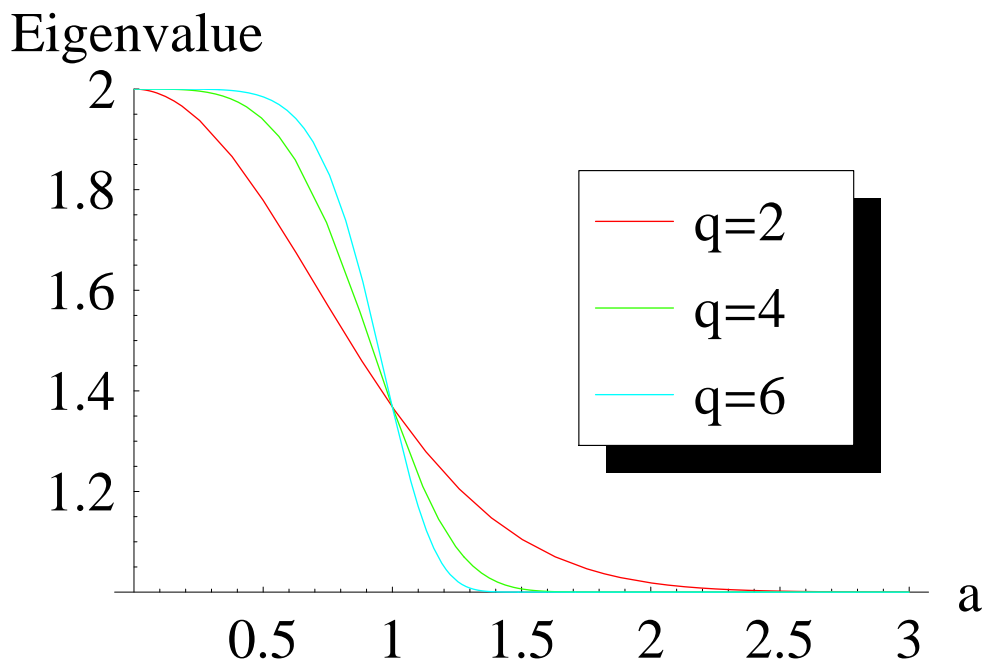


Figure 5: Effect of Exponent on Eigenvalue



degenerate eigenvalues will be split by some amount, resulting in an uncertainty in the energy of the actual state. For spin-orbit calculations, which is one of the objectives of this research, this degeneracy error can mask small spin-orbit splittings.

3.1.4.3 Effect of DFT/MRCI-style Damping on Eigenvalue Absolute Errors. Now that some notion of the effect on the exponent q on the degeneracies of eigenvalues has been investigated for a known system with analytical solutions, it is necessary to explore the effects p_1 and p_2 have on the absolute error between the damped eigenvalue difference and the exact, undamped eigenvalue difference for a two-level system. The two-level system selected with matrix values chosen to represent the values found in a CI Hamiltonian, a diagonally dominant, Hermitian matrix. The matrix, with Grimme and Waletzke damping of the off-diagonal element, is of the form

$$\begin{pmatrix} a & c_0 \cdot p_1 \cdot e^{-p_2(a-b)^4} \\ c_0 \cdot p_1 \cdot e^{-p_2(a-b)^4} & b \end{pmatrix}.$$

Taking the difference between the analytical eigenvalues of this matrix, one gets

$$\Delta E_{DFT/MRCI} = e^{-p_2(a-b)^4} \cdot \sqrt{a^2 e^{-2p_2(a-b)^4} - 2ab e^{-2p_2(a-b)^4} + b^2 e^{-2p_2(a-b)^4} + 4c_0^2 p_1^2}.$$

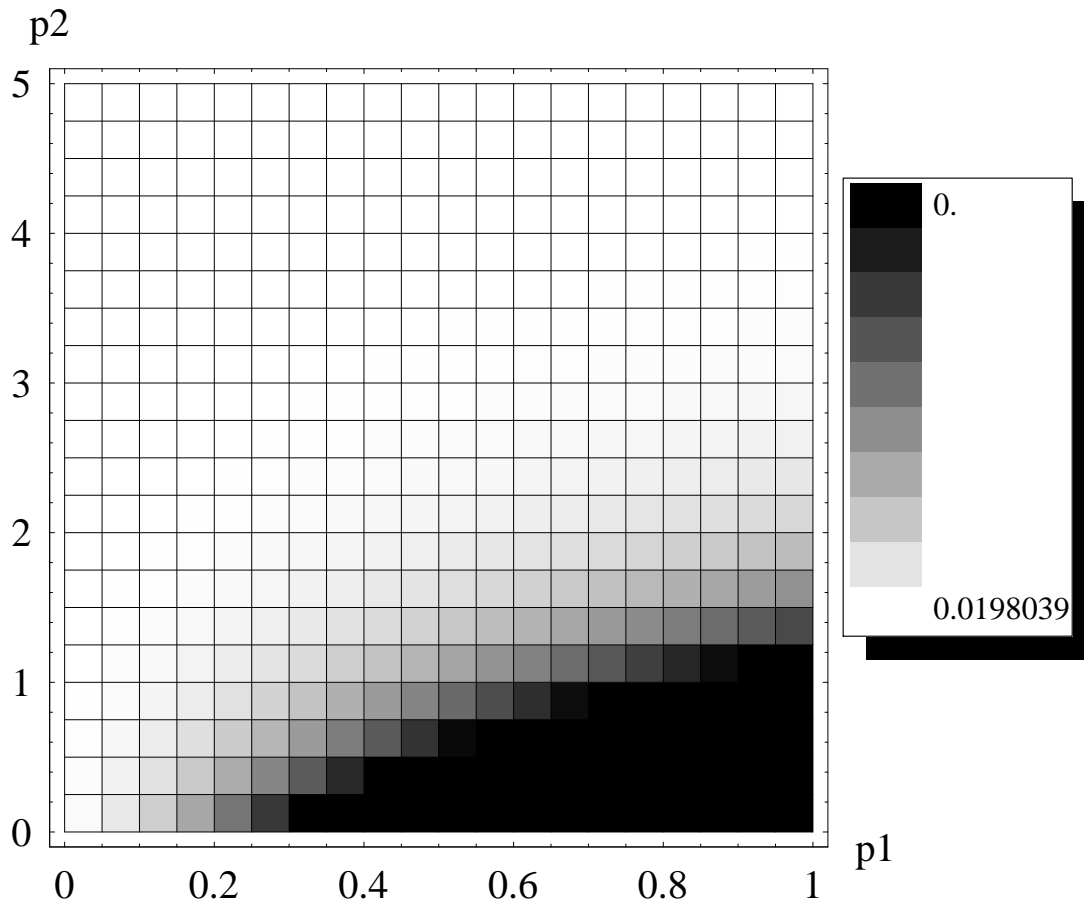
Substituting in values typical of a diagonally dominant CI matrix, $a = -2.0$, $b = -1.0$, $c_0 = -0.1$, an exact value for the eigenvalue difference of 1.0198 is found. Defining the error between the analytical result and the DFT/MRCI result as

$$E(p_1, p_2) = \Delta E_{exact} - \Delta E_{MR-DFT}, \quad (80)$$

one can then explore the error in the p_1 and p_2 parameter space. Figure 6 shows a density plot of the error on a 20 x 20 grid. As expected, the minimum absolute error occurs in the undamped case, $p_1 = 1.0$, $p_2 = 0.0$, where the approximate eigenvalues are equal to the analytical eigenvalues. The error in the density plot for this 2-by-2

matrix ranges from 0.0 to 19.8 milli units in the range examined in the plot. The absolute error remains lowest for $p_1 > 0.3$ and $p_2 < 1.2$.

Figure 6: Density Plot of Absoulte Error Between Exact ΔE and Damped ΔE



3.2 DFT/MRCI Model Implementation with COLUMBUS

This chapter will describe the theory, development, testing, and validation of the the DFT/MRCI method within COLUMBUS, modified from the original model developed by Grimme and Waletzke [63]. For reference, the various program steps involved in performing a CI calculation in COLUMBUS are

1. Compute atomic orbital integrals using ARGOS

2. Perform ROHF SCF calculation to obtain molecular orbitals using SCFPQ
3. Generate the distinct row table for the specified CI expansion using CIDRT
4. Transform the atomic orbit integrals into molecular orbital integrals using TRAN
5. Sort the molecular orbital integrals into their various loop contributions (all-internal through four-external plus spin-orbit integrals) and compute repartitioned Hamiltonian core energy with CISRT
6. Perform the MR-SOCISD calculation using CIUDG

3.2.1 Density Functional Theory Interface to COLUMBUS. The similarity between the basic structure of Kohn-Sham self-consistent density functional theory and the HF codes was pointed out earlier in this chapter. This similarity is one reason for the success of DFT, in that many of the computational algorithms designed for HF calculations could be reused. COLUMBUS contains an ROHF code, SCFPQ, but no DFT capability.

The best approach would be to implement a fully self-consistent numerical integration scheme within SCFPQ. In this way, correlation potential integrals, which are used in the construction of the Kohn-Sham effective Fock matrix, and correlation energy, which are used to obtain the total DFT energy, are obtained from the one- and two-electron densities at each iteration. However, implementing, validating, and testing a new numerical matrix element evaluation scheme was simply not possible within the time available.

Instead, a different approach was taken, consisting of designing and implementing an interface between another well-documented, validated, and tested DFT code, allowing the use of the DFT specific elements in the Fock matrix in the ROHF code SCFPQ within COLUMBUS, as well as in the molecular integral sorting program CISRT, so that the CIUDG code could proceed using Kohn-Sham molecular orbitals and the correlation energy.

The basic elements that must be included in this interface between programs were the one-electron correlation integrals, V_c and the correlation energies, E_c . The correlation potential integral matrix elements are obtained by numerically integrating the functional derivative of the correlation functional with respect to the density,

$$V_{ij}^c = \left\langle \varphi_i \left| \frac{\delta F_c[\rho]}{\delta \rho} \right| \varphi_j \right\rangle, \quad (81)$$

where φ_i are atomic orbital basis functions. The correlation energy is obtained by numerical integration of the correlation density functional over all space,

$$E_c = \int F_c[\rho] d\tau. \quad (82)$$

In order to obtain the correct Kohn-Sham molecular orbital coefficients, V_{ij}^{xc} must be included in the one-electron effective Fock matrix during the self-consistent iterations. Once self-consistency is achieved, and the total DFT energy is computed, the correlation potential integrals are removed from the one-electron Fock matrix, and the correlation energy is added. Failure to do this would yield the incorrect total energy. The one-electron contribution to the total Hartree-Fock energy is computed from the expression [127, 176]

$$E_1^{HF} = \frac{1}{2} \sum_{\mu} \sum_{\nu} P_{\mu\nu} H_{\mu\nu}^{core}, \quad (83)$$

with

$$H_{\mu\nu}^{core} = \left\langle \mu \left| -\frac{1}{2} \sum_{i=1}^N \nabla^2 - \sum_{i=1}^N \sum_{a=1}^M \frac{Z_a}{r_{ia}} \right| \nu \right\rangle. \quad (84)$$

The one-electron charge density matrix, $P_{\mu\nu}$ is given by [127, 139]

$$P_{\mu\nu} = 2 \sum_a^{N/2} C_{\mu a} C_{\nu a}^*, \quad (85)$$

where $C_{\mu a}$ are the basis contraction coefficients. However, in Kohn-Sham DFT, $H_{\mu\nu}^{core}$ is given by

$$H_{\mu\nu}^{core} = \left\langle \mu \left| -\frac{1}{2} \sum_{i=1}^N \nabla^2 - \sum_{i=1}^N \sum_{a=1}^M \frac{Z_a}{r_{ia}} + V_{\mu\nu}^c \right| \nu \right\rangle, \quad (86)$$

while the total DFT energy is given by

$$E_1^{KS} = \frac{1}{2} \sum_{\mu} \sum_{\nu} P_{\mu\nu} (H_{\mu\nu}^{core} - V_{\mu\nu}^c) + E_c, \quad (87)$$

with E_c defined in Equation 82. The main difference between the Hartree-Fock and Kohn-Sham energies is that the Kohn-Sham total DFT energy is not obtained by contracting the density matrix with the correlation potential integrals, but through integration of the correlation density functional over all space. Thus, by extracting the correlation potential integrals and correlation energy from a converged Kohn-Sham DFT calculation, one can reproduce the density functional theory calculation in a Hartree-Fock program.

The first part of the interface required the extraction of the correlation potential integrals and energies from `NWChem`. This was achieved by slightly modifying the `xc_getv.F` code, located in the `\src\nwdft\xc` directory in version 4.7. The correlation potentials and energy are extracted from the calculation by setting the following variables

```
set "dft:idecomp" 2
```

anywhere in the `NWChem` input file, outside of any specific blocks. This forced `NWChem` to separately compute the exchange energy and the correlation energy in a `NWChem` calculation, rather than combine the two energies in a single value. Next, within the DFT block, the following keywords enable the creation of the `xcints` file:

```
dft
  print high
  print "xc matrix"
```

end.

The code modifications to `xc_getv.F` are placed after the numerical integration of the density functional is performed in the call to subroutine `grid_quadv0`, at line 332.

The modified code is

```

        if (oprint_xc_matrix)then
            write(luout,*)'True Vxc'
            call ga_print(g_truevxc)
            write(luout,*)'EVB Exc energy = ',
                .          0.5d0*ga_ddot(g_dens(1),g_truevxc)

            call ga_get(g_truevxc(1),1,nbf_ao,1,nbf_ao,
                $          temp_vxc,nbf_ao)

            open(unit=66,file='xcints',status='replace')

cevb          write out exchange-correlation energy, can't reproduce it

            write(66,fmt='(2f20.10)') Exc(1), Exc(2)
            write(66,fmt='(i4)') nbf_ao

            do i_row = 1, nbf_ao
                do j_column = 1, i_row
                    write(66,fmt='(2i4,f15.9)') i_row, j_column,
                $          temp_vxc(i_row,j_column)
                enddo
            enddo

            close(66)

```

endif.

The next step was to develop the input interface for the SCFPQ program to input data from the `xcints` file and use the data in the appropriate places. The interface code was written in Fortran 95 and is contained in the module file `nwchem_interface_mod.F90`. The interface works in the following way:

1. The COLUMBUS SCFPQ code must be compiled with the preprocessor definitions `-DEVB_MULTIREFERENCE_DFT` and `-D90` activated.
2. If the `xcints` file is not present, the SCFPQ code defaults to ROHF default behavior.
3. Before the first iteration of the SCF cycle, if the `xcints` file is present, it is opened, and the contents, E_x , E_c , and V_{ij}^{xc} are read into memory.
4. V_{ij}^c are added to the one-electron Fock matrix, H_{ij}^{core} for use in the SCF iterations. The potentials are not included when the SCF energy is computed. E_c is added to the total energy instead.

The design of this file-based interface was written to be general enough to facilitate the introduction of any set of one-electron potentials to the Fock matrix. This could facilitate further extensions to the SCFPQ code, for example, in adding a simple solvation model.

There is a potential for mismatch between SCFPQ and NWChem when using this file-based interface, especially in open-shell atomic and molecular systems. For closed-shell systems, NWChem uses a restricted Kohn-Sham algorithm, which interfaces nearly seamlessly into the restricted Hartree-Fock algorithm used in SCFPQ. For open-shell systems, however, SCFPQ uses a ROHF algorithm, while NWChem uses an unrestricted Kohn-Sham algorithm. In the unrestricted case, the α and β orbitals are no longer constrained to remain degenerate, as is the case in the restricted and restricted-open algorithms. The correlation potential integrals may still be used in the file-based interface method, due to the fact that the correlation potential integral matrix are

integrals over basis functions, not molecular orbitals. However, the resulting molecular orbital energies, coefficients, and the total energy obtained from the unrestricted Kohn-Sham calculation and the modified ROHF method will necessarily differ. In most cases examined, the discrepancy in the total DFT energy was small. This discrepancy could be eliminated by implementing an *in situ* correlation numerical integration capability with SCFPQ.

Another mismatch is in the normalization of the atomic orbital integrals in the NWChem and SCFPQ programs. NWChem normalizes atomic orbital integrals to unity, while ARGOS, the one- and two-electron integral program in the COLUMBUS program normalizes atomic orbitals to a value dependent on the angular momentum value of the shell the atomic orbital is in. For example, for a Gaussian orbital of the form

$$x^m y^n z^l e^{-\alpha r^2}, \quad (88)$$

where the orbital angular momentum, L for the atomic orbital is given by $m + n + l$, then the COLUMBUS atomic orbital normalization factor is $(2m - 1)!!(2n - 1)!!(2l - 1)!!$. The $(...)!!$ is the odd factorial, defined by $(2m - 1)!! = (2m - 1)(2m - 3)\dots(1)$. This normalization ensures that orbitals in the same shell have the same normalization, and is identical to NWChem normalization for shells with angular momentum $L < 2$. A normalization conversion had to be incorporated into SCFPQ to ensure that the correlation potential integral normalization was consistent. This was accomplished by multiplying the NWChem correlation potential integrals by the COLUMBUS normalization factor.

Although both programs can exploit Abelian point group symmetry, each program approaches symmetry in a slightly different fashion. NWChem uses a projection operator approach, projecting out the various irreducible representations from the state vector. On the other hand, SCFPQ explicitly works in a symmetry-adapted atomic orbital basis. In this basis, the Fock matrix is block diagonal, and there is no symmetry contamination in the state vector. Developing a one-to-one interface

between the two programs that incorporated point group symmetry as well proved to be too complicated to accomplish in the scope of this research. As a result, all interface calculations must be performed in the C_1 Abelian point group at this time.

3.2.1.1 DFT Interface Validation. Table 10 lists the total DFT energies produced from both `NWChem` and the modified version of `SCFPQ` for atomic and diatomic systems over a range of ground state multiplicities. The doublet and triplet systems are open-shell atoms, and are calculated using an unrestricted Kohn-Sham DFT treatment in `NWChem`, but with the modified ROHF method described above in `SCFPQ`.

Open-shell atomic cases were calculated in `SCFPQ` using a set of high-spin open-shell coefficients, but with the correlation potential integrals and energy from an unrestricted Kohn-Sham DFT calculation. As expected, this mismatch introduces a slight discrepancy into the DFT energy produced by `SCFPQ`. The discrepancy between the `NWChem` and `SCFPQ` DFT results for the closed-shell molecules is due to a slight geometry mismatch between the two calculations. This mismatch is a result of a different conversion factor between bohrs and angstroms being used by the two programs. The mismatch produces a very slight difference in nuclear repulsion energies of the molecules. This small bond length variation propagates into all one- and two-electron integrals, resulting in the 10^{-4} to 10^{-5} Hartree variation in DFT energies between the two programs.

Table 10: SCFPQ + V_{xc} and NWChem DFT Energies, CPBE96 Correlation Functional

Molecule	State	Basis Set	NWChem Total energy(au)	Modified SCFPQ Total Energy(au)
He	1S	cc-pVDZ	-2.8974314	-2.8974314
He	1S	cc-pVTZ	-2.9033415	-2.9033415
Be	1S	cc-pVDZ	-14.6581093	-14.6581092
Be	1S	cc-pVTZ	-14.6587689	-14.6587689
Ne	1S	cc-pVDZ	-128.8418547	-128.8418547
Li	2S	cc-pVDZ	-7.4839186	-7.4839114
Li	2S	cc-pVTZ	-7.4842048	-7.4841740
B	2P	cc-pVDZ	-24.6431084	-24.6397244
C	3P	cc-pVDZ	-37.8316781	-37.8276148
N	4S	cc-pVDZ	-54.5721139	-54.5695753
O	3P	cc-pVDZ	-75.0289806	-75.0230910
F	2P	cc-pVDZ	-99.6694840	-99.6653580
Br	$^2P_{\frac{3}{2}}$	cc-pVDZ + ECP	-153.8323299	-153.8282959
U ⁴⁺	3H_4	cc-pVDZ + ECP	-213.4131032	-213.3284656
U ⁵⁺	$^2F_{\frac{5}{2}}$	cc-pVDZ + ECP	-211.6726845	-211.6114783
H ₂	1S	cc-pVDZ	-1.1738196	-1.1738196
H ₂	1S	cc-pVTZ	-1.1768602	-1.1768601
CO	$^1\Sigma^+$	cc-pVTZ	-113.2326231	-113.2326535
Be ₂	$^1\Sigma_g^+$	cc-pVDZ	-29.3137214	-29.3137193
BF	$^1\Sigma_0^+$	cc-pVTZ+ ECP	-27.0113630	-27.0113971
UO ₂ ²⁺	$^1\Sigma_{0g}^+$	cc-pVDZ + ECP	-247.2848488	-247.2849113

3.2.2 Correlation Energy in the Repartitioned Hamiltonian. Once a set of pseudo-Kohn-Sham orbitals is generated through the file-based interface between NWChem and SCFPQ, the distinct row table for the CI calculation is generated using the CIDRT program, and the integrals over atomic orbitals are transformed into a molecular orbital basis using the TRAN program. The only step remaining before actually performing the CI calculation is to sort the molecular integrals into all-internal, one-external, two-external, three-external, and four-external orbital index sets and compute the reference energy of the repartitioned Hamiltonian. This sorting is accomplished by the CISRT program.

The critical component in an DFT/MRCI calculation is the addition of the correlation energy needs to the reference energy. This is accomplished through the file-based interface, `xcints`. In a similar fashion to the modified ROHF program, the modified CISRT program performs the following:

1. The COLUMBUS CISRT code must be compiled with the preprocessor definitions `-DEVB_MULTIREFERENCE_DFT` and `-D90`.
2. If the `xcints` file is not present, the CISRT code defaults to its default behavior.
3. If the `xcints` file is present, it is opened, and the contents, E_x , E_c are read into memory.
4. E_c is added to the reference energy of the repartitioned Hamiltonian.

This final step adds the correlation energy to the reference energy, effectively offsetting the energies produced in the CIUDG program by E_c . For a single root, ground state calculation, with zero excitations from the reference space, this reproduces the DFT energy result obtained in the modified SCFPQ program exactly. A more ideal approach would be to recompute the correlation energy contribution based on the orbital density for each reference. This approach would allow a more reasonable approximation to the correlation energy for each reference, rather than use the correlation energy obtained from the ground state density and applied to all reference configurations, which may give rise to vastly different densities.

3.2.3 CIUDG Based DFT/MRCI. The third and final step in the implementation of the DFT/MRCI method required modification of the CI program, CIUDG, in order to implement the damping of the off-diagonal CI matrix elements.

3.2.3.1 Modifications to the Grimme and Waletzke DFT/MRCI Model.

In their paper [63], Grimme and Waletzke describe an approach to the development of a hybrid DFT-CISD model. Their approach, based on a selected-CI code, involved modification of both the diagonal and off-diagonal CI Hamiltonian matrix elements. The fact that they used a selected-CI code enabled them to select which CSFs to include in their CI expansion. The DFT/MRCI model and their CSF selection criteria allowed them to drastically reduce the size of the CI expansions necessary to examine systems of interest. The rationale behind this is the fact that the DFT calculation captures a large fraction of the dynamic correlation energy, and so only a modest CI expansion is necessary to model the non-dynamic correlation contribution to the energy.

The approach they described in their paper involved a hybrid correlation functional, half exact HF exchange and half Becke 1988 [11] exchange functional, coupled with the Lee, Yang, and Parr [81] GGA correlation functional. Their resulting DFT/MRCI model contained five unknown parameters, shown in chapter two, equations 75, 76, and 77.

In this model, however, only the off diagonal matrix element damping was retained. The rationale behind this was that modifications to the diagonal CI matrix elements were necessary due to the use of an approximate, local exchange functional. Using a correlation-only functional and eliminating the modifications to the diagonal matrix elements reduced the number of empirical damping parameters to two. However, using the exact Hartree-Fock exchange operator with Kohn-Sham orbitals does not reproduce the exact exchange energy. Most successful hybrid density functionals mix exact Hartree-Fock exchange for the non-local contribution with a portion of local exchange energy obtained from the exchange functional. Perdew and Ernzerhof sug-

gest a rationale for mixing 15% to 30% exact Hartree-Fock exchange with 70% to 85% local density functional approximation [102]. Grimme and Waletzke use the BLYP density functional approximation, which mixes 50% exact exchange with 50% Becke exchange density functional approximation. A popular and accurate hybrid density functional, Becke Three Parameter Hybrid Density Functional (B3LYP) mixes 20% Hartree-Fock exchange with 72% Becke exchange. Using a correlation only functional and 100% exact Hartree-Fock exchange simplifies the treatment of the diagonal CI matrix elements, and allows a more flexible treatment of various spin multiplicities, without resorting to additional parameterization of the method, in exchange for some error in the exchange energy contribution.

Full advantage was taken of the loop-driven approach in CIUDG in implementing the damping of the off-diagonal matrix elements. By taking care to identify the individual CSFs participating in a particular one- or two-body loop interaction within Configuration Interaction Unitary Diagonalize (CIUDG), and applying the scaling appropriately based on Equation 77, the overall scaling factor for each off-diagonal element can be constructed in a factored form. In the GUGA approach to CI calculations, the various contributions to the CI Hamiltonian are constructed from the product of individual segment values within the loop [120, 73] [124].

Off-diagonal matrix element scaling is introduced through a scaling factor, $\rho(i, j)$ applied to both one- and two-body segments, defined by

$$\rho(i, j) = p_1 e^{-p_2 \Delta E_{ij}^A}, \quad (89)$$

where ΔE_{ij} is the diagonal integral difference between CSF i and CSF j . This results in new one- and two body generator matrix elements,

$$\langle m' | E_{ij} | m \rangle = \prod_{k=(i,j)} \rho(i, j) \omega(Q_k; d'_k d_k, \Delta b_k, b_k) \quad (90)$$

and

$$\langle m' | e_{ij,kl} | m \rangle = \prod_{p \in S_1} \rho(i, j) \omega(T_p, b_p) \sum_{x=0,1} \prod_{p \in S_2} \omega_x(T_p, b_p). \quad (91)$$

3.2.3.2 CIUDG based DFT/MRCI Model Validation. The critical step in implementing the method was to correctly identify the interacting CSFs in each loop contribution. One of the efficiencies of the loop-driven approach to CI calculations in the GUGA approach is a result of the compact nature of the DRT. Large CI expansions can be compactly described with compact DRT tables without having to form and store an index vector of the same dimension as the CI expansion. Such compactness is desirable in very large CI expansions, as forming and storing an index vector of millions, or billions of elements long is highly inefficient.

The loop-driven approach indexes loop contributions to internal walks, which are all the walks through the DRT of the occupied reference space. The regular structure of the external space (see Figure 1) is exploited for code efficiency. These internal walks terminate at the beginning of the external space on either Z, Y, X, or W vertices. The CIUDG code is organized according to the types of loop contributions, based on the excitation level with respect to the internal space. A maximum of two orbitals can contribute to one-body loop types, while a maximum of four orbitals can contribute to two-body loops. Calculations proceed in order, computing the following loop type contributions to the CI Hamiltonian:

1. **Four-external loops** – All four orbitals contributing to this loop are in the external (virtual orbital) space. The structure of these matrix element contributions to the CI Hamiltonian can be either a single matrix element, a row or column of matrix elements, or a $m \times m$ block of matrix elements. There are 16 separate locations in the code that perform this type of interaction, based upon the symmetry of the bra and ket CSFs.
2. **Three-external loops** – One orbital is in the internal space, three orbitals are in the external space. The structure of these matrix element contributions to

the CI Hamiltonian can be either a row or column of matrix elements, or a m x m block of matrix elements. There are 9 separate types of this interaction in the code.

3. **Two-external loops** – Two orbitals are in the internal space, two orbitals are in the external space. The vast majority of these matrix element contributions to the CI Hamiltonian are in the form of m x m block of matrix elements, with only one row or column vector contribution. There are 20 separate types of this interaction in the code.
4. **One-external loops** – Three orbitals are in the internal space, and one orbital is in the external space. All these contributions are either row or column vectors in the CI Hamiltonian. There are 6 types of this loop interaction in the code.
5. **All-internal loops** – All four orbitals in the interaction are in the internal space. There are 4 types of this loop interaction in the code, with the contributions appearing as either a single CI matrix element, or a co-diagonal vector.
6. **Spin-orbit integral loops** – Since the spin-orbit operator is a one-body operator, there can only be two- and one-external loop types of this, in addition to all-internal spin orbit loops. These interactions were not modified in this implementation.

For each loop type, the CSFs involved was based upon the sum of the CSF offset for each internal walk and the CSF offset for the number of CSFs involved in the interaction. Each loop contribution eventually ends with a Basic Linear Algebra System (BLAS) subroutine call to update the sigma vector from the CI vector. This update is usually of the form

$$\vec{\sigma} = \hat{H} \cdot \vec{c}. \tag{92}$$

The CSFs involved in the update were identified through the CSFs involved in both the $\vec{\sigma}$ vector and \vec{c} vector, as the Hamiltonian, \hat{H} is never explicitly constructed. In the CIUDG code, both the sigma and CI vectors are indirectly indexed, with locations

in the vectors defined and controlled as offsets to the starting CSF for the internal walks in the interaction. The internal walks are organized according to the Z, Y, X, or W walk vertex upon which they terminate. Z and Y walks are listed first, so Z walks always begin at CSF number 1. The starting CSFs of the Y, X, and W walks are also stored, but only for the internal walks. So the starting CSFs for the sigma and CI vectors in an all-internal interaction between two Y walks would occur at the internal Y walk start CSF. The range of CSFs involved in the interaction is then deduced by the type of BLAS subroutine call. In the YY walk all-internal interaction example, the sigma vector update is performed by the pair of BLAS subroutine calls

```
call daxpy(ny, hint, ciket(nmb2+1), 1, sigmabra(nmb1+1), 1)
call daxpy(ny, hint, cibra(nmb1+1), 1, sigmaket(nmb2+1), 1).
```

All sigma vectors get updated in this pairwise fashion, which takes advantage of the Hermitian nature of the CI Hamiltonian to update the sigma vector in two places, one update due to the lower triangle of the CI Hamiltonian, the other due to the contribution from the upper triangle of the Hamiltonian. In the YY interaction example, the `daxpy` subroutine call performs the following operation:

$$\vec{y} = a * \vec{x} + \vec{y}, \tag{93}$$

where a is a scalar, \vec{x} and \vec{y} are both vectors. In the code segment above, the dimension of these vectors are `ny` and the offsets to the internal Y walk starting CSFs for each are `nmb2+1` and `nmb1+1`. The scalar a is `hint`. In this example, `hint` is the CI Hamiltonian matrix element, and the shape of this interaction in the Hamiltonian is a co-diagonal vector. Unrolling this loop so that off-diagonal matrix element scaling can occur, along with the update of the sigma vector is performed by the following code,

```
hint_original = hint
```

```

do temp=1, ny

    call scale_scalar(cist(2)+nmb1+temp, &
    cist(1)+nmb2+temp, hint)

    sigmabra(nmb1+temp)=sigmabra(nmb1+temp)+&
        hint*ciket(nmb2+temp)
    sigmaket(nmb2+temp)=sigmaket(nmb2+temp)+&
        hint*cibra(nmb1+temp)

    hint = hint_original

end do.

```

Hence, the indices of the Hamiltonian matrix element referred to in the code by `hint` is given by the sum of the Y walk starting CSF in both the CI vector and the sigma vector, and the offset from these starting CSFs. For the CI vector, this sum is `cist(1)+nmb2+temp` while for the sigma vector, the sum is `cist(2)+nmb1+temp`.

Careful analysis along these lines of all the loop BLAS calls allowed reconstruction of the absolute CSFs involved in each interaction from the various offsets.

From the BLAS routines used to update the sigma vector, the possible types of CI matrix elements are:

1. Scalar – A single CI matrix element contributes to the $\vec{\sigma}$ update.
2. Vector – Either a row or column of matrix elements contribute to the $\vec{\sigma}$ update. These vectors are either $n \times 1$ or $1 \times m$ in size.
3. Block – An $n \times n$ block of matrix elements contributes to the $\vec{\sigma}$ update.

Three separate scaling routines were written to account for each case listed above.

For the block matrices and vectors, there were several locations in the `CIUDG` code where significant optimization of the $\vec{\sigma}$ vector update occurs. In these areas, it was not possible to identify what the CSF locations of the matrix elements were in general expansion. These cases occur in the `CIUDG` code where the CI vector gets either symmetrically or asymmetrically expanded into an $n \times n$ matrix. In these cases, the update of the sigma vector no longer takes the form of Equation 92. Instead, the sigma vector gets updated in a complicated matrix/matrix product fashion. For these loop types, involving a small number of external orbitals, with one, two, or three external basis functions, the optimization could be unrolled, and the sigma update reformulated in terms of a matrix/vector product, where identification of the CSFs is then possible. However, no general pattern arose in the assignment of CSFs to matrix elements.

Because of this non-unique usage of the two-electron molecular integrals in the update of the σ vector, the implementation of the Grimme and Waletzke DFT/MRCI approach required slight modification in the GUGA based CI code. In these cases, which arise in two of the six one-external loops, and six of the twenty two-external loop types, a different approach was taken. For these blocks of matrix elements, if the dimension of the block is greater than one, a single scaling factor is applied to the entire block of matrix elements. Three scaling choices are possible, and they are selectable in the input file via a logical flag: minimum scaling, maximum scaling, or average scaling. In these cases, the ranges of CSFs in the block can be deduced in general, however, the matrix elements within the block are not uniquely used, which precludes damping them individually. Instead, based on the CSF range, and the flag chosen in the input file, the entire block of matrix elements gets damped by the same factor. This is a more efficient method for damping these highly optimized cases, and is necessary for two reasons. First, in these blocks, matrix elements are not used uniquely in the block. The same integral contributes to more than one matrix element, precluding individual, unique damping. Second, because of the optimization, linear combinations of integrals contribute to the block, with each integral contribution within a linear

combination possibly having differing CSF indices. Block damping the entire group of matrix elements by a single factor, by either the maximum, minimum, or average damping factor based on the CSF range of the block was the way that code efficiency was preserved.

Additionally, it is simply not feasible to single out specific CSFs for inclusion in the CI expansion in the loop-driven, GUGA-based CI code, *CIUDG*. However, reduction in the size of the CI expansion is one of the most important factors in the Grimme and Waletzke model. Rather than selectively include CSFs in the expansion, as Grimme and Waletzke did using their CI code, expansion size in *CIUDG* is limited by freezing orbitals in the virtual space, using the rationale that high energy virtual orbitals contribute very little to the non-dynamic correlation energy.

3.2.4 Testing the DFT/MRCI Model Implementation within CIUDG. Using the fact that the absolute CSFs of both the sigma and CI vectors involved in the interactions could be reconstructed, an internal consistency check was coded into *CIUDG*. This check worked by constructing the Hamiltonian from the loop contributions and their absolute CSFs. This Hamiltonian was then diagonalized, and the eigenvalues were compared to the eigenvalues obtained from the iterative Davidson diagonalization of the subspace matrix. Incorrect indexing of the CSFs resulted in incorrectly placing the matrix element within the consistency check Hamiltonian, and resulted in eigenvalues that did not agree with those obtained iteratively from the subspace matrix.

The CI program never explicitly generates the Hamiltonian, instead, it generates so-called matrix-vector products, $\hat{H}\vec{v}$ directly, where \vec{v} are the reference vectors. The subspace matrix is generated by forming the product $\vec{v}\hat{H}\vec{v}$. In the first iteration, the start vectors are constructed by placing a 1 in the CSF location for that particular vector, with zeros elsewhere. Starting vectors can be generated using Z walks, or Z and Y walks, defining the set of reference vectors upon which to generate the subspace matrix. The subspace matrix and CI Hamiltonian are equal in this case during the

first iteration. As the starting vectors converge in subsequent iterations, this is no longer true.

This behavior of the subspace matrix was exploited for testing purposes, and code was added to generate start vectors for all Z, Y, W, and W walks (accessed by setting `ISTRIT=3`, `IVMODE=1` in the `ciudgin` namelist input file). As explained above, this allowed construction of a subspace matrix that corresponded to the exact CI Hamiltonian. This exact Hamiltonian was used as a reference to aid in the determination of absolute CSF locations.

A series of very small test systems were used to generate and test the determination of absolute CSF assignments. By setting $p_1 = 1.0$ and $p_2 = 0.0$, the off-diagonal elements were unaffected, and the consistency check Hamiltonian and the exact Hamiltonian could be compared, facilitating debugging of the DFT/MRCI code. A series of systems with very small basis sets were used to facilitate this, so that the entire CI Hamiltonian could be visualized. The atomic systems used to perform this testing, along with their basis sets and point group symmetry are listed in Table 11.

Table 11: DFT/MRCI Testing Cases

Atom	Multiplicity	Basis	Point-group symmetry	CI Irrep	CI dimension
He	singlet	[4s1p]/(3s1p)	C_1	A	15
He	singlet	[4s1p]/(3s1p)	D_{2h}	A_g	6
He	singlet	[4s1p]/(3s1p)	D_{2h}	B_{1u}	2
He	triplet	[4s1p]/(3s1p)	C_1	A	10
Li	doublet	[8s3p]/(2s1p)	C_1	A	32
Li	doublet	[8s3p]/(2s1p)	C_i	A_g	20
Li	doublet	[8s3p]/(2s1p)	C_i	A_u	12
Li	doublet	[8s3p]/(2s1p)	C_{2v}	A_1	12
Li	doublet	[8s3p]/(2s1p)	D_{2h}	A_g	8
Li	doublet	[8s3p]/(2s1p)	D_{2h}	B_{1g}	4
Li	doublet	[8s3p]/(2s1p)	D_{2h}	B_{1u}	4
Be	singlet	[9s4p]/(3s2p)	C_1	A	105
Be	singlet	[9s3p]/(3s1p)	D_{2h}	A_g	15
Be	singlet	[9s3p]/(3s1p)	D_{2h}	B_{1g}	4
Be	singlet	[9s3p]/(3s1p)	D_{2h}	B_{1u}	6

The total number of directly tested loops in the above cases is given in Table 12. The loops involving the block scaling technique described above could not be tested in this fashion, and were not included in the loop totals. Two one-external loops and six two-external loops used this block-scaling method. Direct testing means that the loops were directly involved in the CI calculation.

Based on the type of BLAS calls involved in the directly tested loops, a number of remaining, untested loops could be inferred to be scaling correctly, since they involve the same BLAS subroutine calls as a directly tested loop. Recall the off-diagonal damping depends only on the CSFs of the matrix element, and these CSFs are determined by the shape of the CI Hamiltonian block, which is determined by examination of the BLAS subroutine call. A loop is considered indirectly tested if it consists of the same pair of BLAS subroutine calls as a directly tested loop.

Table 12: Testing Results

Loop-type	Number directly tested	Number indirectly tested	Total number of loops	Percent Total direct + indirect
All-internal	3	1	4	100%
One-external	3	1	4	100%
Two-external	7	5	14	86%
Three-external	4	5	9	100%
Four-external	8	0	16	50%
Total	25	12	66	79%

Interestingly, cases which exposed the remaining untested loops could not be found by changing the multiplicity or the symmetry in the above cases. The only way to expose these untested loops was to increase the size of the basis set. However, increasing the size of the basis set made it nearly impossible to examine the CI matrix from the subspace projection, it became too large.

Based on the results listed in Table 12, the operation of the majority of the DFT/MRCI code was verified to be correct. Following the testing of the developed code, application of the DFT/MRCI model to various atomic and molecular systems to assess the performance could commence.

3.3 Using the COLUMBUS DFT/MRCI Model

3.3.0.1 DFT/MRCI Model Input Control. Input to the COLUMBUS-based DFT/MRCI model is contained in the input to the CIUDG program. Activation of the DFT/MRCI code and control of its various features is accomplished by a series of flags, added to the name list input file for CIUDG, `ciudgin`. The default behavior of the CIUDG code is to not perform DFT/MRCI calculations. DFT/MRCI capability has to be specifically activated in order to perform a DFT/MRCI calculation. As in was the case with the modified SCFPQ and CISRT programs, in order to perform a DFT/MRCI calculation, the CIUDG program must be compiled with the preprocessor definitions `-DEVB_MULTIREFERENCE_DFT` and `-D90`. The following input flags, along with example values, are possible in the `ciudgin` file to control the behavior of the DFT/MRCI code:

```
p1 = 0.96
p2 = 2.5
scale_power = 4
od_allint_damp = .t.
od_1ext_damp = .t.
od_2ext_damp = .t.
od_3ext_damp = .t.
od_4ext_damp = .t.
coarse_scaling = 'minimum'
dump_diag = .f.
debug_file = .f.
loop_track = .f.
```

The first three input flags, control the off-diagonal damping of the CI matrix elements. The `scale_power` flag sets the exponent on the ΔE term in Equation 77. The four `od*_damp` flags activate the damping of the various loop contributions. Each individual loop type (all-internal, one-external, etc.) can be selectively damped. The next flag, `coarse_scaling` controls the block scaling in the eight optimized loop interactions discussed earlier. Three choices exist for this flag: `'minimum'`, which scales the entire block by the minimum damping factor, `'average'`, which damps the entire block of loop interactions by the average damping factor for the entire block, and `'maximum'`, which applies the largest damping factor in the block to the entire block of matrix elements. The final three flags are for debugging. Diagonal CSF integrals can be dumped to a human readable file by setting `dump_diag`, while `debug_file` controls dumping of verbose information about the off-diagonal scaling to a human readable text file, and `loop_track` identifies which loop types, as indexed by an arbitrary numeric label, are being accessed in a calculation.

3.3.0.2 Usage. The procedure for using the COLUMBUS-based DFT/MRCI model is listed below. Before proceeding, a version of NWChem with the modifications listed earlier must be compiled in order to extract V_c and E_c from a DFT calculation. A version of COLUMBUS with the DFT/MRCI model needs to be compiled with the pre-processor flags described earlier enabled. The procedure below describes how to use the DFT/MRCI model using a DFT correlation functional and 100% HF exchange. This implementation of the DFT/MRCI model can not be used with a hybrid density functional. Using a mixture of HF and approximate density functional exchange, in the implementation described by Grimme and Waletzke, requires additional modifications to the diagonal matrix elements, which introduce spin-multiplicity limitations to the model.

The first thing that needs to be done is to determine useful values for the two free parameters in the damping term, Equation 78. Appendix B lists the atomic and molecular systems used to determine the two free damping parameters p_1 and p_2 in

Equation 78, for this research. A generic procedure for determining the damping parameters is:

1. Perform FCI calculation on the atomic or molecular system used in the training set. Compute both the ground state and at least one excited state of the same multiplicity. Be sure to use C_1 point group symmetry. **GAMESS** [95] [98] was used in this research to perform the FCI calculations.
2. Using 100% HF exchange and an approximate LDA, GGA, or meta-GGA correlation functional, perform a DFT calculation on the atomic or molecular system used in the training set in order to extract E_c and V_c . Be sure to use C_1 point group symmetry. The external files **overlap** and **xcints** are generated by keywords in the **NWChem** input file described in a previous section.
3. Setting a particular value of p_1 and p_2 in the **CIUDG** input control specified in the next section, run the following series of **COLUMBUS** programs (either individually, or via a script):
 - (a) Generate the atomic orbital integrals using **ARGOS**. Take care to ensure that the symmetry adapted linear combinations of atomic orbital matrices in the **ARGOS** input file match the ordering used in **NWChem**. **NWChem** orders the various orbital shells from lowest to highest m_l value, while the symmetry-adapted linear combination matrices generated automatically by either **IARGOS** or **CIML** arbitrarily order the atomic orbitals.
 - (b) Run the **SCFPQ** program. Be sure the files **xcints** and **overlap** have been generated by **NWChem**. If performing an open-shell calculation, use the unrestricted DFT option in **NWChem**, and use either the average of configurations or high-spin open shell coefficients in **SCFPQ**. The average of configuration open-shell coefficients, along with fractional occupation in open-shell **SCFPQ** calculations better preserve the symmetry of orbitals within the same shell. **NWChem** does not typically perform spherically averaged open-shell calculations in **ROHF** and unrestricted DFT

- (c) Check the total SCF energy from `SCFPQ` and `NWChem` to ensure the DFT energies are in agreement, especially for closed shell cases. Discrepancies here arise typically from an inconsistency in the ordering of the atomic orbital basis in the Fock matrix between the `ARGOS` and `NWChem` programs.
- (d) Examine the orbital energies in the `SCFPQ` output. Determine an acceptable virtual orbital cutoff point based on orbital energies. In this research, an acceptable cutoff was found to range from 30 to 40 eV above the highest occupied molecular orbital. Take care not to freeze orbitals in such a way that symmetry is broken. For example, this can happen if only two of three p degenerate orbitals are frozen in an atomic calculation.
- (e) Generate the DRT using `CIDRT`, freezing virtual orbitals above the cutoff orbital energy in order to limit the size of the CI expansion. This may require several iterations to find a good balance between CI expansion size and DFT/MRCI accuracy. In the GUGA direct CI method, loop contributions are formed directly from one- and two-electron integrals, bypassing explicit construction of the Hamiltonian and CSFs. Limited selection of interacting CSFs can be accomplished in the GUGA approach either through removing specific levels in the DRT, removing specific walks from the DRT, or by freezing virtual orbitals in the external portion of the graph.
- (f) Transform the atomic orbital integrals to molecular orbital integrals using `TRAN`.
- (g) Sort the molecular integrals into internal, external and frozen orbitals and compute the repartitioned Hamiltonian reference energy with `CISRT`. Ensure the file `xcints` is present in order to incorporate the DFT E_c energy into the reference energy.
- (h) Specify the DFT/MRCI specific input in the `CIUDG` input file. At a minimum, p_1 and p_2 must be specified. By default, coarse scaling is selected to be set to `.minimum..` This forces block scaling to be performed using

the minimum damping factor over the entire block of integrals. This was done in order to avoid situations where overly large scaling gets applied to important loop contributions. The drawback is the fact that some loop contributions may not be scaled enough using this scheme.

4. Repeat the COLUMBUS steps above, changing p_1 and p_2 . In this research, a script was used to automatically vary the damping parameters, with p_1 ranging from 0.0 to 1.0, and p_2 ranging from 0.0 to 10.0, both over 20 steps. The excitation energy between the ground and excited state was computed at each value of p_1 and p_2 , and dumped to a file to facilitate the plotting and analysis contained in Appendix B.
5. Compute the difference between the FCI and DFT/MRCI excitation energies for each pair of p_1 and p_2 values computed above.
6. Look for a region in the density plot (Figure 7) of absolute excitation energy error between the FCI and DFT/MRCI that is a minimum, and where p_1 and p_2 decouple. This fixes the value of p_1 . The value of p_2 is selected from an asymptotically flat region of absolute error along this value of p_1 . In this research, using 100% HF exchange and the PBE 1996 GGA correlation functional, with a selection of training systems spanning the first two rows of the periodic table, the damping parameters decoupled at $p_1 = 0.96$. The absolute error for all values of $p_2 > 2.0$ was roughly constant for $p_1 = 0.96$. These considerations led to the selection of $p_1 = 0.96$ and $p_2 = 2.5$ for this research using 100% HF exchange and PBE 1996 GGA correlation functional.

All DFT and TDDFT calculations were performed using the Perdew Burke and Ernzerhof pure correlation functional (CPBE96) correlation functional. Currently, NWChem can not do TDDFT calculations using meta-GGA functionals, limiting this analysis to at most GGA functionals. A small set of test atoms and molecules was selected and used to determine a set of damping parameters that produce acceptable error for all systems.

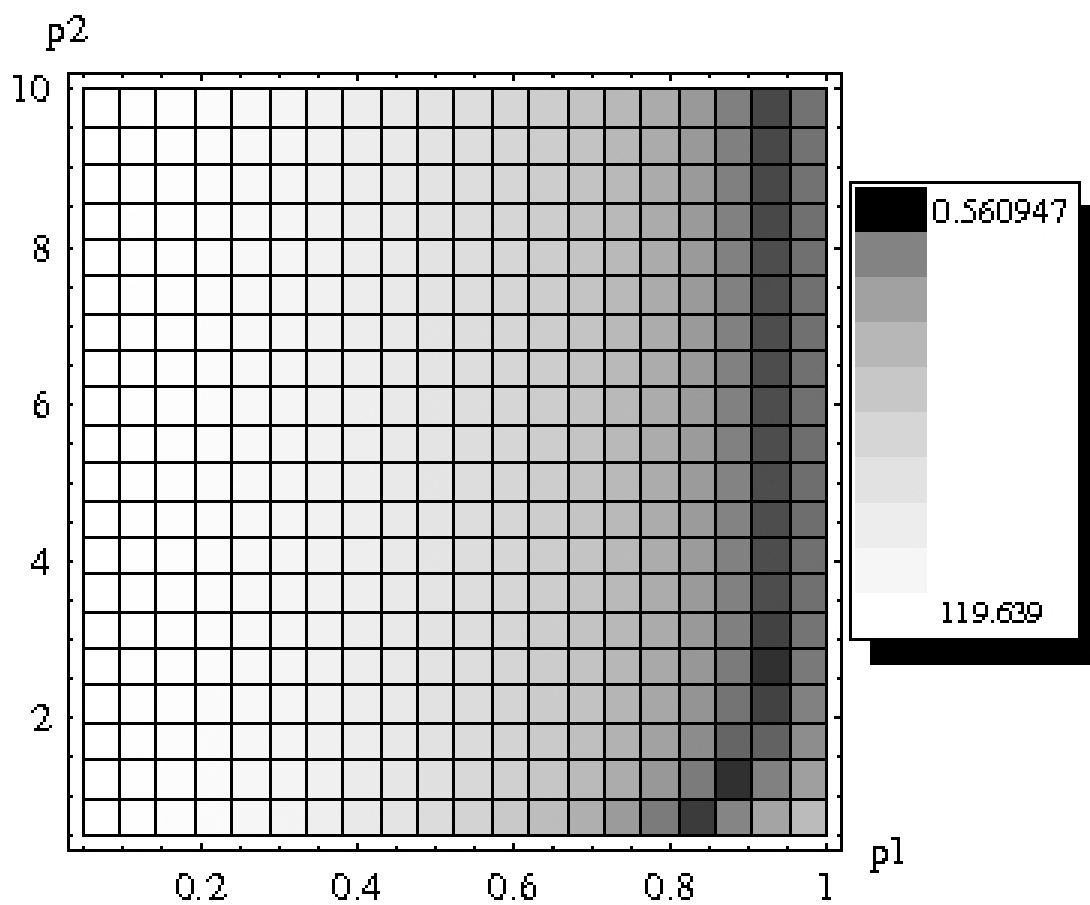
Error was defined as the difference between the DFT/MRCI excitation energy and the FCI excitation energy for the same electronic transition. Both DFT/MRCI and FCI calculations used the same basis set and/or effective core potential.

Appendix B lists the test atomic and molecular systems, the FCI calculations results, and density plots for the absolute error for each systems used to determine the universal damping parameters for the CPBE96 correlation functional. The test set consists of both double- and triple- ζ quality basis sets for atoms and diatomics. Ground state spin multiplicities ranges from singlet through quartet, and cover both closed- and open-shell systems, with open s - and p -shells. The original method proposed by Grimme and Waletzke was limited to singlet and triplet states. The spin-orbit extension to the original DFT/MRCI method developed by Kleinschmidt *et al* also contained this spin-multiplicity limitation. Figure 7 shows a density plot of this averaged data on the p_1/p_2 grid.

A clear band of minimum error exists in the density plot shown in Figure 7, ranging over p_1 values of roughly 0.8 to 0.96 and over p_2 values from 0 through 10. The band stabilizes and is essentially constant for values of $p_1 \approx 0.96$ and $p_2 > 2.0$. The global minimum averaged, normalized error occurred in the combined data at the values $p_1 = 0.85$, $p_2 = 0.5$. The stabilization of the minimum error band seems to indicate an asymptotic region where the damping parameters produce decent result across the range of test cases. Subsequent DFT/MRCI calculations were performed using the damping parameters $p_1 = 0.96$, $p_2 = 2.5$, located in the asymptotic region of the minimum absolute error band. These values were chosen because they produced smaller degeneracy errors in the validation systems than did the global minimum values, while producing roughly the same relative error with experiment.

In the following atomic and molecular systems used to demonstrate the capabilities of this implementation of the DFT/MRCI model, vertical excitation energies relative to the ground state are listed in wave numbers. These vertical transition energies were computed only at the bond length listed. In parentheses next to the

Figure 7: DFT/MRCI Averaged, Absolute Error with Respect to Full Configuration Interaction Results (mH)



excitation energy is the relative error in percent with experiment for that excitation. Positive relative errors reflect overestimation of the excitation energy, while negative relative errors underestimate the excitation energy. Also listed is the RMS error associated with calculated excitation energies over all states computed. For DFT/MRCI results computed using this model, errors in the degeneracy of states necessitated the computation of the average excitation energy, along with the standard deviation in the excitation energy. For states with degeneracies in both the ground and excited states (states with $L > 0$ for atoms or $\Lambda > 0$ for linear molecules), the respective errors in each state were combined statistically to yield the total error for the corresponding transition. For spin-orbit calculations, states are identified via their principle LS component.

3.4 Results and Analysis

A modified DFT/MRCI model, based upon Grimme and Waletzke’s method has been implemented and tested within the COLUMBUS program. Using the procedure described in the previous section, along with the two free damping parameters obtained, the DFT/MRCI model was applied to several atomic and molecular systems.

3.4.1 Carbon Monoxide. Carbon monoxide was chosen in order to compare the performance of this implementation of the DFT/MRCI model with that of Grimme and Waletzke. Spin-orbit effects were not considered in these calculations. A cc-pVTZ quality basis set was used, in order to duplicate the results obtained by Grimme and Waletzke [63] as closely as possible in this implementation. DFT/MRCI and TDDFT calculations were performed at a bond length 1.1261 Å, obtained from the National Institute of Standards and Technology (NIST) Computational Chemistry Comparison and Benchmark DataBase (CCCBDB) [1]. This bond length was generated from a DFT geometry optimization using a cc-pVTZ quality basis set and the hybrid B3LYP GGA correlation density functional.

Table 13 lists the DFT/MRCI, TDDFT, and experimental results for the carbon monoxide molecule. The first two σ orbitals, corresponding to the carbon and oxygen 1s orbitals, were frozen, as were the 44 highest energy virtual orbitals. The Kohn-Sham orbital energy difference between the Highest Occupied Molecular Orbital (HOMO) and the first frozen virtual orbital was roughly 38 eV. All reference configurations from a Complete Active Space (CAS) over the carbon and oxygen 2s and 2p orbitals was used in this calculation, corresponding to 10 active electrons in 8 orbitals. The CI expansion sizes resulting from this active space were 87,612 singlet CSFs and 145,620 triplet CSFs. Without freezing of the high energy virtual orbitals, the singlet CI expansion size was 3,706,115 CSFs while the triplet was 6,333,517 CSFs. This frozen virtual orbital approach resulted in a reduction in the CI expansion size by a factor of nearly 43.

Grimme and Waletzke reported a DFT/MRCI result of 66703.1 cm^{-1} for the ($n \rightarrow \pi^*$) excitation, corresponding to the $^1\Sigma^+$ to $^1\Pi$ transition [63]. They obtained 69284.1 cm^{-1} for the same excitation using TDDFT with the BHLYP functional. The DFT/MRCI transition energy obtained using this model was $72989 \pm 200 \text{ cm}^{-1}$, while the TDDFT excitation using the CPBE96 functional was 73723 cm^{-1} . Grimme’s and Waletzke’s DFT and TDDFT results could not be reproduced using the cc-pVTZ basis set and the BHLYP hybrid functional with the NWChem program.

Using the damping parameters found from the training set using calculations involving the first two rows on the periodic table, the carbon monoxide calculations performed here agree in principle with those results obtained by Grimme and Waletzke. Results listed in Table 13 show reasonable agreement between the DFT/MRCI results and the TDDFT results. The DFT/MRCI model outperforms TDDFT for nearly every state and in overall RMS error, slightly skewed by the large error in the $^3\Sigma^-$ state, which may be misidentified in the correspondence with measured results. For the excitation published, the allowed ($n \rightarrow \pi^*$), corresponding to the $^1\Sigma^+ \rightarrow ^1\Pi$

Table 13: Carbon Monoxide cc-pVTZ DFT/MRCI Results

State	DFT/MRCI Results (cm^{-1})	TDDFT Results (cm^{-1})	Measured Results [71] (cm^{-1})
$^1\Sigma^+$	0	0	0
$^3\Pi$	$49960 \pm 98 (+2.6)$	$47828 (-1.8)$	48686.7
$^3\Sigma^+$	$67570 (+5.2)$	$65059 (+1.3)$	55825.49
$^3\Delta$	$72669 \pm 30 (+18.9)$	$72298 (+18.3)$	61120
$^3\Sigma^-$	$76731 (+37.4)$	n/a	64230.2
$^1\Pi$	$73508 \pm 387 (+13.0)$	$73723 (+13.3)$	65075.7
RMS Error	23.6%	22.7%	

transition, this DFT/MRCI model yielded an electronic excitation energy within 13% of experiment, mirroring the performance of the TDDFT calculation. For the spin-forbidden transition, $^1\Sigma^+ \rightarrow ^3\Pi$, this DFT/MRCI model overestimated the excitation energy relative to experiment by roughly 3%, while the TDDFT calculation underestimated the same transition energy by nearly 2%.

Another source of error in the calculation could come from the correlation functional. While the more modern meta-GGA density functionals are possibly more accurate than local density approximation or generalized-gradient approximation density functionals in some cases because `NWChem` was unable to perform TDDFT calculations using them at present.

Apples to apples comparisons between Grimme and Waletzke’s published DFT/MRCI results for CO and those results obtained here are difficult for several reasons. First, while this implementation of the DFT/MRCI model follows that of Grimme and Waletzke, the basis of the CI algorithm differ between both approaches. The Grimme model is based on a selected CI algorithm allowing more flexibility in selection of the CSFs in the CI expansion. Second, their method incorporates a hybrid functional, with three more empirical parameters fit to a training set than the model presented here. The presence of the three additional fitted empirical parameters alone may be responsible for the 2.5% relative error with experiment they obtained, versus the 13%

found in this implementation of the model. Also, the basis sets were not exactly the same, which could account for some of the discrepancy, even though the basis set used in both calculations is triple- ζ quality.

3.4.2 Boron Fluoride. Table 14 lists DFT/MRCI, TDDFT, and measured results for the boron fluoride molecule at a bond length of 1.262 Å, obtained from diatomic spectroscopic measurements by Herzberg [67]. This DFT/MRCI calculation used references from an active space defined by a 8 electron, 6 orbital full valence CAS over the boron and fluorine 2s and 2p orbitals, with the 41 highest energy virtual orbitals frozen. The Kohn-Sham orbital energy difference between HOMO and the first frozen virtual orbital was roughly 38 eV. This expansion involved 206,346 CSFs. Without freezing the virtual orbitals, the BF expansion size was over 9 million CSFs. Here, the DFT/MRCI approach to freezing virtual orbitals resulted in a reduction in the CI expansion size of a factor of 46. Shape-consistent RECPs were used on both boron and fluorine, along with the corresponding spin-orbit operators, in order to obtain a relativistic treatment for both boron and fluorine. Both RECPs had the 1s electrons in the core.

The boron fluoride diatomic was investigated in the Kleinschmidt *et al* paper [76]. They used a shape-consistent relativistic effective core potential was used along with a spin-orbit operator. A cc-pVTZ quality basis set was used in their boron fluoride calculation.

Kleinschmidt *et al* reported a DFT/MRCI result of 27831 cm⁻¹ for the ¹Σ⁺ to ³Π excitation [76]. Using a two-step method to compute spin-orbit matrix elements, they obtained a spin-orbit splitting of the ³Π state of 22.3 cm⁻¹. They do not report a TDDFT excitation energy. They reported no other state excitation energies.

A MR-SOCISD calculation without DFT on the same active space produces a spin-orbit splitting in the ³Π state of 22.7 cm⁻¹. The DFT/MRCI calculated spin-

Table 14: BF cc-pVTZ DFT/MRCI Results

State	DFT/MRCI Results (cm^{-1})	TDDFT Results (cm^{-1})	Experiment Results [71] (cm^{-1})
$^1\Sigma^+$	0	0	0
$^3\Pi_2$	$28500 \pm 218 (-2.2)$		
$^3\Pi_1$	$30629 \pm 166 (+5.0)$	$22329 (+23.4)$	29144.3
$^3\Pi_0^+, ^3\Pi_0^-$	$32057 \pm 154 (+10.0)$		
$^1\Pi$	$55798 \pm 618 (+9.1)$	$54452 (+6.4)$	51157.45
$^3\Sigma^+$	$68893 (+4.7)$	$69983 (+14.7)$	61035.3
$^1\Sigma^+$	$71683 (+9.7)$	$90809 (+31.6)$	65353.9
$^3\Sigma^+$	$65526 (-2.3)$	$78023 (+16.4)$	67045
RMS Error	18.3%	45.5%	

orbit splitting between the $^3\Pi_2$ and $^3\Pi_1$ states was roughly 2129 cm^{-1} , while the calculated splitting between the $^3\Pi_1$ and $^3\Pi_{0+}$ and $^3\Pi_{0-}$ states was 1428 cm^{-1} , nearly two orders of magnitude greater than the MR-SOCISD calculation and the Kleinschmidt *et al* results. There are two possible reasons for this dramatic overestimation of the spin-orbit splitting in the DFT/MRCI results. The first reason is most likely due to degeneracy errors introduced by the DFT/MRCI method. The result of this state-broadening is to lift the degeneracies in eigenvalues, introducing a source of error into the calculation. For the boron fluoride example above, the degeneracy error introduced into the $^3\Pi$ states amounts to approximately 180 cm^{-1} on average, potentially swamping out the very small spin-orbit splitting. This degeneracy error suggests that this particular implementation of DFT/MRCI will not perform well when computing small spin-orbit splittings. Approximate degeneracy is maintained by the DFT/MRCI method in most cases, but the CI calculation can not restore eigenvalue degeneracies once they have been broken. The second possible reason for the large spin-orbit splitting error in the DFT/MRCI calculation is possibly due an overestimation of the expectation value of \hat{S}^2 on wave functions formed from Kohn-

Sham orbitals. This is a known feature of Kohn-Sham orbitals. The fact that the expectation value of \hat{S}^2 from restricted and unrestricted self-consistent field calculations can be too large by up to several percent [135]. This affects spin-orbit matrix elements over these spin-adapted CSFs, in that the contributions from \hat{S}_+ , \hat{S}_- , and \hat{S}_z can all be overestimated by a small amount.

For example, an unrestricted Kohn-Sham doublet wave function with an \hat{S}^2 expectation value of 0.7618 overestimates the expectation value by nearly 1.6%. This results in a value for \hat{S}_z of 0.5058, a result in error by nearly 1.2%. This 1% error in \hat{S}_z then gets directly factored into the $\hat{L}_z\hat{S}_z$ contribution to the spin-orbit matrix element. Similar errors propagate into the spin-orbit matrix elements from the \hat{S}_+ and \hat{S}_- contributions. Worst case scenario, these errors are all on the order of 1 to 2%, with no cancelation, yielding a spin-orbit matrix element in error by roughly 3 to 4%.

It is important to note that the calculation by Kleinschmidt *et al* computed the spin-orbit coupling in a two-step procedure, after the DFT/MRCI calculation on the singlet ground state and triplet excited state had already been performed separately. Scalar relativistic effects were not included in their calculation.

In this calculation, however, both scalar relativistic and spin-orbit effects were included in the DFT/MRCI calculation, the first such calculation performed. The relative error obtained in the calculation for the excitation from the $^1\Sigma^+ \rightarrow ^3\Pi$ state was nearly 4.3% when compared with experiment when the $^3\Pi$ state energies were averaged, and the DFT/MRCI calculation outperformed the TDDFT calculation when comparing the RMS errors over all six states computed. However, the spin-orbit splitting of the $^3\Pi$ state was grossly overestimated by this DFT/MRCI model. The error in the TDDFT calculation for the $^1\Sigma^+ \rightarrow ^3\Pi$ excitation was in error by roughly 23%.

3.4.3 Bromine Atom. The bromine atom was chosen to provide a test of the spin-orbit DFT/MRCI method using a fairly heavy atom. Spin-orbit coupling splits the doublet P ground state arising from a p^5 electron configuration into the ground

state ${}^2P_{\frac{3}{2}}$ and unoccupied ${}^2P_{\frac{1}{2}}$ state. Spin-orbit effects are largest in P states, and the splitting observed in bromine atomic spectroscopy is on the order of 3600 cm^{-1} . Non spin-orbit calculations will be unable to resolve this splitting, producing only a single energy for the 2P state.

The original DFT/MRCI method proposed by Grimme and Waletzke can not perform this calculation, as their original method did not incorporate two-component relativistic effects. The method extension published by Kleinschmidt *et al* introduces spin-orbit effects (but not scalar relativistic effects), and is multiplicity limited in the same way as the original Grimme and Waletzke procedure to coupling between singlet and triplet states only.

Since the bromine atom ground state is an open p^5 electronic configuration, with an odd number of electrons, the electronic states will transform according to the extra irreducible representations of the double group. This calculation represents the first application of a DFT/MRCI method to an odd-electron state, incorporating both one- and two-component relativistic effects.

A restricted active space was chosen for the bromine atomic calculation, consisting of the $4p^5$ and $(4p^45p^1)$ references, with the $3d$ electrons treated as a frozen core. The cc-pVDZ basis set provided by Dr. Russell Pitzer resulted in 30 basis functions, of which the highest 11 virtual orbitals were frozen. The CI expansion from this restricted active space consisted of 83,720 CSFs. Without freezing the virtual orbitals, the expansion size would have been 2,740,584 CSFs. Thus, the DFT/MRCI approach resulted in a CI expansion size of a factor of 33. A shape-consistent RECP and spin-orbit operator were used as well, with a valence space of $3d$, $4s$, and $4p$ electrons.

Table 15 lists the result of a modest DFT/MRCI calculation. The Kohn-Sham orbital energy difference between the HOMO and first frozen virtual orbital was roughly 34 eV.

Table 15: Bromine Atom cc-pVTZ DFT/MRCI Results

State	DFT/MRCI Results (cm^{-1})	Experiment Results [71] (cm^{-1})
$^2P_{\frac{3}{2}}$	0	0
$^2P_{\frac{1}{2}}$	$4092 \pm 339 (+11.0)$	3685.24

The degeneracy error in the ground state was roughly 323 cm^{-1} , while the degeneracy error in the first excited state was about 101 cm^{-1} , combining to produce an error of 339 cm^{-1} in the excitation energy and a relative error with experiment of roughly 11%.

A bug in the `CIUDG` code was uncovered during the bromine atomic spin-orbit CI calculation in C_1 symmetry. Each eigenvalue from the Spin-orbit Configuration Interaction (SOCI) calculation in the odd-electron case are doubly degenerate. So, for a $^2P_{\frac{1}{2}}$ state, the actual state is doubly degenerate, however, there should be only one eigenvalue associated with it. A $^2P_{\frac{3}{2}}$ state is four-fold degenerate, but the calculation should have two eigenvalues associated with the state. In C_1 symmetry, however, the degeneracy of the state was doubled, with all the roots associated with that doubling of the state degeneracy showing up as eigenvalues of the calculation. For example, the four-fold degenerate $^2P_{\frac{3}{2}}$ state, which should only have generated two degenerate eigenvalues, generated eight. This bug increases the number of roots required to completely characterize a state by J value, placing a limit on the number of states that can be calculated in C_1 . This is not a bug in the DFT/MRCI code, but in the odd-electron spin-orbit sections of the `CIUDG` code using C_1 symmetry.

Overall, despite the degeneracy error, this DFT/MRCI calculation on bromine demonstrates the capability of this DFT/MRCI code to provide reasonable results on an odd-electron atom with both scalar relativistic and spin-orbit effects. Unlike BF, the DFT/MRCI calculation was able to resolve the larger spin-orbit splitting in bromine, though there was still a large relative error due to state-broadening of

roughly 11% when compared with experiment. This calculation represents the first DFT/MRCI on a doublet state that incorporates scalar relativistic and spin-orbit effects via RECP, and demonstrates that this implementation is not multiplicity limited, as is the original Grimme and Waletzke algorithm as well as the two-step procedure by Kleinschmidt *et al.* Both of their approaches are limited to singlet and triplet states, and the Kleinschmidt approach can not incorporate scalar relativistic effects. A more recent publication by Kleinschmidt *et al* which incorporates their Spin Orbit Coupling Kit directly into the MOLCAS computational chemistry code with DFT/MRCI capability [77] performs the spin-orbit calculation in a one-step method, but is still unable to incorporate scalar relativistic effects, and still has the singlet and triplet spin multiplicity limitations.

3.4.4 Uranium +5 Ion. Based on the relative and RMS errors observed in the uranium ion calculations in chapter two, all uranium calculations used the 68 electron RECP. Double- ζ quality basis sets were used for all calculations. The basis set was originally developed by Dr. Scott Brozell. However, the basis set used 3s basis functions, making it unusable in NWChem calculations. Those basis functions had to be converted to 1s functions in order to obtain the V_c matrix elements and the correlation energy in order to use the DFT/MRCI method on the uranium systems. The basis set conversion procedure is described in Appendix C.

Using the converted 1s cc-pVDZ basis set in conjunction with the 68 electron shape-consistent RECP and spin-orbit operator, the uranium +5 ion calculation performed in chapter two was repeated using the DFT/MRCI model. The 5d electron shell was frozen in the calculation, and a full valence CAS of 1 electron in 12 orbitals was used, corresponding to all possible ways of putting one electron into the 5f and 6d orbitals. The five highest energy virtual orbitals were frozen in the calculation. This active space resulted in an expansion size of 39,836 CSFs. The size of the CI expansion without the frozen virtuals was 1,813,300 CSFs. The DFT/MRCI approach resulted in a reduction in the CI expansion size of a factor of 46. Table 16 lists the

results of the DFT/MRCI calculation, along with the corresponding MR-SOCISD calculation using the $3sd$ basis and the experimental values.

Table 16: U^{5+} DFT/MRCI Results, $(5f6d)^1$ Reference Space

Principle LS Component	DFT/MRCI 68e RECP $1s$ cc-pVDZ (cm^{-1})	MR-SOCISD 68e RECP $3sd$ cc-pVDZ (cm^{-1})	Experiment [17] (cm^{-1})
${}^2F_{\frac{5}{2}}^o$	0	0	0
${}^2F_{\frac{7}{2}}^o$	$6515 \pm 109(-14.4)$	$7578(-0.4)$	7608.6

The degeneracy error in the ${}^2F_{\frac{5}{2}}^o$ ground state amounted to nearly 71 cm^{-1} . Degeneracy error in the ${}^2F_{\frac{7}{2}}^o$ first excited state was roughly 82 cm^{-1} . Combining the ground-state and first excited state degeneracy errors resulted produced an error in the excitation energy of 109 cm^{-1} , yielding a relative error with experiment of 14%.

As in the case with the bromine calculation, the large spin-orbit splitting in the 2F ground state, measured to be 7608.6 cm^{-1} , was resolvable by this DFT/MRCI method. Again, the C_1 odd-electron bug in the CIUDG code doubled the expected degeneracies of the ground and first excited states, requiring the calculation of 28 eigenvalues to fully resolve them. The ${}^2F_{\frac{5}{2}}$ ground state required 12 eigenvalues to characterize, while the ${}^2F_{\frac{7}{2}}$ first excited state required 16 eigenvalues to fully characterize by J value. The hard limit on number of eigenvalues in the CIUDG code is 39, which would make exploring more excited states of the uranium +5 ion difficult.

Because of the limit of 39 eigenvalues in the CIUDG code, the next expected excited state, ${}^2D_{\frac{3}{2}}$, would push the number of required roots to 36. This is the limit on the number of states that can be examined with this version of the DFT/MRCI model. The reduced number of $3d$ basis functions and the effect of the degeneracy

errors are expected to result in a rather poor relative error for the ${}^2D_{\frac{3}{2}}$ state, based upon results obtained in chapter two.

3.4.5 Uranium +4 Ion. Using the converted 1s cc-pVDZ basis set in conjunction with the 68 electron shape-consistent RECP and spin-orbit operator, the ground and first two excited states of U^{+4} were calculated using the DFT/MRCI model. The 5d electron shell was frozen in the calculation, and a full valence CAS of 2 electron in 7 orbitals was used, corresponding to all possible ways of putting two electrons into the 5f orbital. The highest energy virtual orbital was frozen in the calculation. This active space resulted in an expansion size of 260,116 CSFs. Without the frozen virtuals, the CI expansion size would have been 5,397,041 CSFs. The DFT/MRCI approach resulted in a reduction in the CI expansion size of a factor of 21. Table 17 lists the results of the DFT/MRCI calculation, along with the corresponding MR-SOCISD calculation using the 3sd basis and the experimental values. The 3sd basis results with the 68 electron RECP for uranium +4 were obtained by Dr. Scott Brozell.

Table 17: U^{4+} DFT/MRCI and MR-SOCISD Results, $5f^2$ Reference Space

Principle <i>LS</i> Component	DFT/MRCI 68e RECP 1s cc-pVDZ (cm^{-1})	68e RECP 3sd cc-pVDZ (cm^{-1})	Measured [17] (cm^{-1})
${}^3H_{4g}$	0	0	0
${}^3F_{2g}$	$5078 \pm 111 (+22.1)$	$4210 (+1.2)$	4160.65
${}^3H_{5g}$	$5604 \pm 284 (-8.7)$	$6316 (+2.9)$	6136.88

It is apparent in the U^{4+} DFT/MRCI calculation that the degeneracy errors significantly impact the calculation of the excitation energies. The ground state degeneracy errors amounted to roughly 93 cm^{-1} , while the degeneracy error in the 3F_2 state was

61 cm^{-1} . These errors combine to produce an error in the ${}^3H_{4g} \rightarrow {}^3F_{2g}$ excitation energy of 111 cm^{-1} . The degeneracy error in the 3H_5 was 268 cm^{-1} . This combined with the degeneracy error in the ground state to produce an error in the ${}^3H_{4g} \rightarrow {}^3H_{5g}$ excitation energy of 284 cm^{-1} . The relative error with experiment of the first excited state was nearly 22%, while the relative error in the second excited state was a more reasonable 9%.

Identification of individual states was additionally complicated in the uranium +4 DFT/MRCI calculation by the degeneracy error in each state was difficulty in identification of the individual states. A large density of nearly degenerate states arise from the $5f^2$ electronic configuration in U^{4+} . With no symmetry in the DFT/MRCI wave function to guide state assignment, and state broadening causing overlap in excited states preventing state assignment through J -value degeneracy, identification of the uranium +4 ion states proved to be the most difficult of all cases studied.

Like the bromine atom, the uranium +4 has a measured excitation energy of the ${}^3H_4 \rightarrow {}^3F_2$ transition of 4160.65 cm^{-1} . When compared with the combined errors found in the uranium +5 ion excitation energy, the effect of the degeneracy errors in each individual state on the excitation energy is smaller, the larger the excitation energy is.

In boron fluoride, with a spin-orbit splitting on the order of 20 cm^{-1} , the degeneracy errors prevent an accurate measurement of this splitting. In the bromine atom and uranium +4 ions, with spin-orbit splittings on the order of 3600-4200 cm^{-1} relative errors in the DFT/MRCI excitation energies are roughly 11-22%. Based on the the results listed in Table 5 in chapter two for the MR-SOCISD calculations on the uranium +4 ion indicate that the dominant source of error in the relativistic DFT/MRCI calculations is due to the degeneracy errors, not the basis set or RECP. In the uranium +5 ion, with an excitation energy of roughly 7600 cm^{-1} , the combined relative error is roughly 14%.

3.4.6 *Uranyl Ion, UO_2^{2+} .* The final application of the DFT/MRCI model was to the uranyl ion, UO_2^{2+} . The DFT/MRCI calculation again used the converted $1s$ cc-pVDZ basis set on the uranium atom, in conjunction with the 68 electron RECP and spin-orbit operators. The $5d$ uranium electrons were frozen in the calculation, and a restricted active space consisting of $(\sigma_u^1 \delta_u \phi_u)^1$ was used. The five highest energy virtual orbitals were frozen in this calculation. The Kohn-Sham orbital energy difference between the HOMO and first frozen virtual orbital was 35 eV. The DFT/MRCI calculation consisted of 351,035 CSFs. Without the frozen virtuals, the expansion length was 22,545,659 CSFs. Here, the DFT/MRCI approach yielded a reduction in the CI expansion of a factor of 65.

Table 18 lists the results for the DFT/MRCI calculation, as well as the results of a MR-SOCISD calculation using the same RECP and a $3sd$ cc-pVDZ basis [9]. The MR-SOCISD calculation involved 5,322,501 CSFs, while the DFT/MRCI calculation involved 351,035 CSFs, a reduction in the CI expansion length of over an order of magnitude, while producing comparable results.

Table 18: UO_2^{2+} DFT/MRCI results

Principle <i>LS</i> Component	DFT/MRCI 68e RECP $1s$ cc-pVDZ	MR-SOCISD 68e RECP $3sd$ cc-pVDZ [9]
$^1\Sigma_{0g}^+$	0	0
$^3\Delta_{1g}$	18235±354	19799
$^3\Delta_{2g}$	20393±192	19912
$^3\Delta_{3g}$	21615±404	21138
$^3\Phi_{2g}$	22838±73	22432
$^3\Phi_{3g}$	26123±42	25064
$^3\Phi_{4g}$	26825±52	26486

Table 19 lists a series of experimentally measured uranyl fluorescent series [111] as well as the results of the DFT/MRCI and MR-SOCISD calculations.

Table 19: UO_2^{2+} Calculated and Measured Fluorescent Series

Molecule	Fluorescent Series (cm^{-1})
DFT/MRCI	18235±354
MR-SOCISD 68e RECP [9]	19779
$\text{Rb}_2\text{UO}_2\text{Cl}_4 \cdot 2\text{H}_2\text{O}$	19961
$\text{K}_2\text{UO}_2\text{Cl}_4 \cdot 2\text{H}_2\text{O}$	19970
$\text{Cs}_2\text{UO}_2\text{Cl}_4$	20096
$\text{Rb}_2\text{UO}_2(\text{SO}_4)_2$	20390
$\text{UO}_2(\text{NO}_3)_2 \cdot 6\text{H}_2\text{O}$	20578
$\text{Cs}_2\text{UO}_2(\text{SO}_4)_2 \cdot 3\text{H}_2\text{O}$	20594
$\text{UO}_2(\text{NO}_3)_2 \cdot 3\text{H}_2\text{O}$	20779
$\text{Rb}_2\text{UO}_2(\text{NO}_3)_4$	20808
$\text{K}_2\text{UO}_2(\text{NO}_3)_4$	20818
$\text{K}_2\text{UO}_2(\text{CO}_3)_2$	20943
$\text{PbUO}_2(\text{CH}_3\text{COO})_4$	20958
$\text{CsUO}_2(\text{CH}_3\text{COO})_3$	20992
$\text{RbUO}_2(\text{CH}_3\text{COO})_3$	21049
$\text{NH}_4\text{UO}_2(\text{CH}_3\text{COO})_3$	21056
$\text{CsUO}_2(\text{NO}_3)_3$	21090
$\text{NH}_4\text{UO}_2(\text{NO}_3)_4$	21098
$\text{NaUO}_2(\text{CH}_3\text{COO})_3$	21135
$\text{KUO}_2(\text{NO}_3)_3$	21183
$\text{RbUO}_2(\text{NO}_3)_3$	21199

While the uranyl ion is an alluring benchmark for relativistic calculations, due to its importance in uranium chemistry, the lack of gas-phase experimental measurements of its electronic spectra make meaningful accuracy assessments of theoretical methods applied to uranyl difficult. Without such gas-phase data to compare with, only comparisons versus crystallographic measurements are possible. In such bulk measurements, uncertainties in the local uranyl environment, the effect of crystal field splittings, and other perturbations to the spectra make most quantitative comparisons problematic.

However, based upon the results listed in the last chapter in Table 18, it appears that this DFT/MRCI model does at least as good a job as a MR-SOCISD calculation, and does it at a substantial computational savings when compared to the MR-SOCISD calculation. The DFT/MRCI CI expansion was roughly 315,000 CSFs, versus the nearly 5,000,000 CSF expansion in the MR-SOCISD calculation. It is possible that the reduction in $3d$ function flexibility resulting from the $1s$ basis conversion process is responsible for more error than degeneracy errors here, which are on the range from 42 cm^{-1} for the ${}^3\Phi_{3g}$ state to 404 cm^{-1} in the ${}^3\Delta_{3g}$ state. Despite this, the DFT/MRCI results fall nicely in range of measured uranyl spectra listed in Table 19. One possible explanation is that some cancellation of error occurred in the linear molecular calculation that was not present in the spherically symmetric ionic calculations. The calculated excitation energies for the fluorescent spectra fall in the low end of the measured values. A likely reason for the measured values being higher is because of solvation or crystal field effects that are not present in the theoretical gas phase calculations.

IV. Conclusions

This chapter contains an analysis of the results of the various aspects of this research project, as well conclusions based upon that analysis. It is divided into several sections, one section for each major thrust of this project.

The first section analyzes and draws conclusions from the series of MR-SOCISD calculations on the uranium +5 and uranium +4 ions described in chapter two. Conclusions based on the relative errors involved in the various core-valence cut-off choices using the shape-consistent RECPs are drawn. The second section examines the overall performance of this implementation of the DFT/MRCI model, and based on the analysis in the previous chapter, examines the observed successes in the calculations on carbon monoxide, boron fluoride, the bromine atom, followed by a discussion of performance of the DFT/MRCI model on uranium ions and molecules. Next the successes and failures in achieving the research objectives laid out in chapter one will be covered, followed finally by suggestions for future work in the area of hybrid DFT and wave function based computational chemistry for application to atomic and molecular excited states.

4.1 Uranium Shape-Consistent RECP Accuracy Assessment

Two factors impacting the relative and overall errors in the calculation of the electronic excitation energies of the U^{5+} and U^{4+} cations are the sizes of the relativistic effective potential core and the reference space.

The effect of the core size in the uranium cation calculations shows that the 68 electron core does well in both the $5f^n$ and $(5f6d)^n$ reference spaces when compared with experiment. States that arise from electron configurations not included in the reference space were poorly modeled in all calculations and skew the overall RMS error accordingly. These states are the 2D and 2S states in the U^{5+} calculations, which arise from $6d^1$ and $7s^1$ electron configurations, respectively. Similarly, the odd states in the U^{4+} calculations, arising from $5f^16d^1$ electron configurations are not modeled well using only the $5f^2$ references.

The larger error in those states can be explained by the fact excitations from electron configurations specifically in the reference space represent excitation levels higher than single and double excitations. For example, states produced by $6d^1$ configurations are computed at the single and double excitation level when using a smaller $5f^1$ reference space, however, these same states contain selected contributions of higher order (triple and quadruple) excitations from the larger $(5f6d)^1$ active space. Thus, the 2D states are computed at excitation levels higher than singles and doubles when computed using the larger active space.

With respect to the choice of the core size, in both uranium cation calculations, the 68 electron core produced the lowest relative and RMS errors, on the order of 1-2% for those states included in the reference space in the U^{5+} calculations. The 78 electron core produces large relative and RMS errors in the U^{5+} calculation. The 60 electron core produces better results when compared with the 78 electron core, however, the accuracies produced by the 60 electron core do not warrant the larger computational effort in terms of CI expansion size involved in its use.

For the +4 cation, however, different results were obtained. When examining only the even states arising from the $5f^2$ configurations, both the 68 and 78 electron core calculations produced roughly equivalent results, both of which outperform the 60 electron core. Inclusion of the odd states arising from $5f^16d^1$ electronic configurations skew the overall errors in favor of the 68 electron core.

One possible explanation for the relative success of the 68 electron core RECP in the U^{5+} calculation may lie in the nature of the core and valence electron shell treatments. Recall the various valence electrons included in each RECP listed in table 1. Incorporation of an electron shell in the core allows for a relativistic treatment (relativistic contraction and expansion, as well as spin-orbit splitting) of those electrons, while relativity is treated indirectly, via interaction with the core potential, in the valence electrons. Electrons in the core p -shells are known to exhibit the largest spin-orbit splitting, so inclusion of the uranium $5p$ shell in the core in order for an

accurate relativistic description seems warranted, as is done in the 68 and 78 electron core potentials. Removal of the uranium $5d$ shell from the valence space, as is done in the 78 electron shape-consistent core potential, does not allow for relaxation of the $6d$ electron shell. The 68 electron core RECP strikes one possible balance between relativity and polarization. The near degeneracy of the $5f$ and $6d$ shells in many uranium atomic species seems to require an accurate treatment of the $6d$ electronic excitations, which can be facilitated by freeing the $5d$ shell from the core and into the valence electron space.

The similar performance of the 78 and 68 electron cores in the U^{4+} calculations seems to counter the argument presented above. One possible source of this result is the fact that in this core potential treatment, there are no core-valence interactions possible, so the shape-consistent core potential method does not include any way for the core region to polarize. Thus, while the 68 electron core allows polarization of the $5d$ electrons, with only indirect relativistic effects via interaction with the core, the 78 electron core allows a relativistic treatment of the $5d$ electrons, but no polarization to occur. One possible explanation of the observed results is that these treatments are roughly the same magnitude, and that a higher order description of the core-valence interaction may be necessary to resolve the near degeneracy in the 68 and 78 electron core results. The fact remains, however, that the 78 electron core calculations represent a lower computational cost in terms of CI expansion length, and give accurate results, in the U^{4+} calculations. The presence of a trend may be established by examining the U^{3+} and U^{2+} cations.

Overall, applying Christiansen *et al* shape-consistent relativistic effective core potentials in MR-SOCISD calculations of the ground and excited states of U^{5+} and U^{4+} ions shows that the 68 electron RECP, along with a cc-pVDZ basis set, yields relative errors of 1 to 3% with experiment for each calculated state, part of which may be due to a fortuitous cancellation of error based on analysis of results obtained using double- ζ quality basis sets. The lowest relative errors in excitation energies were achieved when the reference space included all the electron configurations spawning

the states of interest. Inclusion of the spin-orbit interaction is crucial in these calculations, as the lowest energy electronic transitions in U^{5+} and U^{4+} arise from $5f \rightarrow 5f$ transitions.

4.2 *DFT/MRCI Model*

The first experiences with applications of this implementation of the DFT/MRCI model was during the determination of the damping parameters p_1 and p_2 . The training systems, listed in Appendix B, span the first two rows of the periodic table, with emphasis on atomic systems with open $2p$ shells using double- ζ quality basis sets.

It is interesting to note the absolute errors for each individual test case listed in Appendix B vary. In some cases, the error between the DFT/MRCI and FCI results are very small, on the order of micro-Hartrees. Even the largest errors obtained are not greater than 10s of milliHartrees. It is impressive that the hybrid DFT/CI method implemented here can achieve such accuracies when compared with FCI calculations, which are known to be the exact non-relativistic solution for that particular basis set. All training systems listed in Appendix B were treated non-relativistically.

When examining the density plots of in Appendix B, some are devoid of features. The beryllium cc-pVDZ calculation is one such example. The triple- ζ calculation reveals more detail in the p_1/p_2 space, where the double- ζ basis set calculation shows no features at all. Helium is another such example where the larger basis set reveals detail in the damping parameter space that is absent in the calculation with the smaller basis set. In all cases where there were double- and triple- ζ quality basis set calculations on the same system, the larger basis set revealed as much and usually more detail in the damping parameter space. Unfortunately, for the larger atoms, beyond carbon, FCI calculations using larger basis sets simply were not feasible in this research effort.

Examining the density plots in Appendix B, several of the calculations reveal interesting structure. Some density plots revealed contours similar in shape to those

found in the analytical investigation of the two level system investigated in chapter three. Double- ζ H_2 , the helium atom at both basis set sizes, oxygen and fluorine all exhibit this simple structure. Most of the other density plots showed band-like structure in the damping parameter space. In most cases where this minimum error banding occurred, the bands tended to stabilize at higher values of p_2 , as if exhibiting asymptotic behavior. It is difficult to draw overarching significance to this banded structure in the damping parameter space, as little is known about the theoretical basis of the DFT/MRCI method. One of the most interesting band structures is seen in the case of the beryllium dimer. There does appear to be some correlation between the banding structure in the density plots and the single reference nature of the test system involved. Both the beryllium atom (cc-pVTZ) and beryllium dimer have the most multi-determinant character, and both exhibit interesting banding structure. Carbon, nitrogen, and boron also have larger multi-reference character than the other systems, and they exhibit banding in the density plots. It is possible, at least in the plots that show features (cc-pVDZ helium and beryllium are relatively featureless) in the damping parameter space, that all of the plots show banding, however, the location and direction of the bands varies from system to system. In some systems, such as lithium, the band runs up the right hand side of the density plot, and is independent of p_2 . In other cases, such as neon, the band runs up the left hand side of the density plot, apparently independent of p_2 . Perhaps in these cases, which are mostly single-determinant systems, forming a CI expansion based upon those Kohn-Sham orbitals results in a good initial guess, which is then only corrected through small contributions from degenerate CSFs. In the cases of oxygen and fluorine, it appears that the DFT/MRCI approach using a GGA correlation functional may not be accurate enough to show the banding structure, based on the similarities with the absolute error density plots of the two level system investigated in detail in Appendix B. A rigorous theoretical basis for the hybrid DFT/MRCI method should be able to account for this banding structure. At the moment, however, only loose trends can be drawn from the data in Appendix B. Whether these trends can be attributed to the

accuracy of the correlation functional, the basis set quality, or, the multi-determinant nature of the system studied is difficult to determine at this stage.

Three systems were chosen to demonstrate the capabilities of this implementation of this DFT/MRCI model: Carbon monoxide, boron fluoride, and the bromine atom. Carbon monoxide and boron fluoride were chosen to compare the accuracy of this model with published results of Grimme and Waletzke for carbon monoxide, and Kleinschmidt *et al* for boron fluoride. The carbon monoxide calculation did not involve relativistic effects. The DFT/MRCI method resulted in a reduction in the CI expansion size in both CO and BF of over a factor of 40.

Using the damping parameters found from the training set using calculations involving the first two rows on the periodic table, the carbon monoxide calculations performed here seem to agree in principle with those results obtained by Grimme and Waletzke. Results listed in Table 13 show reasonable agreement between the DFT/MRCI results and the TDDFT results. The DFT/MRCI model outperforms TDDFT for nearly every state and in overall RMS error, slightly skewed by the large error in the $^3\Sigma^-$ state, which may be misidentified in the correspondence with experiment. For the excitation published, the allowed ($n \rightarrow \pi^*$), corresponding to the $^1\Sigma^+ \rightarrow ^1\Pi$ transition, this DFT/MRCI model yielded an electronic excitation energy within 12% of experiment, mirroring the performance of the TDDFT calculation. For the spin-forbidden transition, $^1\Sigma^+ \rightarrow ^3\Pi$, this DFT/MRCI model overestimated the excitation energy relative to experiment by roughly 1%, while the TDDFT calculation underestimated the same transition energy by nearly 2%.

Another source of error in the calculation could be the correlation functional used. Modern meta-GGA density functionals are possibly more accurate than local density approximation or generalized-gradient approximation density functionals in some cases.

Apples to apples comparisons between Grimme and Waletzke’s published DFT/MRCI results for CO and those results obtained here are difficult for several reasons. First,

while this implementation of the DFT/MRCI model follows that of Grimme and Waletzke, the basis of the CI algorithm differ between both approaches. The Grimme model is based on a selected CI algorithm, allowing more flexibility in selection of the CSFs in the CI expansion. Second, their method incorporates a hybrid functional, with three more empirical parameters fit to a training set than the model presented here. The presence of the three additional fitted empirical parameters alone may be responsible for the 2.5% relative error with experiment they obtained, versus the 12% found in this implementation of the model. Also, the basis sets were not exactly the same, which could account for some of the discrepancy, even though the basis set used in both calculations are of triple- ζ quality.

The DFT/MRCI calculation on boron fluoride performed here was an attempt to duplicate the results obtained by Kleinschmidt *et al* using the relativistic capabilities of the COLUMBUS code in conjunction with the DFT/MRCI model. It is important to note that the calculation by Kleinschmidt *et al* involved only computing the spin-orbit coupling in a two-step procedure, after the DFT/MRCI calculation on the singlet ground state and triplet excited state had already been performed. Scalar relativistic effects were not included in their calculation.

In this calculation, however, both scalar relativistic and spin-orbit effects were included in the DFT/MRCI calculation, the first such calculation performed. While the relative error obtained in the calculation for the excitation from the $^1\Sigma^+ \rightarrow ^3\Pi$ state was nearly 22% when compared with experiment, and the DFT/MRCI calculation outperformed the TDDFT calculation when comparing the RMS errors over all six states computed. However, the spin-orbit splitting of the $^3\Pi$ state was grossly overestimated by this DFT/MRCI model. There are two possible contributing factors to this large spin-orbit splitting error in the BF calculation. First, state broadening is introduced by the DFT/MRCI method. The result of this state-broadening is to lift the degeneracies in eigenvalues, introducing a source of error into the calculation. For the boron fluoride example above, the state broadening error introduced into the $^3\Pi$ state is roughly 115 cm^{-1} , potentially swamping out the very small spin-orbit splitting.

This degeneracy error suggests that this particular implementation of DFT/MRCI will not perform well when computing small spin-orbit splittings. Kleinschmidt *et al* reported a spin-orbit splitting of about 22 cm⁻¹, a result verified through a small MR-SOCISD calculation.

The degeneracy errors arise from two sources. The first source is the broken degeneracy in the initial Kohn-Sham orbitals, problematic for DFT calculations and atomic calculations with *d* orbitals and above. This is due to the fact that the approximate density functionals are not yet capable of reproducing the degeneracy in spherically symmetric states with angular momentum $L = 2$ or higher. The second degeneracy error source is the DFT/MRCI method, which was shown in chapter three to be capable of breaking degeneracies between eigenvalues. Approximate degeneracy is maintained by the DFT/MRCI method in most cases, but the CI calculation can not restore proper eigenvalue degeneracies if they are broken in the initial guess. The second possible reason for the large spin-orbit splitting error in the DFT/MRCI calculation is possibly due an overestimation of the expectation value of \hat{S}^2 on wave functions formed from Kohn-Sham orbitals. It is a known feature of Kohn-Sham orbitals [135] that the expectation value of \hat{S}^2 from restricted and unrestricted self-consistent field calculations are too large by up to several percent. This affects spin-orbit matrix elements over these spin-adapted CSFs, in that the contributions from \hat{S}_+ , \hat{S}_- , and \hat{S}_z can be overestimated by a small amount. Worse case scenario, these errors are all on the order of 1 to 2% with no cancellation, yielding a spin-orbit matrix element in error by roughly 6 to 7%.

In terms of correspondence with the measured experimental excitation energy, the DFT/MRCI calculation was able to predict the ³Π excitation energy to less than 22%, with a very small CI expansion of less than 20,000 CSFs, however degeneracy errors made an accurate spin-orbit splitting calculation impossible for this system. The corresponding relative error in the TDDFT calculation was 23.4%.

The bromine atom is an odd-electron system, with a 2P ground state. It is a fairly heavy atom with a spin-orbit splitting of the ground state which is two orders of magnitude higher than in BF. Indeed, experiment measures a spin-orbit splitting in the 2P state of about 3600 wave numbers.

A bug in the odd-electron, spin-orbit behavior of the CIUDG code was uncovered which resulted in a doubling of the degeneracies of the calculated eigenvalues in C_1 symmetry. This bug increases the number of roots required to completely characterize a state by J value, placing a limit on the number of states that can be calculated in C_1 . This is not a bug in the DFT/MRCI code, but in the odd-electron spin-orbit sections of the code in C_1 symmetry.

The degeneracy error in the Br ground state was roughly 323 cm^{-1} , while the degeneracy error in the first excited state was about 102 cm^{-1} , yielding a relative error with experiment of 11%. Overall, despite the degeneracy error, this DFT/MRCI calculation on bromine demonstrates the capability of this DFT/MRCI code to provide reasonable results on an odd-electron atom with both scalar relativistic and spin-orbit effects. Unlike BF, the DFT/MRCI calculation was able to resolve the larger spin-orbit splitting in bromine, though there was still a large relative error due to state-broadening of roughly 11% when compared with experiment. This calculation represents the first DFT/MRCI on a doublet state that incorporates scalar relativistic and spin-orbit effects via RECP, and demonstrates that this implementation is not multiplicity limited, as are the original Grimme and Waletzke codes, which are unable to incorporate scalar relativistic effects, and the two-step procedure by Kleinschmidt *et al.* Both the Grimme and Waletzke and Kleinschmidt *et al.* DFT/MRCI model implementations are limited to singlet and triplet states. A more recent publication by Kleinschmidt *et al.* which incorporates their Spin Orbit Coupling Kit directly into the MOLCAS computational chemistry code with DFT/MRCI capability [77] performs the spin-orbit calculation in a one-step method, but is still unable to incorporate scalar relativistic effects, and it still has the singlet and triplet spin multiplicity limitations.

The DFT/MRCI approach here in the bromine calculation yielded a reduction in the CI expansion size of a factor of 33.

Based upon the analysis in Appendix C, the basis set conversion procedure used to create a useful $1s$ function basis set for use in DFT/MRCI calculations resulted in an adequate cc-pVDZ basis set, but reduced in size from the original $3sd$ basis. Most of the basis set reduction occurred in the elimination of $3d$ functions, reducing the flexibility of the basis set somewhat. Calculations using both the $1s$ and $3sd$ basis set showed little impact in the $f \rightarrow f$ transitions characteristic in the electronic spectra of the uranium +5 and +4 ions. In the +5 ion, both basis sets produced relative errors of less than 1% in ${}^2F_{\frac{5}{2}} \rightarrow {}^2F_{\frac{7}{2}}$ transition. The effect of the conversion process became apparent in the D and S states. The effect was particularly pronounced in the S state, with a relative error of nearly 37% in the converted $1s$ basis set versus 10% in the original $3sd$ basis set. Based on this analysis, it is assumed that the states arising from $5f$ configurations are relatively unaffected by the conversion process.

As in the case with the bromine calculation, the large spin-orbit splitting in the 2F ground state, measured experimentally to be 7608.6 cm^{-1} , was resolvable by this DFT/MRCI method. Again, the C_1 odd-electron bug in the CIUDG code doubled the expected degeneracies of the ground and first excited states, required calculation of 28 eigenvalues to fully resolve them. The ${}^2F_{\frac{5}{2}}$ ground state required 12 eigenvalues to characterize, while the ${}^2F_{\frac{7}{2}}$ first excited state required 16 eigenvalues to fully characterize.

Degeneracy errors in the ${}^2F_{\frac{5}{2}}$ ground state amounted to nearly 71 cm^{-1} . Degeneracy error contributed roughly 82 cm^{-1} to the ${}^2F_{\frac{7}{2}}$ excited state. Combining the ground state and first excited state error statistically, the DFT/MRCI model underestimates the excitation energy calculation climbs by about 14%. Cancellation of errors could account for the reduced relative error in the maximum excitation energy listed in Table 16. The next expected excited state, the ${}^2D_{\frac{3}{2}}$ would push the number of required eigenvalues to 36. This is the limit on the number of states that can be

examined with this version of the DFT/MRCI model, because 39 eigenvalues is the hard coded limit in CIUDG.

The U^{5+} active space resulted in an expansion size of 39,836 CSFs. The size of the CI expansion without the frozen virtuals was 1,813,300 CSFs. The DFT/MRCI approach resulted in a reduction in the CI expansion size of a factor of 46.

It is apparent in the U^{4+} DFT/MRCI calculation that the state broadening introduces a significant error into the calculation of the excitation energies. The combined 3H_4 ground state and 3F_2 degeneracy errors yield an overestimation of the excitation energy by a slightly more than 22%. The second excited state transition energy is underestimated by a 9%. This result was achieved with a CI expansion size of 260,116 CSFs. Without the frozen virtuals, the CI expansion size would have been 5,397,041 CSFs. In the DFT/MRCI approach resulted in a reduction in the CI expansion size of a factor of 21.

An additional complication in the uranium +4 DFT/MRCI calculation was that the degeneracy error in each state complicated identification of the individual states. A large density of nearly degenerate states arise from the $5f^2$ electronic configuration in U^{4+} . The main difficulties in state identification were due to lack of symmetry in the DFT/MRCI wave function and state broadening overlap in excited states. Both factors complicated state assignment through J degeneracy.

The uranium +4 has a measured excitation energy of the ${}^3H_4 \rightarrow {}^3F_2$ transition of 4160.65 cm^{-1} . When compared with the combined errors found in the uranium +5 ion excitation energy, the effect of the degeneracy errors in each individual state on the excitation energy is smaller, the larger the excitation energy is. This trend, based on the boron fluoride, bromine atom, uranium +4, and uranium +5 ion DFT/MRCI results is supported by the calculations.

In boron fluoride, with a small spin-orbit splitting on the order of 20 cm^{-1} , degeneracy errors prevent an accurate measurement of this splitting. In the bromine atom and uranium +4 ions, with spin-orbit splittings on the order of $3600\text{-}4200 \text{ cm}^{-1}$,

relative errors in the DFT/MRCI excitation energies are roughly 11-22%. In the uranium +5 ion, with an excitation energy of roughly 7600 cm^{-1} , the combined relative error is roughly 14%. Based on the the results in chapter two for the MR-SOCISD calculations on the uranium +4 and +5 ions, the dominant source of error in the relativistic DFT/MRCI calculations appears to be due to the degeneracy error.

The final application of this DFT/MRCI model to the uranyl ion shows that this method holds promise, while the uranium ionic calculations showed large relative errors with experiment in the first excitation energy.

Based upon the results listed in the last chapter in Table 18, it appears the this DFT/MRCI model does at least as good a job as a MR-SOCISD calculation, and does it at a substantial computational savings when compared to the MR-SOCISD calculation. The DFT/MRCI CI expansion was roughly 315,000 CSFs, versus the over 22,000,000 CSFs resulting from no frozen virtual orbitals. Here, the DFT/MRCI method yielded a reduction in the CI expansion by a factor of 65. It is possible that the reduction in $3d$ function flexibility resulting from the $1s$ basis conversion process is responsible for more error than degeneracy errors here, which are on the range from 42 cm^{-1} for the ${}^3\Phi_{3g}$ state to 404 cm^{-1} in the ${}^3\Delta_{3g}$ state. Despite this, the DFT/MRCI results fall nicely in the range of measured uranyl spectra listed in Table 19. One possible explanation is that some cancellation of error occurred in the linear molecular calculation that was not present in the spherically symmetric ionic and atomic calculations. The calculated values for the fluorescent spectra fall in the low end of the measured values. A likely reason for the measured values being higher is because of solvation or crystal field perturbations that are not present in the theoretical gas phase calculations.

4.3 Research Objective Successes and Failures

The focus of this work was to develop an accurate and scalable method for computing the electronic spectra of heavy element compounds which incorporates

one- and two-component relativistic effects based upon the hybrid DFT-CI method developed by Grimme and Waletzke [62] [63].

By leveraging the relativistic capabilities in the COLUMBUS relativistic quantum chemistry code, these objectives were successfully completed, as demonstrated by the boron fluoride, bromine atom, uranium +4 and +5 ions, as well as the uranyl ion. Scalar relativistic effects were incorporated through the use of shape consistent RECPs, while spin-orbit effects were incorporated in a one-step fashion through the use of spin-orbit operators.

This DFT/MRCI model achieved modest accuracy when computing electronic excitation energies, and consistently outperformed TDDFT calculations of the same excitation energy. Errors in eigenvalue degeneracies, also referred to as state broadening, governed the overall accuracy achievable in the electronic excitation energy in states split by a spin-orbit Hamiltonian. For boron fluoride, with a spin-orbit splitting in the $^3\Pi$ state of roughly 20 cm^{-1} , as determined by MR-SOCISD calculations and obtained in reference [76], these state broadening errors prevented accurate measurement of the spin-orbit splitting. This model was unable to resolve the splitting, grossly overestimating the spin-orbit splitting by several orders of magnitude. It should be noted that the measured spectroscopic values do not report spin-orbit splitting in the $^3\Pi$ state.

In the case of the bromine atom, with spin-orbit splittings of the 2P ground state of roughly 3600 cm^{-1} , this DFT/MRCI model was able to compute the $^2P_{3/2} \rightarrow ^2P_{3/2}$ excitation energy to a relative error with experiment of around 11%. The bromine atom was a significant calculation, in that not only did it demonstrate the DFT/MRCI model could achieve modest accuracy in the case of a fairly heavy atom, it was also the first non-singlet, non-triplet DFT/MRCI calculation performed. This calculation demonstrated that this implementation of the DFT/MRCI model was successful in removing the spin multiplicity limitations inherent in the original Grimme and Waletzke model.

The DFT/MRCI calculation on the uranium +4 ion, with a measured excitation energy for the ${}^3H_4 \rightarrow {}^3F_2$ transition of roughly 4100 cm^{-1} , yielded modest results on the roughly the same order as those obtained in the bromine calculation. Relative error between the DFT/MRCI and measured excitation energy was on the order of 22% in this case.

The DFT/MRCI results on the ${}^2F_{\frac{5}{2}} \rightarrow {}^2F_{\frac{7}{2}}$ transition again yielded roughly the same relative error as was observed in the bromine and uranium +4 calculations. A relative error with experiment of around 14% was observed in the uranium +5 calculation, where the measured excitation energy was nearly 7600 cm^{-1} . The reduction in relative error here might be a result of the larger spin-orbit splitting of the ground state, but is consistent with the boron fluoride, bromine, and uranium +4 results.

The final application of this DFT/MRCI model to the uranyl ion showed the most promising results in terms of relative error with respect to measured photoluminescence spectra. While no direct comparison with measured values is possible for this calculation, the results obtained for the ${}^1\Sigma_{0g^+} \rightarrow {}^3\Delta_{1g}$ transition compare favorably with larger MR-SOCISD calculations and measured uranyl spectra in crystalline compounds. Table 19 in chapter three show these results. Reductions in CI expansion size of factors of 25-65 were achieved using the DFT/MRCI approach of freezing high energy virtual orbitals. This reduction of effort occurred while still beating the accuracy of TDDFT in RMS and relative error in almost every case.

This implementation of the DFT/MRCI model, based upon a correlation-only density functional, removed the spin multiplicity limitation inherent in the original Grimme and Waletzke DFT/MRCI method. Examining the DFT/MRCI calculations on doublet and quartets in Appendix B, errors on the order of 6-70 microHartrees with respect to the FCI excitation energies were obtained in lithium, boron, and nitrogen, which have 2S , 2P , and 4S ground states respectively. Calculations on the 2P and 2F states of bromine and uranium +5, respectively demonstrate successful relativistic DFT/MRCI calculations on a doublet atomic system.

Accuracy of the DFT/MRCI method was another research goal in this project. Calculations used to determine the damping parameters, presented in Appendix B, achieved error ranging from 6-70 microHartrees with respect to FCI excitation energies as well as consistently outperforming TDDFT results over a wide range of states. It is apparent that this DFT/MRCI model, in the non-relativistic case, can achieve accuracies rivaling and exceeding those obtainable using TDDFT and MR-CISD calculations in most cases examined. Using a correlation only density functional to compute the dynamic correlation energy was successful in producing accurate, meaningful results, and was directly responsible for lifting the multiplicity limitation. However, some error in the method will always remain as long as 100% exact HF exchange is used, even if the exact correlation functional was found. This is because HF exchange is exactly only with HF orbitals, not when used with Kohn-Sham molecular orbitals. Additionally, the relative errors produced in the relativistic calculations, due mostly to degeneracy errors inherent to this method, are inadequate for precision spectroscopic predictions.

In terms of efficiency, in the case of MR-CISD comparisons, the DFT/MRCI achieved better results using smaller CI expansions by freezing select virtual orbitals. Experience demonstrated that the DFT/MRCI calculations produced good results by freezing virtual orbitals with Kohn-Sham orbital energy differences with the HOMO on the order of 40 eV. Substantial reductions in CI expansion size were achieved in all cases.

With respect to scalar relativistic and spin-orbit effects, accuracy of this DFT/MRCI model was clouded by errors in eigenvalue degeneracies, on the order of 10s to 100s of wave numbers. The best results were obtained in U^{+5} , with a relative error in the excitation energy of around 9%. Uranyl ion results also looked favorable, though no direct comparison with experiment was possible. Larger errors marred the bromine and uranium +4 ion DFT/MRCI calculations, resulting in relative errors with experiment of 11-22%. It is possible these errors can be reduced by increasing the basis set size, which will be difficult in the case of uranium, but until a DFT/MRCI method

which can preserve symmetry in the eigenvalues is developed, these errors will likely not change much. The observed trend in the BF, Br, U⁴⁺, and U⁵⁺ calculations indicate that the degeneracy error impact on DFT/MRCI accuracy is reduced in systems with larger spin-orbit splittings.

4.4 *Future Work*

The results of this research listed in Appendix C and the previous chapter suggest several avenues for future work. The future research proposed below is ordered by the scope of the research and the estimated time required. Either way, the accuracy and efficiency of the DFT/MRCI method is intriguing, and it is definitely worthy of further study. Understanding the theoretical basis behind the success of the model is crucial.

4.4.1 DFT/MRCI with Other Correlation Density Functionals. One research project spinning off from this work is a relatively small scale project. All results obtained in Appendix B and chapter three were obtained using the CPBE96 GGA correlation-only density functional. Original results obtained by Grimme and Waletzke and later, Kleinschmidt *et al* used a hybrid GGA density functional.

As research into DFT continues, especially development of exchange-correlation density functionals, John Perdew’s vision of the development of more accurate density functionals follows a certain progression that he calls “Jacob’s Ladder” [103]. The analogy, beginning at the bottom rung on “Earth” with Hartree theory, and ending on the top rung in “Heaven” with chemical accuracy, follows the progression

- Rung 0 – Hartree theory “Earth”
- Rung 1 – Local density only (LDA).
- Rung 2 – Explicit dependence on gradients of the density (GGA functionals).
- Rung 3 – Explicit dependence on kinetic energy density (meta-GGA functionals).

- Rung 4 – Explicit dependence on occupied orbitals (hybrid functionals).
- Rung 5 – Fully non-local explicit dependence on unoccupied orbitals.
- Rung 6 – Chemical Accuracy “Heaven”

To date, DFT/MRCI performed by Grimme and Waletzke, Kleinschmidt *et al*, and this work used GGA density functionals only, corresponding to the second rung on Jacob’s Ladder. However, current development of functionals has progressed to step three on Jacob’s Ladder, with the availability of meta-GGA density functionals.

It would be interesting to reproduce the work done here using range of LDA and meta-GGA correlation-only density functionals. Development of damping parameters should proceed along the lines presented in Appendix B and chapter three, and a reexamination of accuracy and efficiency of this DFT/MRCI method on the CO, BF, Br, and uranium ion systems would be of interest. A possible result of this proposed work would lead to a better understanding of the accuracy of the DFT/MRCI method as various density functional approximations are used, progressing up “Jacob’s Ladder” as envisioned by Perdew.

This research could proceed with the DFT/MRCI model as is, using the file-based interface between COLUMBUS and NWChem. However, as of version 4.7, NWChem is unable to perform TDDFT calculations using meta-GGA density functionals.

4.4.2 Integration of DFT Within SCFPQ using Abelian Point Groups .

The file-based DFT interface between NWChem and COLUMBUS provided a method to use Kohn-Sham orbitals and correlation energy from a DFT calculation for use in COLUMBUS calculations. The inability to use point group symmetry in the DFT/MRCI calculation complicated final state assignment, as well as uncovered bugs in the workings of the SOCI code CIUDG. Additionally, subtle differences between the behavior of NWChem and SCFPQ led to discrepancies in the total DFT energies produced by both programs.

By developing an *in situ* numerical integration capability within SCFPQ, as well as implementation of various density functionals, the file-based interface could be eliminated in favor of a completely self-consistent DFT capability within SCFPQ. It would be easier to implement point group symmetry through this approach, than to expand the file-based interface between the two independent programs to incorporate symmetry.

The computational methods necessary to implement a restricted Kohn-Sham DFT approach are well documented, an incomplete list of references include [10] [59] [97] [96] [65], just to name a few.

In order to implement a grid-based DFT capability within SCFPQ, beyond implementation of the density functionals, an ability to numerically integrate these functionals and their functional derivatives over all space, or some subset of space, using the one- and two-electron density produced during each iteration is needed. If the use of a hybrid exchange functional is desired, the exchange portion of the two-electron Fock matrix will have to be identified and modified. Additionally, the ability to evaluate basis functions at grid points is necessary.

The basic routines for a set of density functionals, plus the grid numerical quadrature routines have been developed and are in place, as are additional utilities for evaluating basis functions at various points in space. The only step that remains is the final development, integration, testing and validation of the DFT specific parts of the code.

4.4.3 Hybrid Exchange-Correlation Density Functional Implementation.

While the model developed in this work was based on a correlation-only density functional, research into density functionals indicates that using 100% exact exchange without any exchange functional mixture is not the most accurate approach [102]. Research by Perdew *et al* indicates the optimal mixture of exact HF exchange and exchange functional in hybrid density functionals ranges from 20 to 30% exact exchange, 70 to 80% exchange functional.

Additional work on this implementation of the DFT/MRCI model would be necessary in order to implement the use of a hybrid exchange-correlation functional. If the *in situ* DFT within SCFPQ was developed to enable use of hybrid exchange functionals, then a detailed investigation of the necessary modifications to diagonal CI matrix elements is in order. Recall that in Grimme and Waletzke's work, their diagonal CI matrix element manipulations led to spin multiplicity limitations in their model, as well as three additional empirical parameters. Careful study of the inclusion of a hybrid exchange functional into this DFT/MRCI model is required to see if a hybrid exchange-correlation density functional could be used in conjunction with the CIUDG GUGA based CI code without introducing spin multiplicity limitations or additional empirical parameters.

Implementation of a hybrid exchange-correlation density functional within this DFT/MRCI model represents a major research effort. It would require the development of a grid-based DFT capability capable of using hybrid functionals within SCFPQ before starting. If this capability is in place, careful study of the problem, plus significant manipulation of the existing DFT/MRCI model would be necessary.

4.4.4 Investigations into the Theoretical Basis of the DFT/MRCI Method. A final, and more open-ended research spin-off from this work is to seriously investigate what mechanisms in this hybrid DFT and CI model are responsible for the accuracy and efficiency observed, in this work, and in the work by Grimme, Waletzke, and Kleinschmidt, as well as others.

A limitation to the Kohn-Sham approach to density functional theory is the inability to systematically improve upon the results obtained with an approximate exchange-correlation density functional. In wave function based approaches, improvement of the results is possible via many methods, from many body perturbation theory, to configuration interaction, among others.

Conceptual difficulties remain in the fictitious Hamiltonian approach in applying these methods to density functional theory results. A serious, long term research effort

focused on finding the theoretical basis for the successes behind the DFT/MRCI model may yield important results in the attempt to improve upon the successes of DFT. Such a theoretical description might account for such features observed here as the absolute error banding observed in the density plots shown in Appendix B.

4.5 *Summary*

All in all, the aims of this research project were achieved, in that an accurate and efficient DFT/MRCI model was successfully implemented based upon a correlation-only GGA functional and implemented within a GUGA CI computational framework. The resulting model had no spin multiplicity limitations inherent in the original model by Grimme and Waletzke and added one- and two-component relativistic effects, enabling application of the method to heavy element compounds.

Using the CPBE96 correlation functional, a set of two damping parameters were obtained by locating in the p_1/p_2 parameter space the values which minimized the averaged, normalized error between the DFT/MRCI excitation energy for a given transition and the corresponding FCI result for the same transition. The training set used consisted of the first two rows of the periodic table, focusing mainly on atomic calculations.

The model developed was successfully tested, first using small, minimal basis calculations, then using larger molecular and atomic applications. A carbon monoxide calculation demonstrated the DFT/MRCI capabilities in a non-relativistic calculation, producing relative errors with respect to measured experimental values of 1.3% for the $^1\Sigma^+$ to $^3\Pi$ transition and 12.2% for the $^1\Sigma^+$ to $^1\Pi$ electronic transition with an overall reduction in CI expansion size of a factor of 43. Similar trends were observed in this DFT/MRCI calculation as were reported by Grimme and Waletzke [63]. Carbon monoxide DFT/MRCI results are listed in Table 13.

Scalar relativistic and spin-orbit capability was demonstrated using calculations on boron fluoride and the bromine atom. This DFT/MRCI model was unable to

accurately resolve the 22 cm^{-1} splitting of the ${}^3\Pi$ state in boron fluoride, though it did achieve a respectable relative error for the ${}^1\Sigma^+ \rightarrow {}^3\Pi$ transition with experiment of roughly 3% with a reduction in CI expansion length of a factor of 46. Although Kleinschmidt *et al* [76] were more successful at resolving the spin-orbit splitting, their reported excitation was in good agreement with the result obtained using this model. Boron fluoride DFT/MRCI results are listed in Table 14.

The next DFT/MRCI calculation on the bromine atom demonstrated that this implementation of the DFT/MRCI model could achieve moderate accuracy on a heavy element with large spin-orbit splitting. Additionally, it demonstrated this ability on a system that neither the original Grimme and Waletzke nor Kleinschmidt methods could calculate, since it had a doublet spin-multiplicity. An unexpected doubling of the eigenvalue degeneracies were observed in the odd-electron C_1 calculation on bromine, which were attributed to a bug in the CIUDG code not associated with the DFT/MRCI model. For the bromine atom, a relative error in the ${}^2P_{3/2}$ to ${}^2P_{1/2}$ electronic transition with experiment of roughly 20% was achieved with a factor of 33 reduction in the CI expansion length. Table 15 lists the bromine DFT/MRCI excitation energies.

For the uranium ionic and molecular calculations, work had to be done to convert the basis set used to obtain the results reported in chapter two, using $3sd$ basis functions, to $1s$ and $3d$ functions compatible with the DFT code. The converted basis set had fewer s and d functions, though the results for $f \rightarrow f$ transitions were essentially unaffected. Table 52 in Appendix C compares MR-SOCISD results on uranium +5 using both the original and converted basis set.

The DFT/MRCI calculation on the uranium +4 ion produced results reminiscent of the bromine calculation. Relative errors with experiment of approximately 15% were achieved in the ${}^3H_{4g}$ to ${}^3F_{2g}$ electronic transition, with a factor of 21 reduction in the CI expansion size. Degeneracy errors significantly complicated wave function analysis and state assignment. Table 17 list the DFT/MRCI excitation energies obtained and their relative errors with experiment.

The best DFT/MRCI calculation on an odd-electron heavy element was achieved on the uranium +5 ion, which was another odd-electron doublet system. A relative error in the excitation energy of approximately 9% for the ${}^2F_{\frac{5}{2}}$ to ${}^2F_{\frac{7}{2}}$ transition was achieved when compared with measured experiment values, with a factor of 46 reduction in CI expansion size. Table 16 show the DFT/MRCI results for the uranium +5 ion.

The final application of the DFT/MRCI model on the uranyl (UO_2^{2+}) ion yields results that compared favorably with MR-SOCISD calculations performed [9] for several orders of magnitude less computational effort in terms of the dimensions of the CI expansions involved. The DFT/MRCI calculation used a small expansion of nearly 40,000 CSFs, while the MR-SOCISD calculation involved nearly 5,000,000 CSFs. The DFT/MRCI results on uranyl fluorescent series compared favorably with those measured in a range of crystals [111]. Table 19 shows this comparison for uranyl.

Suggestions for future work include repeating the analysis done here with a meta-GGA density functional, as well as integrating DFT within the SCFPQ program to eliminate the need for a file-based interface with NWChem. This would facilitate the incorporation of symmetry into the DFT/MRCI model. Further investigations into adapting this model for use with a hybrid exchange-correlation density functional might improve accuracy of the method, while more work into the theoretical basis for the successes of the DFT and CI method could lead to further improvements in accuracy and computational efficiency.

Appendix A. List of Acronyms

- B3LYP** Becke Three Parameter Hybrid Density Functional
- BHLYP** Becke half-and-half hybrid exchange correlation functional
- BLAS** Basic Linear Algebra System
- CAS** Complete Active Space
- CASSCF** Complete Active Space Self Consistent Field
- CCCBDB** Computational Chemistry Comparison and Benchmark DataBase
- cc-pVDZ** Correlation Consistent Valence Double- ζ with Polarization Functions
- CI** Configuration Interaction
- CIS** Configuration Interaction Singles
- CISD** Configuration Interaction Singles and Doubles
- CIUDG** Configuration Interaction Unitary Diagonalize
- CPBE96** Perdew Burke and Ernzerhof pure correlation functional
- CSF** Configuration State Function
- CSFs** Configuration State Functions
- DFT** Density Functional Theory
- DFT/MRCI** Density Functional Theory Multireference Configuration Interaction Hybrid Model
- DRT** Distinct Row Table
- eV** electron Volts
- FCI** Full Configuration Interaction
- GGA** Generalized Gradient Approximation
- GUGA** Graphical Unitary Group Approach
- HF** Hartree-Fock

HOMO Highest Occupied Molecular Orbital

kJ kilo Joule

LDA Local Density Approximation

mH milli Hartrees

MRCI Multireference Configuration Interaction

MR-CISD Multi-reference Configuration Interaction, Single and Double Excitations

MR-SOCISD Multi-reference Spin-Orbit Configuration Interaction Singles and
Doubles

NIST National Institute of Standards and Technology

PBE Perdew Burke and Ernzerhof

RECP Relativistic Effective Core Potential

RECPs Relativistic Effective Core Potentials

RMS Root Mean Square

ROHF Restricted-Open Hartree Fock

SCF Self-Consistent Field

SOCI Spin-orbit Configuration Interaction

TDDFT Time Dependent Density Functional Theory

Appendix B. DFT/MRCI Damping Parameter Selection

This appendix contains the results of FCI calculations on the atomic and molecular systems used to determine the optimal damping parameters used in the uranium calculations, as well as DFT/MRCI calculations performed over a wide range of damping parameters, p_1 and p_2 . All DFT/MRCI calculations were performed on a 20 by 20 grid in the damping parameter space. Statistical analysis of the error between the electronic excitation energy as computed by DFT/MRCI and FCI is also listed.

For each system examined, a density plot representing the absolute value of the error between the DFT/MRCI and FCI for the lowest, spin-multiplicity allowed electronic transition. The range of the damping parameters in the density plots are $0 \leq p_1 \leq 1, 0 \leq p_2 \leq 10$.

The squares of the Hartree-Fock configurations from *ab initio* calculations on each of the systems is given in Table B. It is a measure of the multi-reference character of system.

Table 20: MR-CISD Hartree-Fock Configuration Coefficients For Systems Used for Damping Parameter Determination

System	Basis Set	c_0^2	State
H ₂	cc-pVDZ	0.983859	$1\Sigma_g^+$
H ₂	cc-pVTZ	0.985199	$1\Sigma_g^+$
He	cc-pVDZ	0.992739	$1S$
He	cc-pVTZ	0.992673	$1S$
Li,	cc-pVDZ	0.999924	$2S$
Li,	cc-pVTZ	0.999664	$2S$
Be	cc-pVDZ	0.906694	$1S$
Be	cc-pVTZ	0.904388	$1S$
B	cc-pVDZ	0.928991	$2P$
C	cc-pVDZ	0.951450	$3P$
N	cc-pVDZ	0.969066	$4S$
O	cc-pVDZ	0.967909	$3P$
F	cc-pVDZ	0.970048	$2P$
Ne	cc-pVDZ	0.972435	$1S$
Be ₂	cc-pVDZ	0.787166	$1\Sigma_g^+$

B.1 Hydrogen Molecule, cc-pVDZ Basis

The H₂ cc-pVDZ calculation had 10 basis functions. The active space used in the DFT/MRCI calculations for H₂ was a CAS over the 1 σ , and 2 σ orbitals, with the four highest energy virtual orbitals frozen.

Table 21: Hydrogen Molecule, cc-pVDZ Basis Set, Full CI Results

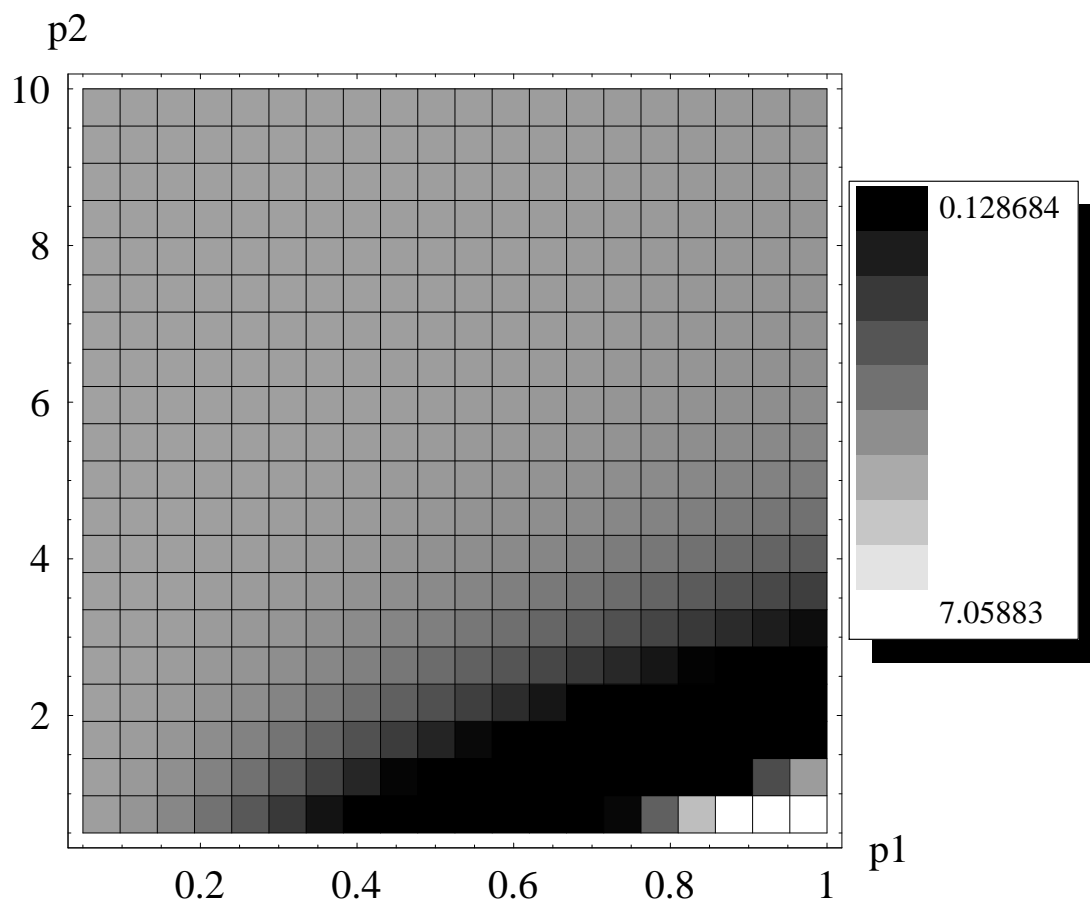
Eigenvalue	Energy(au)	Spin Quantum Number(S)
1	-1.1634454317	0.00
2	-0.7719930623	1.00
3	-0.6526531835	0.00
4	-0.5172916288	1.00
5	-0.3771969905	0.00
6	-0.1712406269	1.00
7	-0.0860211873	0.00
8	-0.0260620923	0.00
9	0.0994560644	1.00
10	0.0994560644	1.00

Table 22: DFT/MRCI Error Analysis for Hydrogen Molecule, cc-pVDZ Basis

$p1$	$p2$	Average error (mH)	Standard deviation of error (mH)
$0 \leq p1 \leq 1$	$0 \leq p2 \leq 10$	3.17379	1.43684

In figure 8, the horizontal axis is p_1 , the vertical axis is p_2 , and the absolute error units are milli-Hartrees.

Figure 8: H₂ cc-pVDZ basis DFT/MRCI Absolute Error (mH) with Respect to FCI Results



B.2 Hydrogen Molecule, cc-pVTZ Basis

The H₂ cc-pVTZ calculation had 28 basis functions. The active space used in the DFT/MRCI calculations for H₂ was a CAS over the 1 σ , and 2 σ orbitals, with the eighteen highest energy virtual orbitals frozen.

Table 23: Full CI Results for Hydrogen Molecule, cc-pVTZ Basis

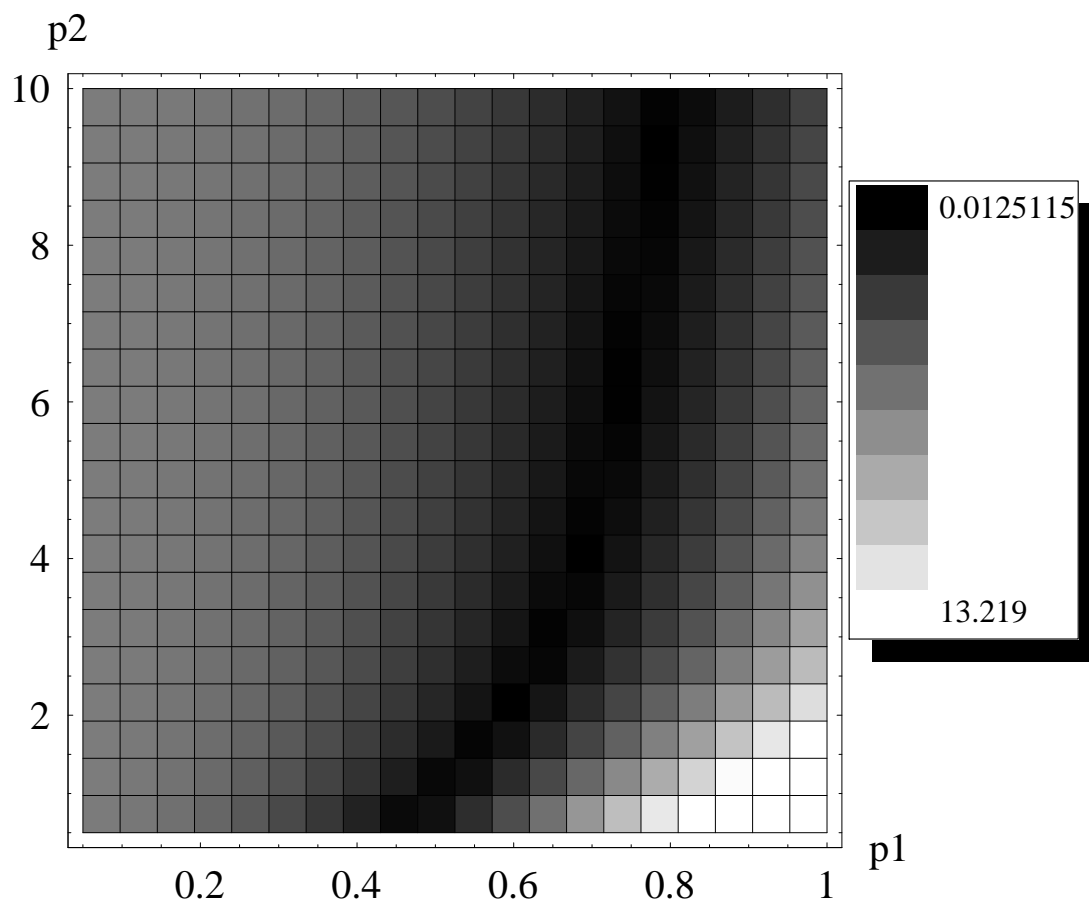
Eigenvalue	Energy(au)	Spin Quantum Number(S)
1	-1.1721405481	0.00
2	-0.7803634789	1.00
3	-0.6771947554	0.00
4	-0.6276575090	1.00
5	-0.5486996299	0.00
6	-0.3915914198	1.00
7	-0.3904709905	1.00
8	-0.3904709905	1.00
9	-0.2612510066	0.00
10	-0.2455885332	0.00
11	-0.2455885332	0.00
12	-0.1223283192	0.00
13	0.0141686518	1.00
14	0.0605395246	1.00
15	0.0682666734	0.00
16	0.0685243592	0.00
17	0.0685243592	0.00
18	0.0987817252	1.00
19	0.0987817252	1.00
20	0.1409960535	0.00

In figure 9, the horizontal axis is p_1 , the vertical axis is p_2 , and the absolute error units are milli-Hartrees.

Table 24: DFT/MRCI Error Analysis for Hydrogen Molecule, cc-pVTZ Basis

$p1$	$p2$	Average error (mH)	Standard deviation of error (mH)
$0 \leq p1 \leq 1$	$0 \leq p2 \leq 10$	0.832851	2.98819

Figure 9: H₂ cc-pVTZ basis DFT/MRCI Absolute Error (mH) with Respect to FCI Results



B.3 Helium Atom, cc-pVDZ Basis

The He atom cc-pVDZ calculation had five basis functions. The active space used in the DFT/MRCI calculations for He was a CAS over the $1s$, and $2s$ orbitals. No virtual orbitals were frozen.

Table 25: Full CI Results for Helium Atom, cc-pVDZ Basis

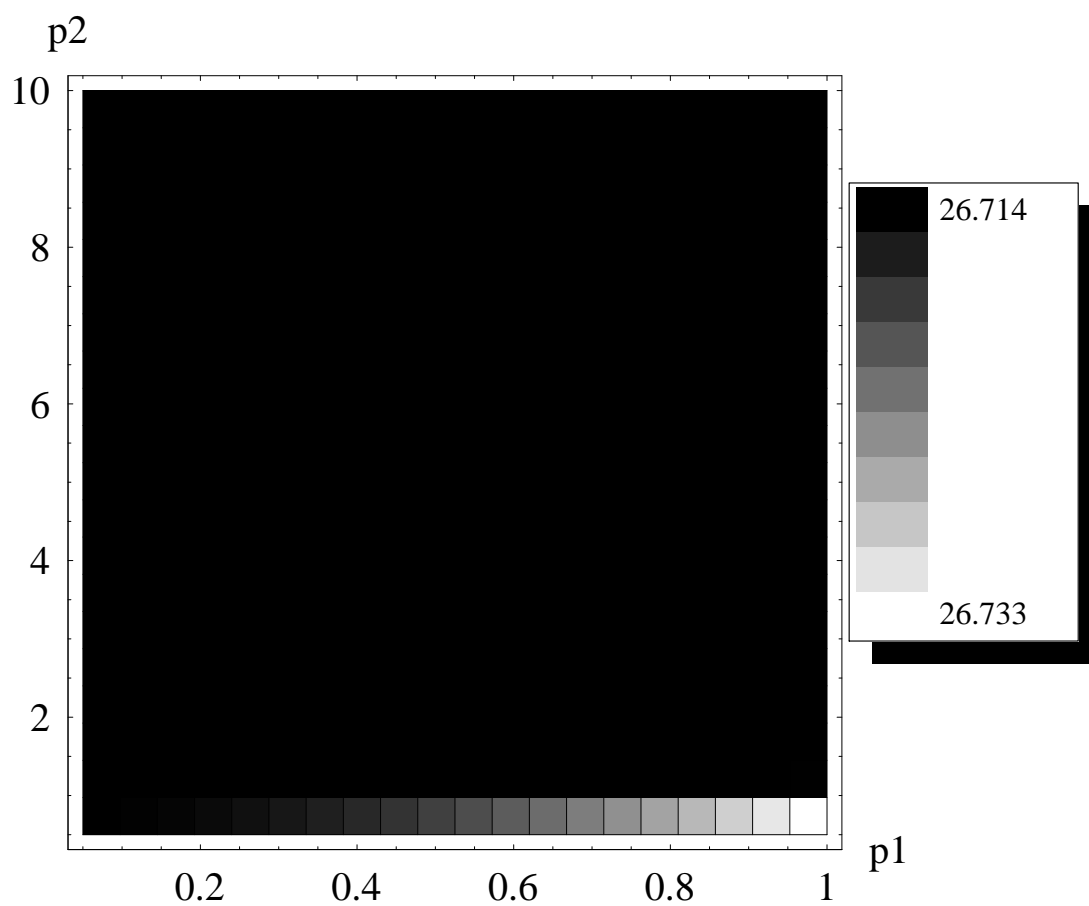
Eigenvalue	Energy(au)	Spin Quantum Number(S)
1	-2.8875948311	0.00
2	-1.4011632767	1.00
3	-0.9521509999	0.00
4	-0.3846928589	1.00
5	-0.3846928589	1.00
6	-0.3846928589	1.00
7	-0.0140305136	0.00
8	-0.0140305136	0.00
9	-0.0140305136	0.00
10	0.6027713426	0.00
11	1.4479742314	1.00
12	1.4479742314	1.00
13	1.4479742314	1.00
14	1.5006676821	0.00
15	1.5006676821	0.00
16	1.5006676821	0.00
17	2.4194075597	1.00
18	2.4194075597	1.00
19	2.4194075597	1.00
20	2.5468195066	0.00
21	2.5468195066	0.00
22	2.5468195066	0.00
23	2.5468195066	0.00
24	2.5468195066	0.00
25	2.7586172117	0.00

In figure 10, the horizontal axis is p_1 , the vertical axis is p_2 , and the absolute error units are milli-Hartrees.

Table 26: DFT/MRCI Error Analysis for Helium Atom, cc-pVDZ Basis

$p1$	$p2$	Average error (mH)	Standard deviation of error (mH)
$0 \leq p1 \leq 1$	$0 \leq p2 \leq 10$	-26.7143	1.993013

Figure 10: He Atom, cc-pVDZ basis DFT/MRCI Absolute Error (mH) with Respect to FCI Results



B.4 Helium Atom, cc-pVTZ Basis

The He atom cc-pVTZ calculation had 14 basis functions. The active space used in the DFT/MRCI calculations for He was a CAS over the $1s$, and $2s$ orbitals. The seven highest energy virtual orbitals were frozen.

Table 27: Full CI Results for Helium Atom, cc-pVTZ Basis

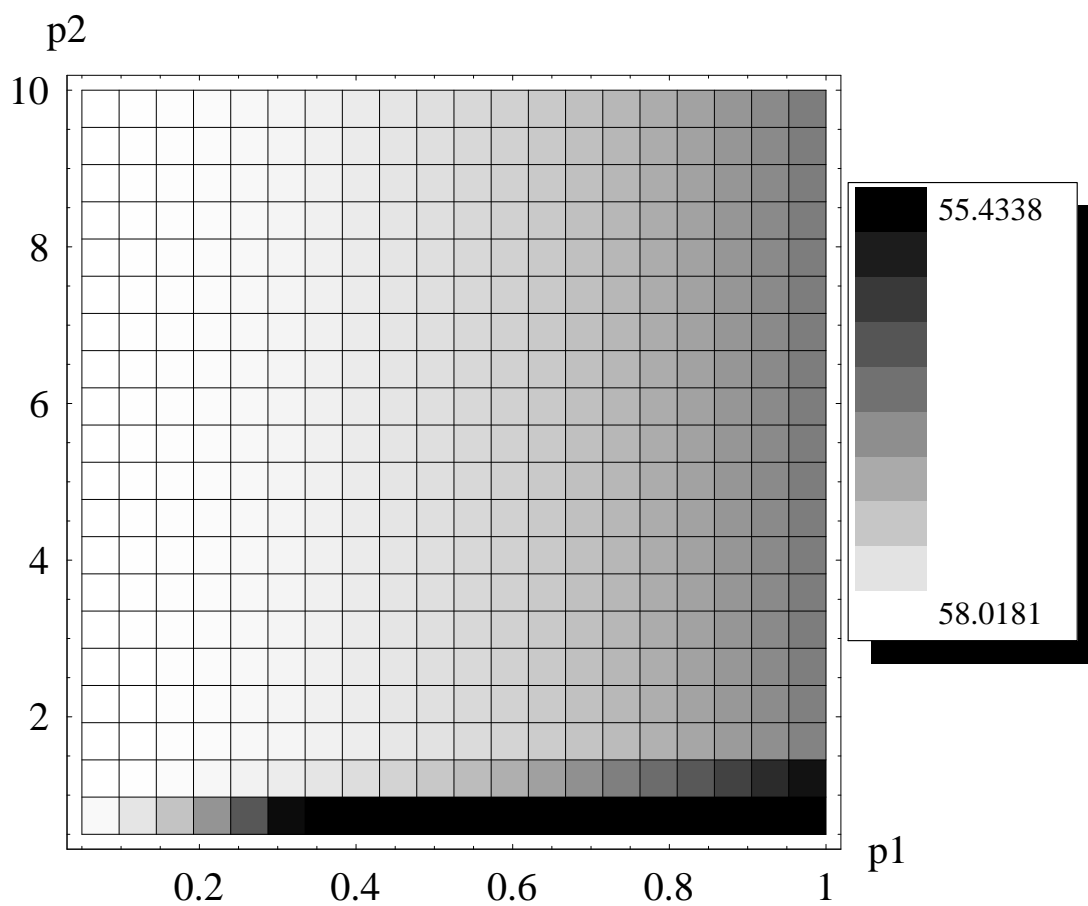
Eigenvalue	Energy(au)	Spin Quantum Number(S)
1	-2.8970673069	0.00
2	-1.9334705002	1.00
3	-1.7529254971	0.00
4	-1.2532701076	1.00
5	-1.2532701076	1.00
6	-1.2532701076	1.00
7	-1.0165706840	0.00
8	-1.0165706840	0.00
9	-1.0165706840	0.00
10	-0.4017414794	0.00
11	0.1064824663	1.00
12	0.1064824663	1.00
13	0.1064824663	1.00
14	0.1382686250	0.00
15	0.1382686250	0.00
16	0.1382686250	0.00
17	0.6636303193	1.00
18	0.7313588535	1.00
19	0.7313588535	1.00
20	0.7313588535	1.00

In figure 11, the horizontal axis is p_1 , the vertical axis is p_2 , and the absolute error units are milli-Hartrees.

Table 28: DFT/MRCI Error Analysis for Helium Atom, cc-pVTZ Basis

$p1$	$p2$	Average error (mH)	Standard deviation of error (mH)
$0 \leq p1 \leq 1$	$0 \leq p2 \leq 10$	57.9311	0.263939

Figure 11: He Atom, cc-pVTZ Basis DFT/MRCI Absolute Error (mH) with Respect to FCI Results



B.5 Lithium Atom, cc-pVDZ Basis

The Li atom cc-pVDZ calculation had 14 basis functions. The active space used in the DFT/MRCI calculations for Li was a CAS over the $1s$, $2s$, $2p$, $3s$, and $3p$ orbitals. No virtual orbitals were frozen.

Table 29: Full CI Results for Lithium Atom, cc-pVDZ Basis

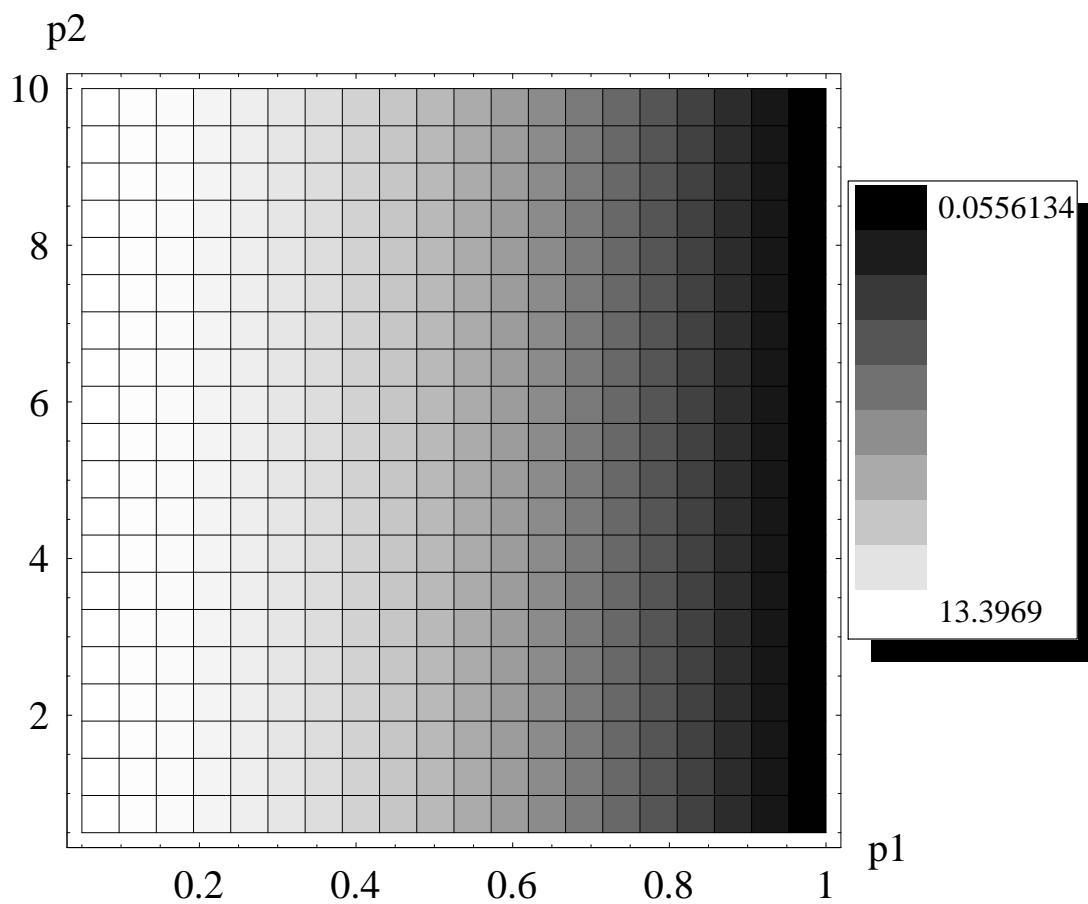
Eigenvalue	Energy(au)	Spin Quantum Number(S)
1	-7.4326345923	0.50
2	-7.3648490641	0.50
3	-7.3648490641	0.50
4	-7.3648490641	0.50
5	-7.2572185901	0.50
6	-7.2572185901	0.50
7	-7.2572185901	0.50
8	-7.2469567861	0.50
9	-7.1026935868	0.50
10	-7.1026935868	0.50
11	-7.1026935868	0.50
12	-7.1026935868	0.50
13	-7.1026935868	0.50
14	-5.2980319280	0.50
15	-5.2531598973	1.50
16	-5.2531598973	1.50
17	-5.2531598973	1.50
18	-5.2253952659	0.50
19	-5.2253952659	0.50
20	-5.2253952659	0.50

In figure 12, the horizontal axis is p_1 , the vertical axis is p_2 , and the absolute error units are milli-Hartrees.

Table 30: DFT/MRCI Error Analysis for Li Atom, cc-pVDZ Basis

$p1$	$p2$	Average error (mH)	Standard deviation of error (mH)
$0 \leq p1 \leq 1$	$0 \leq p2 \leq 10$	8.37894	4.22027

Figure 12: Li Atom, cc-pVDZ Basis DFT/MRCI Absolute Error(mH) with Respect to FCI Results



B.6 Lithium Atom, cc-pVTZ Basis

The Li atom cc-pVTZ calculation had 30 basis functions. The active space used in the DFT/MRCI calculations for Li was a CAS over the $1s$, $2s$, $2p$, $3s$, and $3p$ orbitals. The highest energy virtual orbital was frozen. ROHF open-shell coefficients corresponding to the high-spin 2S state were used to generate the initial orbitals, with exchange-correlation potential integrals from an unrestricted DFT calculation.

Table 31: Full CI Results for Lithium Atom, cc-pVTZ Basis

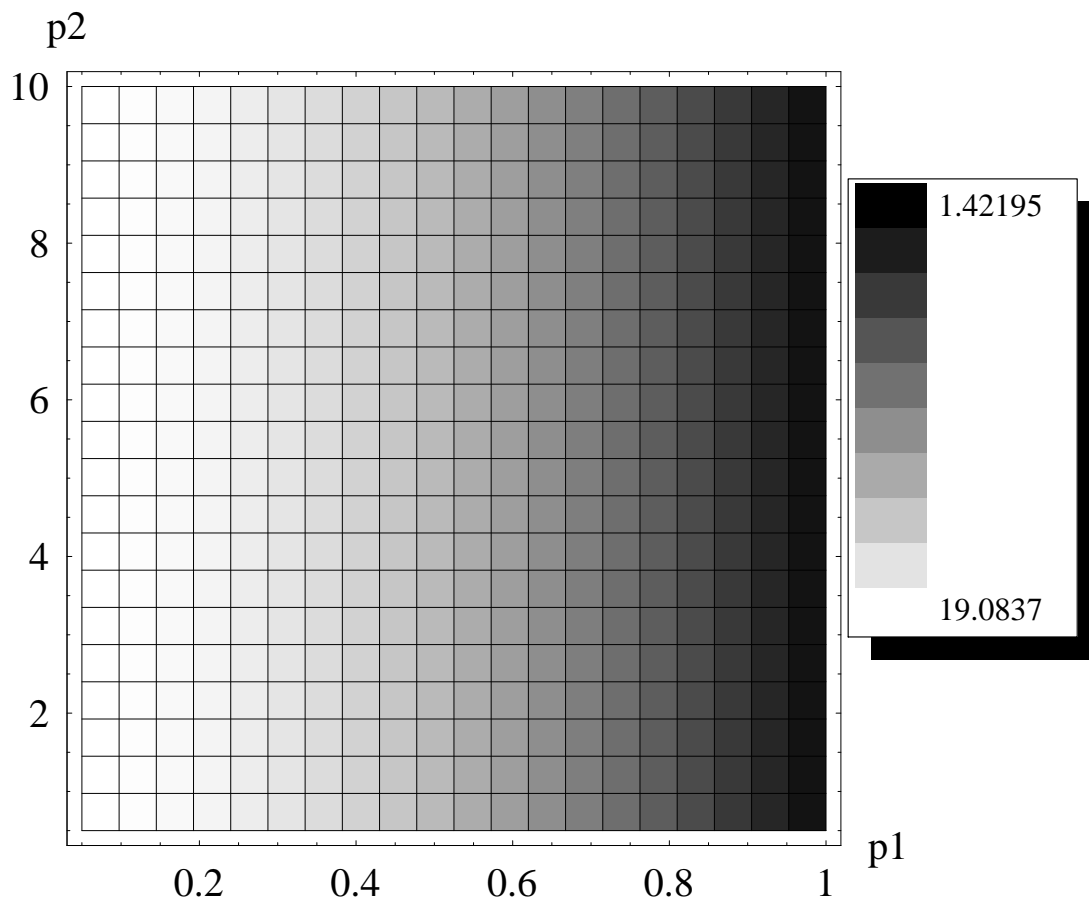
Eigenvalue	Energy(au)	Spin Quantum Number(S)
1	-7.4332546271	0.50
2	-7.3654330817	0.50
3	-7.3654330817	0.50
4	-7.3654330817	0.50
5	-7.2827258411	0.50
6	-7.2761519403	0.50
7	-7.2761519403	0.50
8	-7.2761519403	0.50
9	-7.2021446003	0.50
10	-7.2021446003	0.50
11	-7.2021446003	0.50
12	-7.2021446003	0.50
13	-7.2021446003	0.50
14	-7.0789295728	0.50
15	-7.0789295728	0.50
16	-7.0789295728	0.50
17	-7.0370981897	0.50
18	-6.7539585204	0.50
19	-6.7539585204	0.50
20	-6.7539585204	0.50
21	-6.7539585204	0.50
22	-6.7539585204	0.50
23	-6.7260996854	0.50
24	-6.7260996854	0.50
25	-6.7260996854	0.50
26	-6.7260996854	0.50
27	-6.7260996854	0.50
28	-6.7260996854	0.50
29	-6.7260996854	0.50
30	-5.3317686889	0.50

Table 32: DFT/MRCI Error Analysis for Li Atom, cc-pVTZ Basis

$p1$	$p2$	Average error (mH)	Standard deviation of error (mH)
$0 \leq p1 \leq 1$	$0 \leq p2 \leq 10$	12.2333	5.61206

In figure 13, the horizontal axis is p_1 , the vertical axis is p_2 , and the absolute error units are milli-Hartrees.

Figure 13: Li Atom, cc-pVTZ Basis DFT/MRCI Absolute Error (mH) with Respect to FCI Results



B.7 Beryllium Atom, cc-pVDZ Basis

The Be atom cc-pVDZ calculation had 14 basis functions. The active space used in the DFT/MRCI calculations for Be was a CAS over the $2s$, $2p$, and $3s$ orbitals. The $1s$ core electrons were frozen. No virtual orbitals were frozen.

Table 33: Full CI Results for Beryllium Atom, cc-pVTZ Basis

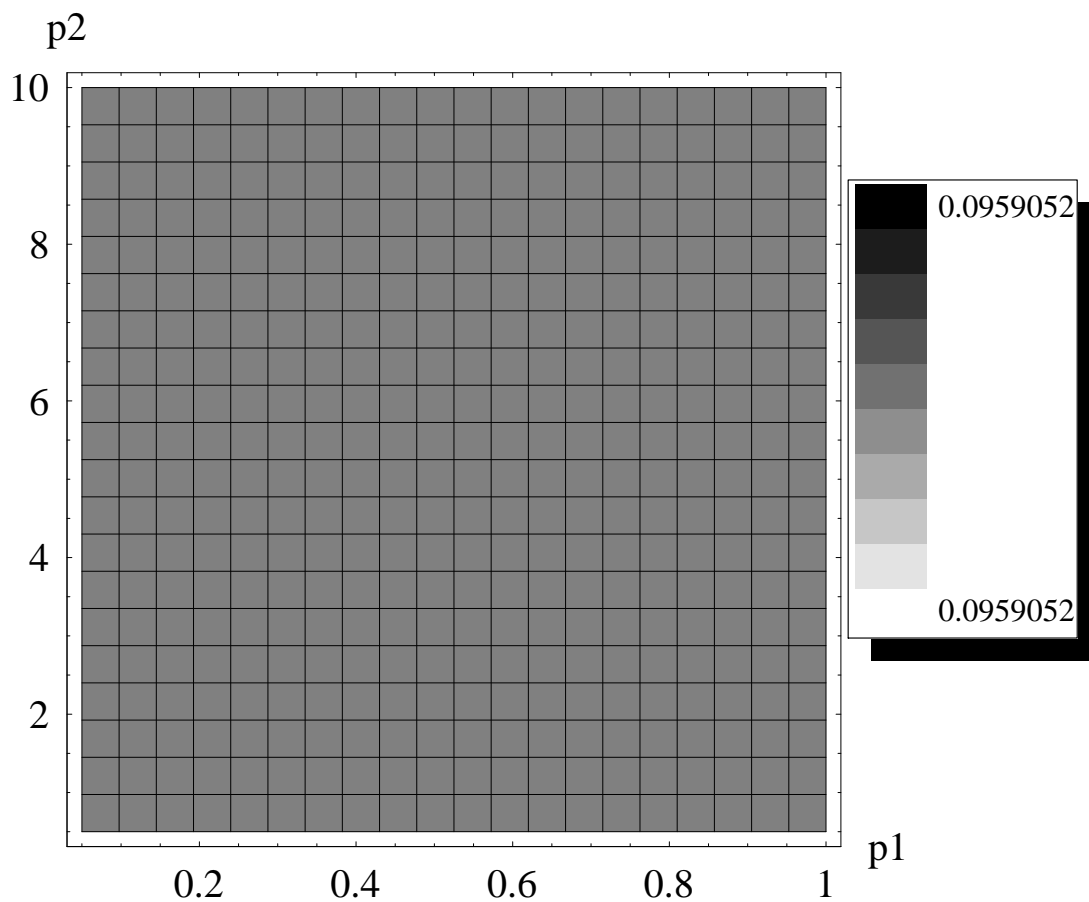
Eigenvalue	Energy(au)	Spin Quantum Number(S)
1	-14.6170550612	0.00
2	-14.5160407645	1.00
3	-14.5160407645	1.00
4	-14.5160407645	1.00
5	-14.4097625863	0.00
6	-14.4097625863	0.00
7	-14.4097625863	0.00
8	-14.3423297244	1.00
9	-14.3423297243	1.00
10	-14.3423297243	1.00
11	-14.3324015006	0.00
12	-14.3324015006	0.00
13	-14.3324015006	0.00
14	-14.3324015006	0.00
15	-14.3324015006	0.00
16	-14.2603499935	1.00
17	-14.2518898465	0.00
18	-14.2223192621	0.00
19	-14.2223192621	0.00
20	-14.2223192620	0.00

Table 34: DFT/MRCI Error Analysis for Be Atom, cc-pVDZ Basis

$p1$	$p2$	Average error (mH)	Standard deviation of error (mH)
$0 \leq p1 \leq 1$	$0 \leq p2 \leq 10$	-0.0959052	0.0

In figure 14, the horizontal axis is p_1 , the vertical axis is p_2 , and the absolute error units are milli-Hartrees.

Figure 14: Be Atom, cc-pVDZ Basis DFT/MRCI Absolute Error (mH) with Respect to FCI Results



B.8 Beryllium Atom, cc-pVTZ Basis

The Be atom cc-pVTZ calculation had 30 basis functions. The active space used in the DFT/MRCI calculations for Be was a CAS over the $2s$, $2p$, and $3s$ orbitals. The $1s$ core electrons were frozen. The eleven highest energy virtual orbitals were frozen.

Table 35: Full CI Results for Beryllium Atom, cc-pVTZ Basis

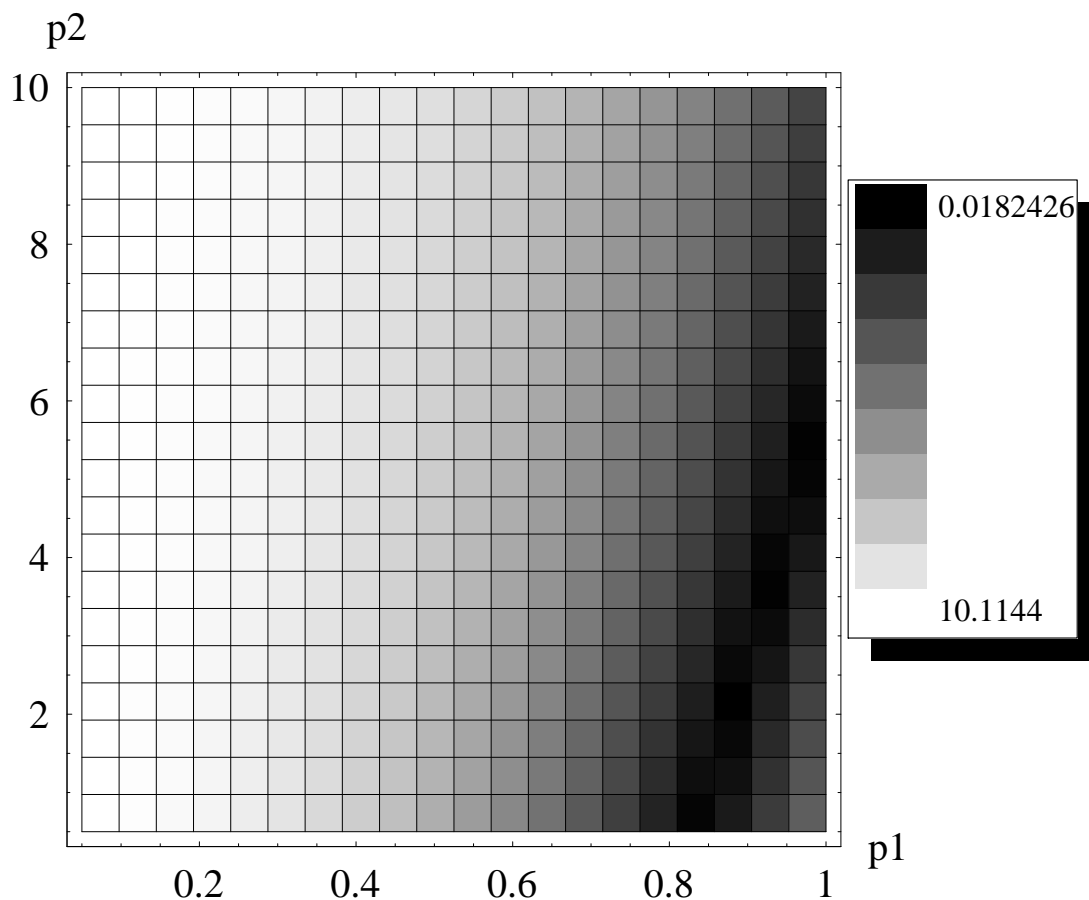
Eigenvalue	Energy(au)	Spin Quantum Number(S)
1	-14.6194922142	0.00
2	-14.5187820394	1.00
3	-14.5187820394	1.00
4	-14.5187820394	1.00
5	-14.4196053512	0.00
6	-14.4196053512	0.00
7	-14.4196053512	0.00
8	-14.3500737083	1.00
9	-14.3453786584	1.00
10	-14.3453786584	1.00
11	-14.3453786584	1.00
12	-14.3409231284	0.00
13	-14.3409231283	0.00
14	-14.3409231283	0.00
15	-14.3409231283	0.00
16	-14.3409231283	0.00
17	-14.3209144672	0.00
18	-14.2881970390	1.00
19	-14.2881970390	1.00
20	-14.2881970390	1.00

Table 36: DFT/MRCI Error Analysis for Be Atom, cc-pVTZ Basis

$p1$	$p2$	Average error (mH)	Standard deviation of error (mH)
$0 \leq p1 \leq 1$	$0 \leq p2 \leq 10$	-6.72072	3.37373

In figure 15, the horizontal axis is p_1 , the vertical axis is p_2 , and the absolute error units are milli-Hartrees.

Figure 15: Be Atom, cc-pVTZ Basis DFT/MRCI Absolute Error (mH) with Respect to FCI Results



B.9 Boron Atom, cc-pVDZ Basis

The B atom cc-pVDZ calculation had 14 basis functions. The active space used in the DFT/MRCI calculations for B was a CAS over the $2s$, $2p$, $3s$, and $3p$ orbitals. The $1s$ core electrons were frozen. No virtual orbitals were frozen. ROHF open-shell coefficients corresponding to the high-spin 2P state were used to generate

the initial orbitals, with exchange-correlation potential integrals from an unrestricted DFT calculation.

Table 37: Full CI Results for Boron Atom, cc-pVDZ Basis

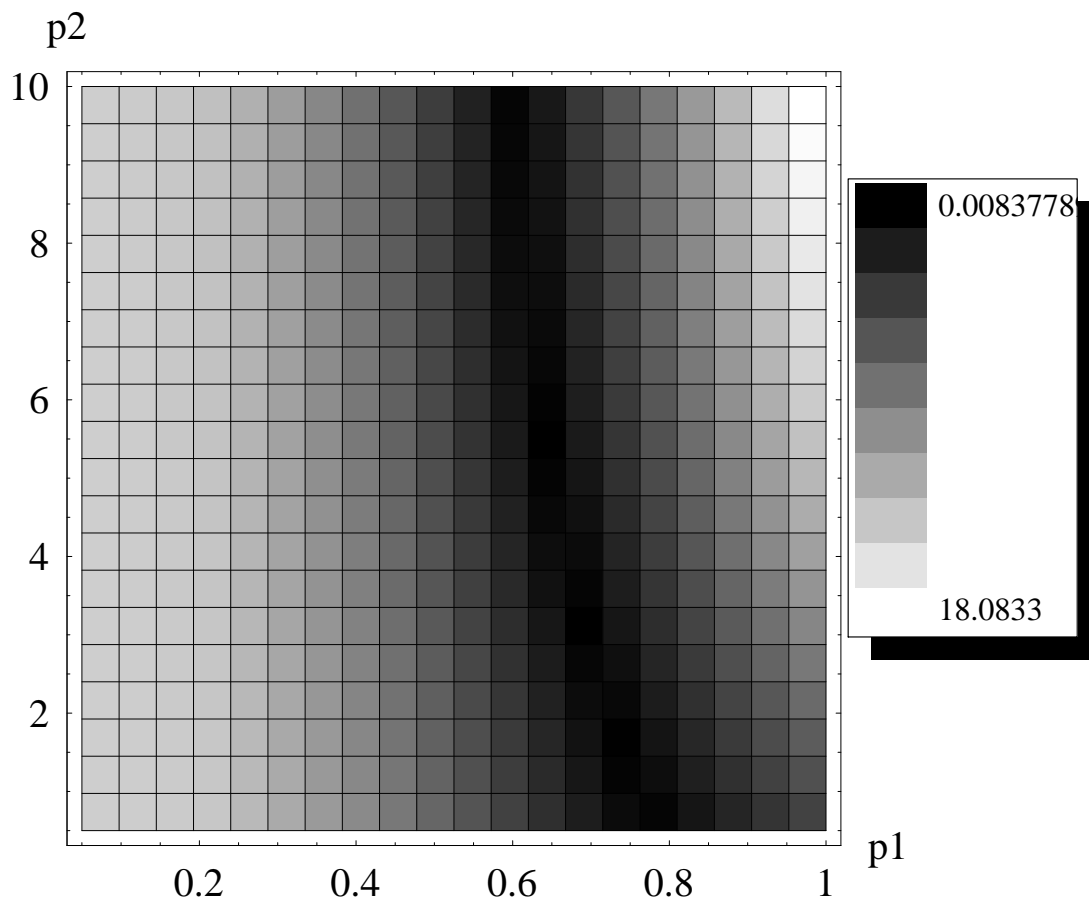
Eigenvalue	Energy(au)	Spin Quantum Number(S)
1	-24.5889055248	0.50
2	-24.5888984561	0.50
3	-24.5888984561	0.50
4	-24.4609115942	1.50
5	-24.4609115942	1.50
6	-24.4609106003	1.50
7	-24.3565727635	0.50
8	-24.3565727635	0.50
9	-24.3565727178	0.50
10	-24.3565722966	0.50
11	-24.3565722966	0.50
12	-24.2874059053	0.50
13	-24.2389721593	0.50
14	-24.2389689817	0.50
15	-24.2389689817	0.50
16	-24.1826143223	0.50
17	-24.1647026709	0.50
18	-24.1646933564	0.50
19	-24.1646933564	0.50
20	-24.1464989570	1.50

Table 38: DFT/MRCI Error Analysis for Boron Atom, cc-pVDZ Basis

$p1$	$p2$	Average error (mH)	Standard deviation of error (mH)
$0 \leq p1 \leq 1$	$0 \leq p2 \leq 10$	3.55402	9.09908

In figure 16, the horizontal axis is p_1 , the vertical axis is p_2 , and the absolute error units are milli-Hartrees.

Figure 16: B Atom, cc-pVDZ Basis DFT/MRCI Absolute Error (mH) with Respect to FCI Results



B.10 Carbon Atom, cc-pVDZ Basis

The C atom cc-pVDZ calculation had 14 basis functions. The active space used in the DFT/MRCI calculations for C was a CAS over the $2s$, $2p$, $3s$, and $3p$ orbitals. The $1s$ core electrons were frozen. No virtual orbitals were frozen. ROHF open-shell coefficients corresponding to the high-spin 3P state were used to generate the initial orbitals, with exchange-correlation potential integrals from an unrestricted DFT calculation. The large error spot in Figures 17 is a result of shifting of the ground state and the 1S state, probably due to a numerical instability in the iterative matrix diagonalization generated by an ill-conditioned matrix.

A single anomaly occurred during the carbon calculation at $p_1 = 0.96$, $p_2 = 4.0$. The carbon calculation did not yield a meaningful excitation energy at that point in the p_1/p_2 parameter space. This behavior could be due to the introduction of a numerical instability in the carbon calculation at that point on the grid. No other DFT/MRCI calculations exhibited this behavior. Examining a slice through the carbon data as a function of p_2 at $p_1 = 0.96$, a clear, smooth trend was apparent, with the exception of that single data point. Because of the data dropout in the carbon calculation at that particular point, the error for that point was interpolated from neighboring points in the carbon calculation.

Table 39: Full CI results for Carbon Atom, cc-pVDZ Basis

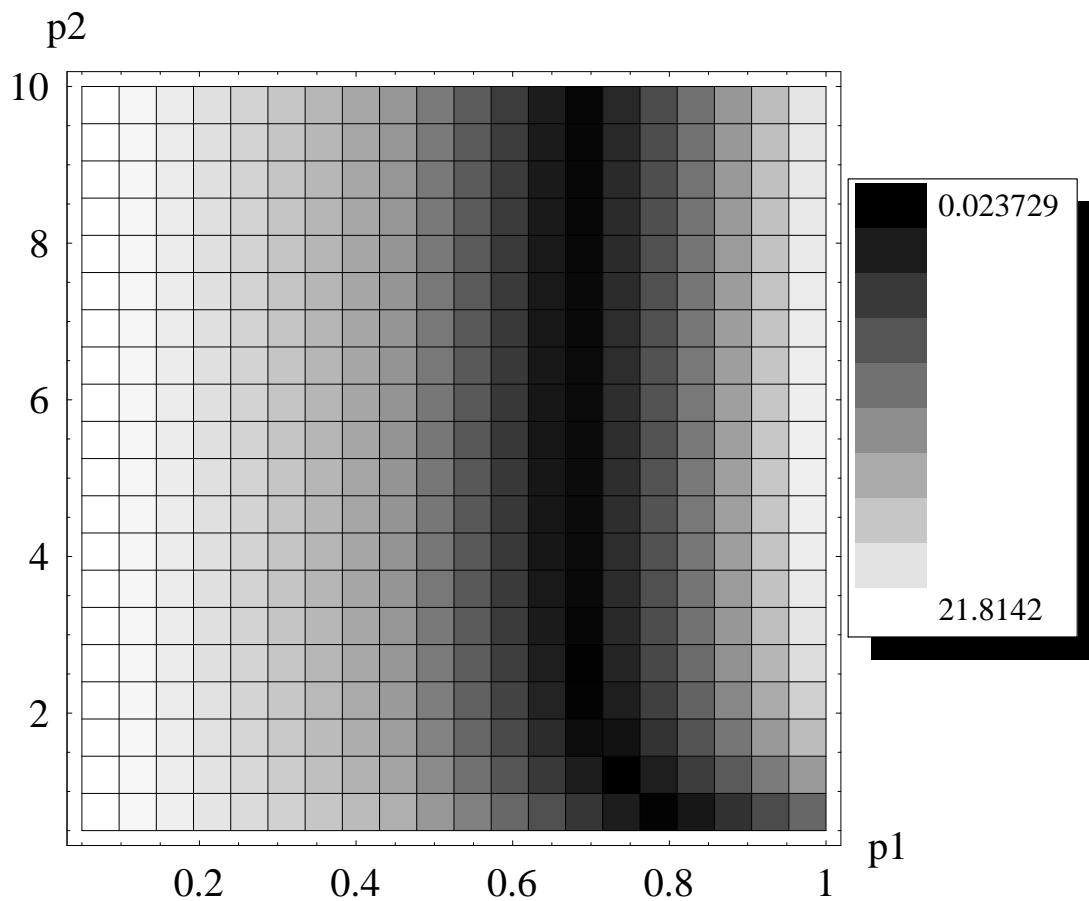
Eigenvalue	Energy(au)	Spin Quantum Number(S)
1	-37.7592125200	1.00
2	-37.7592008135	1.00
3	-37.7592008135	1.00
4	-37.6165280238	2.00
5	-37.4548851325	1.00
6	-37.4548836429	1.00
7	-37.4548836429	1.00
8	-37.4548797964	1.00
9	-37.4548797964	1.00
10	-37.3977324546	1.00
11	-37.3977297417	1.00
12	-37.3977297417	1.00
13	-37.2296166451	1.00
14	-37.1268085912	1.00
15	-37.1268085912	1.00
16	-37.1267894120	1.00
17	-37.1267894120	1.00
18	-37.1267830398	1.00
19	-37.1218806259	1.00
20	-37.1218806259	1.00

Table 40: DFT/MRCI Error Analysis for Carbon Atom, cc-pVDZ Basis

$p1$	$p2$	Average error (mH)	Standard deviation of error (mH)
$0 \leq p1 \leq 1$	$0 \leq p2 \leq 10$	6.62745	15.9442

In figure 17, the horizontal axis is p_1 , the vertical axis is p_2 , and the absolute error units are milli-Hartrees.

Figure 17: C Atom, cc-pVDZ Basis DFT/MRCI Absolute Error (mH) with Respect to FCI Results



B.11 Nitrogen Atom, cc-pVDZ Basis

The N atom cc-pVDZ calculation had 14 basis functions. The active space used in the DFT/MRCI calculations for N was a CAS over the $2s$, $2p$, $3s$, and $3p$ orbitals. The $1s$ core electrons were frozen. No virtual orbitals were frozen. ROHF open-shell coefficients corresponding to the high-spin 4S ground state were used to generate the initial orbitals, with exchange-correlation potential integrals from an unrestricted DFT calculation.

Table 41: Full CI Results for Nitrogen Atom, cc-pVDZ Basis

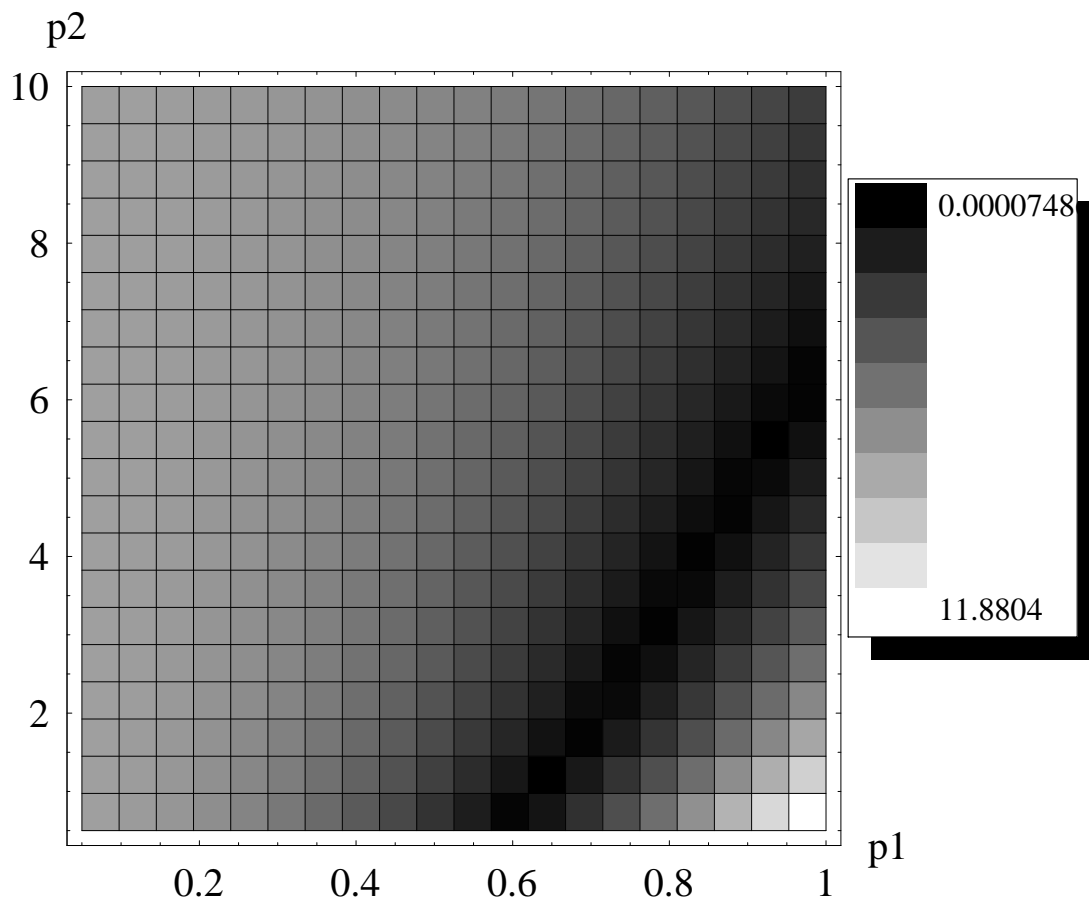
Eigenvalue	Energy(au)	Spin Quantum Number(S)
1	-54.4767066248	1.50
2	-54.0654859868	1.50
3	-54.0654859868	1.50
4	-54.0654859868	1.50
5	-53.5574561262	1.50
6	-53.5574561262	1.50
7	-53.5574561262	1.50
8	-53.5565303513	1.50
9	-53.5565303513	1.50
10	-53.5565303513	1.50
11	-53.5565303513	1.50
12	-53.5565303513	1.50
13	-53.5409323847	1.50
14	-53.5409323847	1.50
15	-53.5409323846	1.50
16	-53.4320611239	1.50
17	-53.3515711786	2.50
18	-53.3503670002	2.50
19	-53.3503670002	2.50
20	-53.3503670002	2.50

Table 42: DFT/MRCI Error Analysis for Nitrogen Atom, cc-pVDZ Basis

$p1$	$p2$	Average error (mH)	Standard deviation of error (mH)
$0 \leq p1 \leq 1$	$0 \leq p2 \leq 10$	3.95767	3.58527

In figure 18, the horizontal axis is p_1 , the vertical axis is p_2 , and the absolute error units are milli-Hartrees.

Figure 18: N Atom, cc-pVDZ Basis DFT/MRCI Absolute Error (mH) with Respect to FCI Results



B.12 Oxygen atom, cc-pVDZ Basis set

The O atom cc-pVDZ calculation had 14 basis functions. The active space used in the DFT/MRCI calculations for N was a CAS over the $2s$, $2p$, $3s$, and $3p$ orbitals. The $1s$ core electrons were frozen. No virtual orbitals were frozen. ROHF open-shell coefficients corresponding to the high-spin 3P ground state were used to generate the initial orbitals, with exchange-correlation potential integrals from an unrestricted DFT calculation.

Table 43: Full CI Results for Oxygen Atom, cc-pVDZ Basis

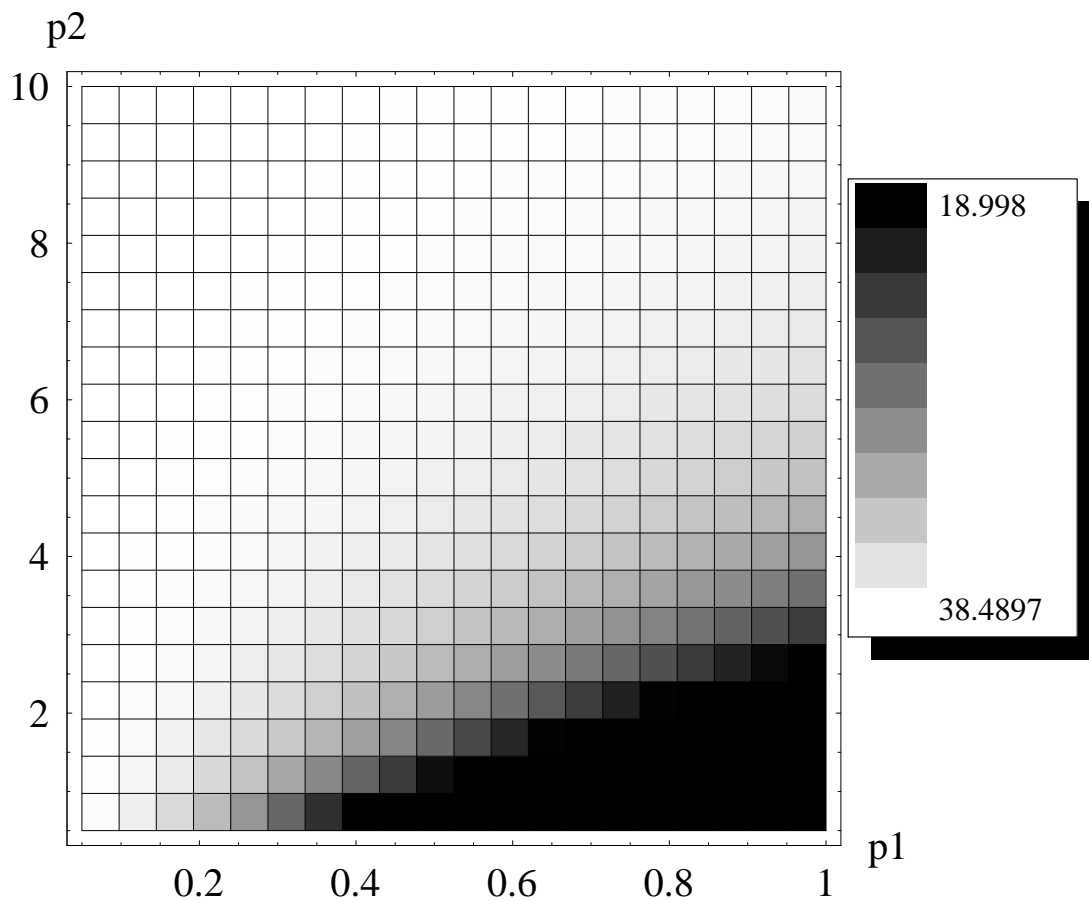
Eigenvalue	Energy(au)	Spin Quantum Number(S)
1	-74.9076668782	1.00
2	-74.9076668782	1.00
3	-74.9076651533	1.00
4	-74.3144151907	1.00
5	-74.3144151907	1.00
6	-74.3144089572	1.00
7	-73.8961915673	2.00
8	-73.8961707443	2.00
9	-73.8961707443	2.00
10	-73.8294403260	1.00
11	-73.8294047725	1.00
12	-73.8294047725	1.00
13	-73.8197705793	2.00
14	-73.7854164706	1.00
15	-73.7854164706	1.00
16	-73.7853895151	1.00
17	-73.7853895151	1.00
18	-73.7853815338	1.00
19	-73.7301128656	1.00
20	-73.7301128656	1.00
21	-73.7301004221	1.00
22	-73.7301004221	1.00
23	-73.7300923622	1.00
24	-73.7300923622	1.00
25	-73.7296367317	1.00

Table 44: DFT/MRCI Error Analysis for Oxygen Atom, cc-pVDZ Basis

$p1$	$p2$	Average error (mH)	Standard deviation of error (mH)
$0 \leq p1 \leq 1$	$0 \leq p2 \leq 10$	37.497	2.42638

In figure 19, the horizontal axis is p_1 , the vertical axis is p_2 , and the absolute error units are milli-Hartrees.

Figure 19: O Atom, cc-pVDZ Basis DFT/MRCI Absolute Error (mH) with Respect to FCI Results



B.13 Fluorine Atom, cc-pVDZ Basis

The F atom cc-pVDZ calculation had 14 basis functions. The active space used in the DFT/MRCI calculations for F was a CAS over the $2s$, $2p$, $3s$, and $3p$ orbitals. The $1s$ core electrons were frozen. No virtual orbitals were frozen. ROHF open-shell coefficients corresponding to the high-spin 2P ground state were used to generate the initial orbitals, with exchange-correlation potential integrals from an unrestricted DFT calculation.

Table 45: Full CI Results for Fluorine Atom, cc-pVDZ Basis

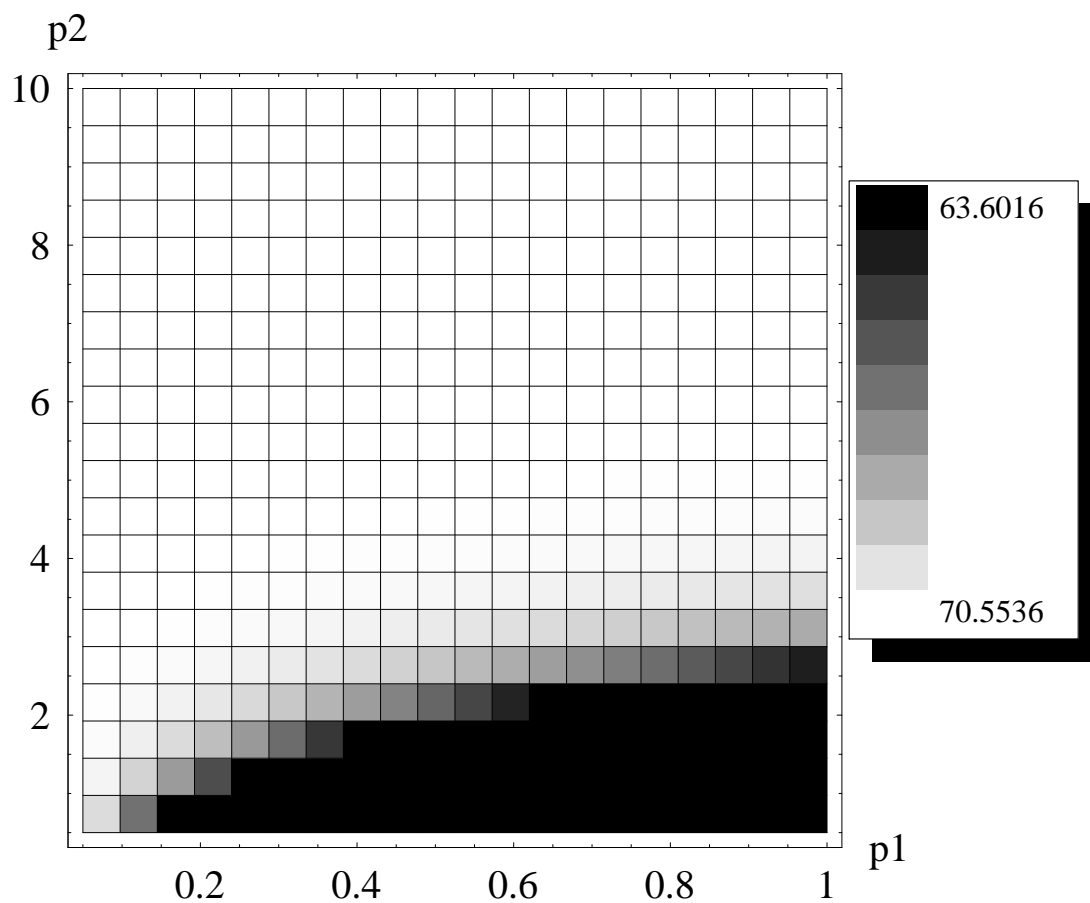
Eigenvalue	Energy(au)	Spin Quantum Number(S)
1	-99.5250149572	0.50
2	-99.5250122692	0.50
3	-99.5250122692	0.50
4	-98.7098466484	0.50
5	-98.2263496364	1.50
6	-98.2263398709	1.50
7	-98.2263398709	1.50
8	-98.1722681950	0.50
9	-98.1722404883	0.50
10	-98.1722404883	0.50
11	-98.1452591018	1.50
12	-98.1452591018	1.50
13	-98.1452580440	1.50
14	-98.1452580440	1.50

Table 46: DFT/MRCI Error Analysis for Fluorine Atom, cc-pVDZ Basis

$p1$	$p2$	Average error (mH)	Standard deviation of error (mH)
$0 \leq p1 \leq 1$	$0 \leq p2 \leq 10$	70.365	0.763109

In figure 20, the horizontal axis is p_1 , the vertical axis is p_2 , and the absolute error units are milli-Hartrees.

Figure 20: F Atom, cc-pVDZ Basis DFT/MRCI Absolute Error (mH) with Respect to FCI Results



B.14 Neon Atom, cc-pVDZ Basis

The Ne atom cc-pVDZ calculation had 14 basis functions. The active space used in the DFT/MRCI calculations for Ne was a CAS over the $2s$, $2p$, $3s$, and $3p$ orbitals. The $1s$ core electrons were frozen. No virtual orbitals were frozen.

Table 47: Full CI Results for Neon Atom, cc-pVDZ Basis

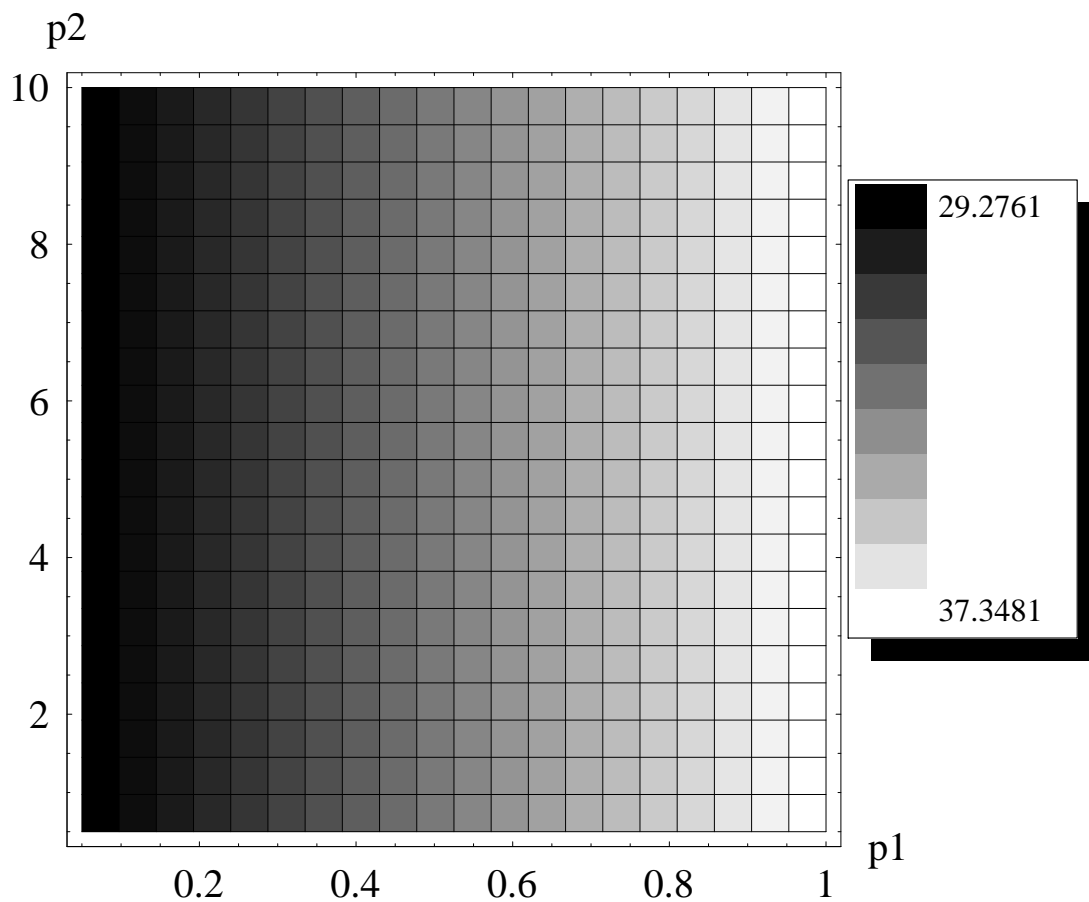
Eigenvalue	Energy(au)	Spin Quantum Number(S)
1	-128.6762641527	0.00
2	-127.0362874267	1.00
3	-126.9067374859	1.00
4	-126.9067374858	1.00
5	-126.9067374858	1.00
6	-126.9067374857	1.00
7	-126.9067374856	1.00
8	-126.8392428164	0.00
9	-126.8392428082	0.00
10	-126.8392428052	0.00
11	-126.8379777691	1.00
12	-126.8379777659	1.00
13	-126.8379777577	1.00
14	-126.8208198490	0.00

Table 48: DFT/MRCI Error Analysis for Neon Atom, cc-pVDZ Basis

$p1$	$p2$	Average error (mH)	Standard deviation of error (mH)
$0 \leq p1 \leq 1$	$0 \leq p2 \leq 10$	33.3121	2.45285

In figure 21, the horizontal axis is p_1 , the vertical axis is p_2 , and the absolute error units are milli-Hartrees.

Figure 21: Ne Atom, cc-pVDZ Basis DFT/MRCI Absolute Error (mH) with Respect to FCI Results



B.15 Beryllium Dimer, cc-pVDZ Basis

The Be dimer cc-pVDZ calculation had 28 basis functions. The active space used in the DFT/MRCI calculations for Be₂ was a CAS over the 2σ, 1π, 1π*, 2σ*, 3σ and 3σ* orbitals. The 1σ and 1σ* orbitals were frozen.

Table 49: Full CI Results for Beryllium Dimer, cc-pVDZ Basis

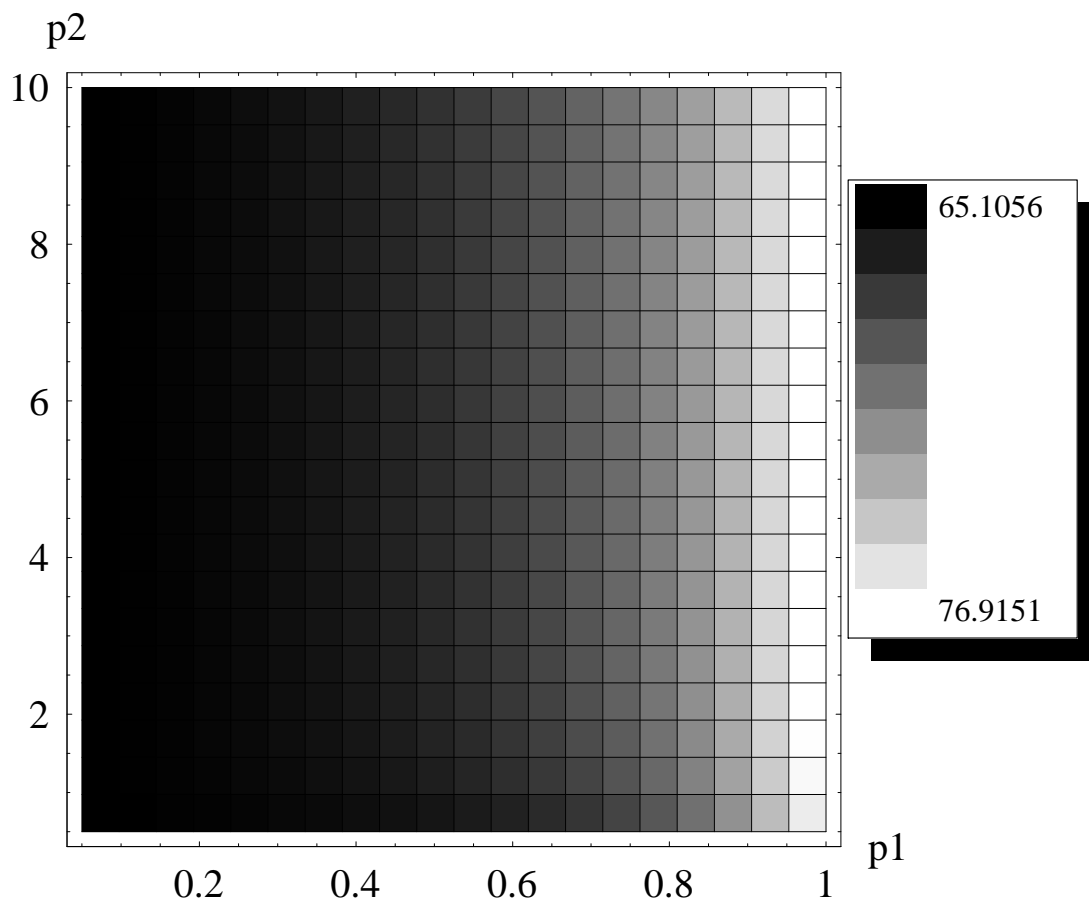
Eigenvalue	Energy(au)	Spin Quantum Number(S)
1	-29.2338409859	0.00
2	-29.1914009165	1.00
3	-29.1802291199	1.00
4	-29.1802291199	1.00
5	-29.1476359431	0.00
6	-29.1476359431	0.00
7	-29.1225304798	1.00
8	-29.1225304798	1.00
9	-29.1156678694	0.00
10	-29.1156678694	0.00
11	-29.1143923436	1.00
12	-29.1143923436	1.00
13	-29.1007032177	0.00
14	-29.0976158970	1.00
15	-29.0931147426	0.00
16	-29.0868631904	0.00
17	-29.0868631903	0.00
18	-29.0828377548	2.00
19	-29.0828377548	2.00
20	-29.0769245880	1.00
21	-29.0744258409	2.00
22	-29.0666929750	0.00
23	-29.0579750627	0.00
24	-29.0578158780	1.00
25	-29.0578158779	1.00
26	-29.0534236925	1.00
27	-29.0534236924	1.00

Table 50: DFT/MRCI Error Analysis for Beryllium Dimer, cc-pVDZ Basis

$p1$	$p2$	Average error (mH)	Standard deviation of error (mH)
$0 \leq p1 \leq 1$	$0 \leq p2 \leq 10$	-68.4936	3.41014

In figure 22, the horizontal axis is p_1 , the vertical axis is p_2 , and the absolute error units are milli-Hartrees.

Figure 22: Be Dimer, cc-pVDZ Basis DFT/MRCI Absolute Error (mH) with Respect to FCI Results



Appendix C. A Procedure for Conversion of 3s Basis Functions into Equivalent 1s Functions

One method for generating correlation-consistent double- ζ quality basis sets for use with actinides is to perform open-shell Hartree-Fock atomic calculations. This procedure results in a shell-averaged description of a particular spin-state of the atom, which facilitates a balanced description of atomic states in MR-SOCISD calculations.

Because exponent collapse can be a frequent occurrence when using 1s primitives in optimization of the exponents for heavy-element atom basis sets [20], Cartesian d functions are frequently used, with an additional symmetry adapted linear combination added to represent the 3s functions. Such functions vanish at the origin, making them quite useful with shape-consistent pseudo potentials, which go smoothly and nodelessly to zero at the origin. Exponent collapse can occur during the development of $2p$ basis functions, though not as often. In this case Cartesian f functions can be used to circumvent the exponent collapse that can occur in the exponent optimization in larger basis sets. When $2p$ function primitives are used, an extra primitive is typically added to ensure the vanishing of the derivative of the contracted function at the origin [31]. When Cartesian functions of higher principle quantum number are used ($3sd$, $4pf$, etc.), the resulting contracted functions need not have their functional behavior at the origin compensated with an additional primitive. Polarization functions are added, and the exponents are hand optimized using MR-SOCISD calculations, typically involving correlation of the $5f$ electrons for uranium. The procedure is relatively straightforward for cc-pVDZ quality basis sets, however, the hand optimization step becomes tedious when adding a second g polarization function. This tedium may be avoided or reduced via the use of even-tempered bases.

Recently, Dr. Russell Pitzer has had success developing basis sets for heavier atoms that do not use 3s functions. To develop these basis sets, he uses a modified atomic SCF program which uses a Legendre expansion method for the optimization of the primitive exponents, developed by Petersson *et al* [104]. This method results in a set of well-conditioned optimization parameters for optimization of the exponents,

and initial results on heavy atoms show that the method is more stable with respect to exponent collapse. The bromine cc-pVDZ basis set provided by Dr. Pitzer was generated using this method. The original bromine cc-pVDZ basis set developed by Dr. Jean Blaudeau used 3s primitives [21]. Unfortunately, a cc-pVDZ basis set for use with the uranium 68 electron RECP could not be generated in time for this work, and an alternate method for producing 1s functions from the 3s primitives had to be used.

C.0.0.1 Conversion of the Uranium cc-pVDZ 3s Primitives to 1s Functions By Fitting. Since attempts to reoptimize exponents for the 6s and 7s basis functions using 1s primitives results in exponent collapse when applied to the uranium +2 ion using the 68 electron RECP, an alternate method involving fitting had to be used. The basic idea behind the procedure is to obtain a set of 1s basis functions that provide a good fit to the 3s basis function orbital and radial probability density, without experiencing exponent collapse when re optimizing the primitive coefficients.

The first step in the method replaces the 3s basis functions by 1s basis functions, such that their maximum values coincide. A normalized 3s primitive has the form

$$f_{3s}(r) = N_{3s}(\alpha_{3s}) r^2 e^{-\alpha_{3s} r^2}, \quad (94)$$

while 1s primitives have the form

$$f_{1s}(r) = N_{1s}(\alpha_{1s}) e^{-\alpha_{1s} r^2}. \quad (95)$$

Differentiating equations 94 and 95 with respect to r and setting them equal yields a condition on the exponents of the 1s functions in order to match the maxima of the 3s functions of

$$\alpha_{1s} = \frac{\alpha_{3s}}{3}. \quad (96)$$

Because of the r^2 multiplicative factor, 3s functions go to zero at the origin, while 1s primitives do not. This behavior is undesirable in the 1s functions for use with RECPs, and so the first correction to this 1s basis set involves adding a tight primitive (large exponent), the sole function of which is to force the 1s basis function to go to zero at the origin. The coefficient for this primitive is determined by a linear combination of the other coefficients, satisfying the condition

$$c_0 = - \sum_{i=1}^N c_i f_{1s}(r=0). \quad (97)$$

Now that the initial set of 1s primitives has been defined by the exponent condition in equation 96 and the coefficient of the tight, canceling primitive has been determined, the conversion procedure proceeds as follows:

1. Add another 1s primitive.
2. Reoptimize all 1s coefficients in an atomic SCF calculation.
3. Determine the coefficient on c_0 from Equation 97.
4. Plot the difference in radial probability densities between the new 1s and original 3s basis function.

This procedure is repeated until a decent fit occurs, or adding an additional 1s function results in exponent collapse. The later case is typically the stopping point of the procedure. Figure 23 shows the original 3s orbital along with the converted 1s orbital formed using 10 primitives from the above procedure. Figure 24 shows the radial probability density functions of the original 3s orbital and the converted 1s orbital. Figure 25 shows the difference between the radial probability densities of the original 3s and converted 1s basis function.

Two figures of merit which measure the goodness of the fit procedure are defined for the basis set conversion. Each value measures the average deviation in the radial probability density between the original 3s function and the new 1s function over a

Figure 23: Uranium cc-pVDZ 68 Electron RECP 3sd and Converted 1s Orbitals

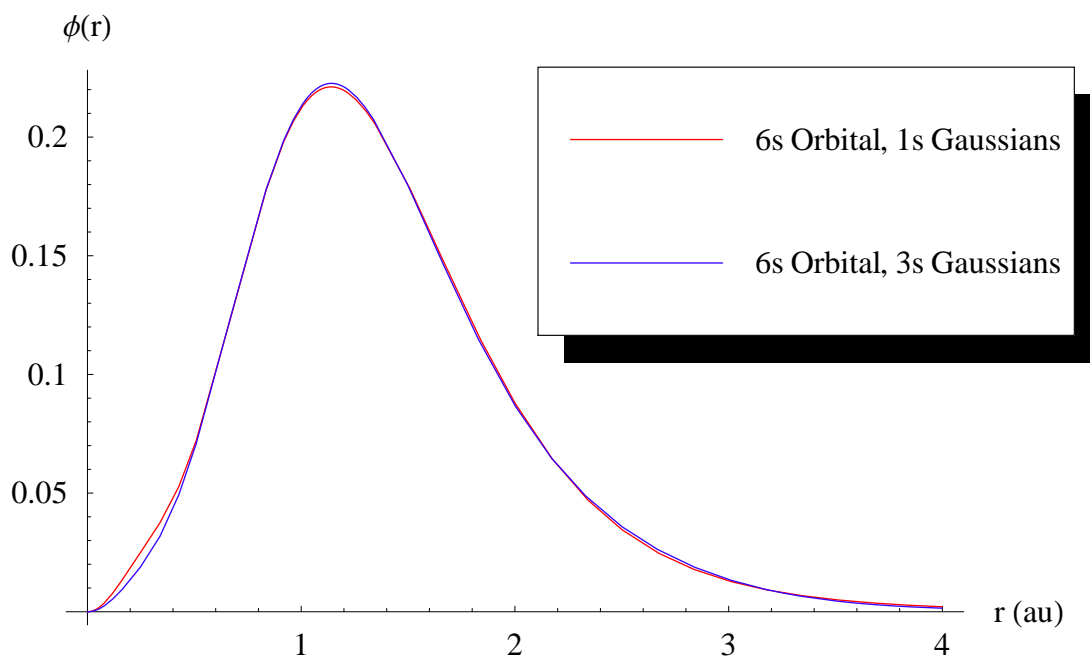


Figure 24: Uranium cc-pVDZ 68 Electron RECP 3sd and Converted 1s Orbital Radial Probability Densities

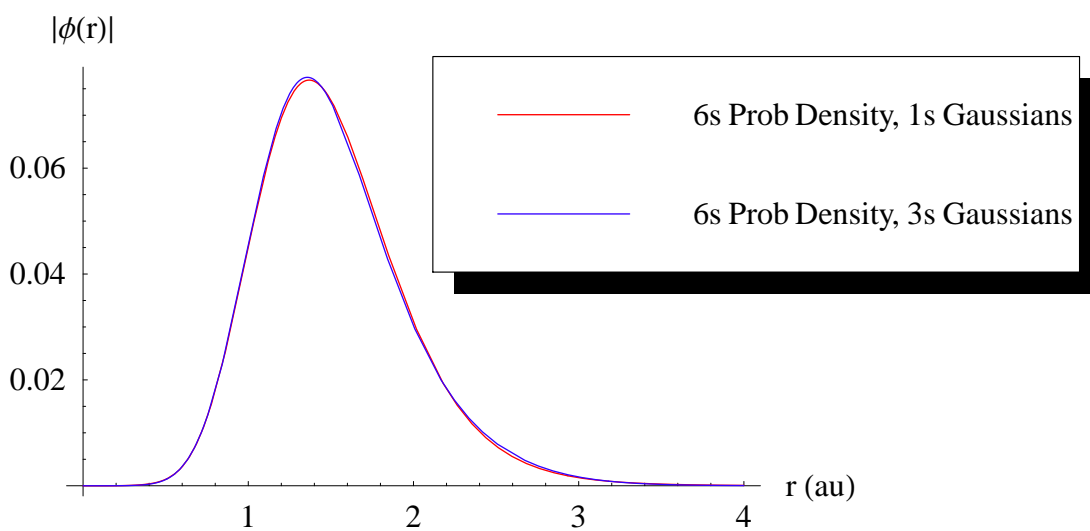
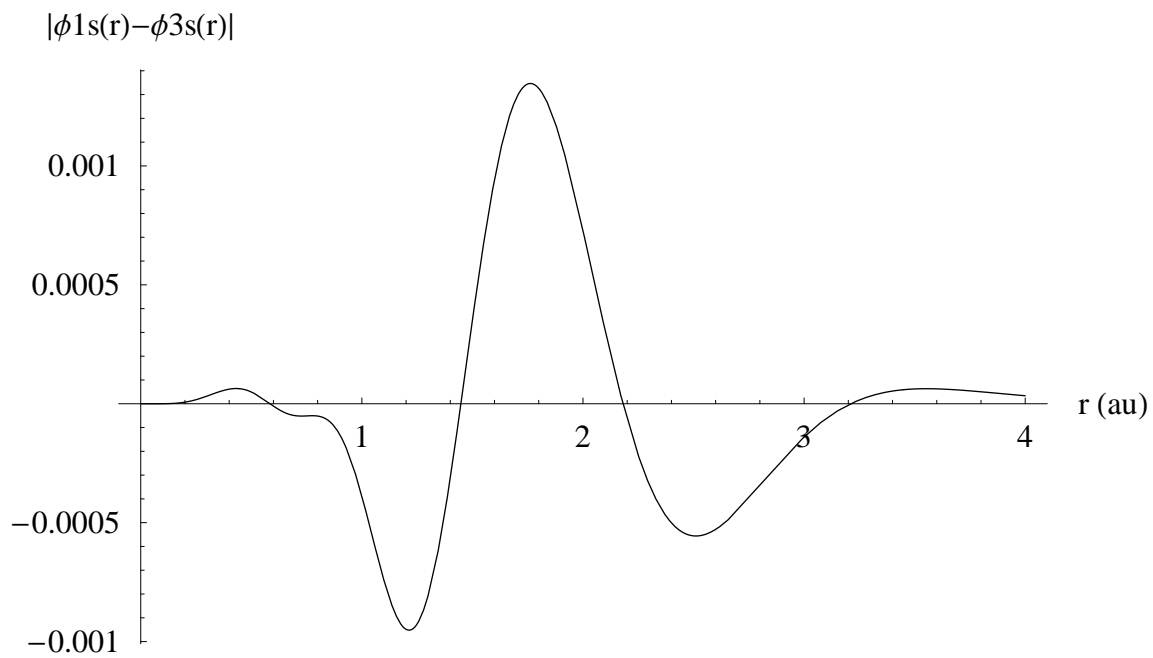


Figure 25: Uranium cc-pVDZ 68 Electron RECP 3sd and Converted 1s Radial Probability Density Difference



range of radial values. The average integrated density difference is defined as

$$AIDD = \frac{1}{b-a} \int_a^b (r^2 (\phi_{3s}^*(r) \phi_{3s}(r) - \phi_{1s}^*(r) \phi_{1s}(r))) dr, \quad (98)$$

while the average integrated absolute density difference is defined by

$$AIADD = \frac{1}{b-a} \int_a^b (r^2 |\phi_{3s}^*(r) \phi_{3s}(r) - \phi_{1s}^*(r) \phi_{1s}(r)|) dr. \quad (99)$$

The conversion procedure necessarily results in a smaller basis set than results from using $3sd$ functions. For every $3sd$ contraction, there are six symmetry adapted basis functions. These correspond to the $x^2 + y^2 + z^2$, which is the $3s$ function, and another five functions representing $3d$ functions. For example, the original $3s$ basis had four contractions. This resulted in 24 total basis functions corresponding to one contraction for the uranium $6s$ shell, one contraction for the uranium $5d$ and one contraction for the $6d$ shell, with the fourth contraction serving as a diffuse function for all three. However, each contraction in the $3sd$ basis generates six basis functions for a total of 24 functions. There are four $3s$ functions, and 20 $3d$ functions. Replacing the $6s$ contractions in the $3sd$ basis with two $1s$ contractions generates two basis functions. Additionally, removing the $3s$ symmetry adapted function removes three more functions. So, the converted $1s$ basis contains two $6s$ contractions, and three $3d$ contractions, for a total of 17 basis functions. Missing in the converted $1s$ basis set are two $6s$ basis functions and one $3d$ set, so the converted basis has seven fewer basis functions than the $3sd$ basis set. The end result of the conversion process yields a $1s$ basis set for use with the uranium 68 electron RECP, but has two fewer s functions and five fewer d functions. Since it is a smaller basis, the energetics from it will be slightly worse than the results obtained using the $3sd$ basis. This is best illustrated by looking at the MR-SOCISD results on the uranium +5 ion using both basis sets, same active spaces. Table 51 shows the excitation energies obtained from both basis sets using a $(5f)^1$ active space, while Table 52 shows the excitation energies obtained from both basis sets using all $(5f6d)^1$ references. The effect on the excitation energies

Table 51: U^{5+} Results From Both $3sd$ and $1s$ Converted Basis Set, $5f^1$ Reference Space

J	Principle <i>LS</i> Component	68e RECP cc-pVDZ $3sd$ basis (cm^{-1})	68e RECP cc-pVDZ $1s$ basis (cm^{-1})	Experiment (cm^{-1}) [17]
$\frac{5}{2}u$	$^2F_{\frac{5}{2}}^o$	0	0	0
$\frac{7}{2}u$	$^2F_{\frac{7}{2}}^o$	7560(-0.6)	7598(-0.1)	7608.6
$\frac{3}{2}g$	$^2D_{\frac{3}{2}}$	103246(+13.5)	105305(+15.7)	90999.6
$\frac{5}{2}g$	$^2D_{\frac{5}{2}}$	112030(+11.5)	113721(+13.1)	100510.5
$\frac{5}{2}u$	$^4F_{\frac{5}{2}}^o$	116683	114045	
$\frac{7}{2}u$	$^4F_{\frac{7}{2}}^o$	121025	118402	
$\frac{1}{2}g$	$^2S_{\frac{1}{2}}$	156038(+10.3)	193377(+36.7)	141447.5
RMS deviation		10.2%	21.7%	

is most clearly seen in the 2D and 2S states, where the converted $1s$ basis set has less flexibility than the $3sd$ basis. Listed below is the $1s$ converted basis for use with the uranium 68 shapte-consistent electron relativistic effective core potential, obtained from the original $3s$ basis developed by Dr. Scott Brozell. The $3sd$ notes listed below are from Dr. Brozell's development work, the other notes describe the conversion procedure.

Table 52: U^{5+} Results From Both $3sd$ and $1s$ Converted Basis Set, $(5f6d)^1$ Reference Space

J	Principle <i>LS</i> Component	68e RECP cc-pVDZ $3sd$ basis (cm^{-1})	68e RECP cc-pVDZ $1s$ basis (cm^{-1})	Experiment (cm^{-1}) [17]
$\frac{5}{2}u$	${}^2F_{\frac{5}{2}}^o$	0	0	0
$\frac{7}{2}u$	${}^2F_{\frac{7}{2}}^o$	7578(-0.4)	7615(+0.1)	7608.6
$\frac{3}{2}g$	${}^2D_{\frac{3}{2}}$	92570(+1.7)	95671(+5.1)	90999.6
$\frac{5}{2}g$	${}^2D_{\frac{5}{2}}$	101403(+0.9)	104179(+3.7)	100510.5
$\frac{5}{2}u$	${}^4F_{\frac{5}{2}}^o$	116809	114162	
$\frac{7}{2}u$	${}^4F_{\frac{7}{2}}^o$	121471	118519	
$\frac{1}{2}g$	${}^2S_{\frac{1}{2}}$	146989(+3.9)	191357(+35.3)	141447.5
RMS deviation		2.2%	17.9%	

```

! The Uranium +2 Ion      Core Potential pVDZ Correlation Consistent Set
!
! Basis Set:
! (8s4p5d4f1g)/[2s2p4d2f1g]
! modified from the u.dication.68.pvdz.sd basis developed by
! S.R. Brozell, Ph.D. Dissertation, The Ohio State University, 1999
! with a change to the most diffuse p contraction coefficients.
! The most diffuse p contraction follows the augmentation scheme of
! P.A. Christiansen, J. Chem. Phys. 112, 10070 (2000).
!
! Core Potential:
! 68 electron core.
! P.A. Christiansen
! Unpublished, Mon Nov 9 13:50 EST 1998.
!
! State: 5d(10)6s(2)6p(6)5f(2)6d(2), av. of config.
!
! Hartree-Fock Calculations
! Total HF Energy          State
! -214.13612675 5d(10)6s(2)6p(6)5f(2)6d(2), av. of config-- 3sd basis
! -214.13387918 5d(10)6s(2)6p(6)5f(2)6d(2), av. of config-- 1s basis
!
! Average integrated absolute orbital difference,
! |6s(3s) -6s(1s)| = 0.000978334, r->(0,4au)
! Average Integrated absolute orbital density difference,
! |6s(3s)-6s(1s)| = 0.00022913, r->(0,4au)
!
! (HF+1+2) Calculations -- on 3sd basis
! Total CI Energy          State          Description
! -214.30206505          5f(2)6d(2), J=6          5f(2)6d(2) Ref., 5f to 5g
! -214.28867792          5f(2)6d(2), J=4          5f(2)6d(2) Ref., 5f to 5g
!
8 1 2 / U s (8s4p5d4f1g)/[2s2p4d2f1g]
18.0 -0.00778796 0.0
5.346 0.0867051 0.0
1.5 -0.9535696 0.0
0.896 0.3974739 0.0
0.5 0.9553621 1.0
0.357 0.1838804 0.0
0.1559 0.1543360 0.0
0.05187 -0.0150411 0.0
5 3 4 / U sd (8s4p5d4f1g)/[2s2p4d2f1g]
16.040000 -0.0220355 0.0067838 0.0
2.688000 0.7136482 -0.3001085 0.0
1.071000 0.3561056 -0.0536579 0.0
0.467800 0.0172751 0.4687373 0.0
0.155600 0.0052648 0.6719109 1.0
4 2 2 / U p (8s4p5d4f1g)/[2s2p4d2f1g]
7.579000 -0.002612 0.0
1.391000 -0.3323902 0.0
0.623700 0.7835309 -0.31146
0.245300 0.4972529 1.0
4 4 2 / U f 8s4p5d4f1g)/[2s2p4d2f1g]
6.539000 0.0944382 0.0
2.443000 0.4175731 0.0
0.952000 0.4948986 0.0
0.331400 0.2716050 1.0
1 5 1 / U g (8s4p5d4f1g)/[2s2p4d2f1g]
1.645000 1.0000000

```

```

! 6s basis functions were developed from 3sd functions by using a series of avg. of config
! atomic SCF calculations. G function not reoptimized
! Starting with the 3s exponents, 1s exponents were developed by dividing the 3s exponents by 3 to
! produce 1s functions with peak densities in the same place as the 3s functions. Next, a tight primitive
! was added, with the purpose of cancelling the orbital at the origin.
! The coefficient on this exponent was calculated to force
! the orbital to go to zero at the origin. All contractions were allowed
! to relax in the atomic SCF calculation. Additional primitives were added until evidence of exponent collapse
! manifested at 9 primitives.
! 6s functions, 5 primitives (3s exponents / 3)
! HF energy = -213.92366504 au, avg integrated |delta density| = 0.00465794
! 6s functions, 6 primitives (alpha=18.0)
! HF energy = -213.93923575 au, avg integrated |delta density| = 0.00429569
! 6s functions, 7 primitives (alpha=1.5)
! HF energy = -214.13183388 au, avg integrated |delta density| = 0.00025679
! 6s functions, 8 primitives (alpha=0.5)
! HF energy = -214.13387918 au, avg integrated |delta density| = 0.00022913
! 6s functions, 9 primitives -- exponent collapse beginning to manifest in the 1.5/0.896 exponents

! 3sd basis set development notes
! The atomic set wamizing the (5sd,4p,4f)-exponents in
! Hartree-Fock calculations on the 5f(2)6d(2) av. of config., with the
! idea of obtaining a d and an f basis close to optimum for a U(II)
! or higher oxidation-state ion.
! An additional f, p, or sd primitive lowered the energy by 0.0023, 0.0015,
! or 0.0117, respectively, resulting in exponent-collapse for p or sd.
! The first, second, and third sd, the first p, and the first f contractions,
! which represent the 5d, 6s, 6d, 6p, and 5f orbitals respectively,
! were obtained from a single Hartree-Fock calculation on the above optimized
! exponents.
! The fourth sd, second p, and second f contractions, which represent the
! 6d, 6p, and 5f orbitals respectively, were obtained by freeing the most
! diffuse exponent of the respective symmetry;
! the Christiansen augmentation scheme was followed for the only
! applicable irrep, namely p.
! Thus, the valence space of 6d, 6p, and 5f is double zeta and
! the core space of 5d and 6s is single zeta.
! The polarization set was obtained by optimizing the exponent of
! a single g primitive in HF+1+2 calculations on the lowest state of
! 5f(2)6d(2), allowing for correlation of the 5f shell only.
! The energy versus g primitive curve has a shallow minimum and is
! not affected by the Christiansen augmentation scheme.

```

Bibliography

1. NIST Computational Chemistry Comparison and Benchmark Database. Technical Report, August 2005. NIST Standard Reference Database Number 101.
2. Adamo, Carlo and Vincenzo Barone. "Toward reliable density functional methods without adjustable parameters: The PBE0 model," *Journal of Chemical Physics*, 110(13) (1999).
3. Addleman, R. Shane, et al. "On-Line Speciation of Uranyl Chelates in Supercritical CO₂ by Time-Resolved Laser-Induced Fluorescence Spectroscopy," *Analytical Chemistry*, 73:1112–1119 (2001).
4. Altmann, Simon L. *Rotations, Quaternions and Double Groups*. Mineola, New York: Dover Publications, Inc., 2005.
5. Azenha, M. E., et al. "The Influence of an Effective Charge on the Uranate Luminescence in the Ordered Perovskite Structure," *Journal of Solid State Chemistry*, 101:190–194 (1992).
6. Balasubramanian, K. *Handbook on the Physics and Chemistry of Rare Earths*, 18, 29. 1994.
7. Balasubramanian, K. *Relativistic Effects in Chemistry, Part A: Theory and Techniques*. John Wiley and Sons, Inc., 1997.
8. Barandiarán, Zolia and Luis Seijo. "Quantum chemical analysis of the bond lengths in f^n and $f^{n-1}d^1$ states of Ce³⁺, Pr³⁺, Pa⁴⁺ and U⁴⁺ defects in chloride hosts," *Journal of Chemical Physics*, 119(7):3785–3790 (2003).
9. Beck, Eric V. *Theoretical Comparison of the excited electronic states of the uranyl (UO₂²⁺) and uranate (UO₄²⁻) ions using relativistic computational methods*. MS thesis, Air Force Institute of Technology, 2003.
10. Becke, A. D. "A multicenter numerical integration scheme for polyatomic molecules," *Journal of Chemical Physics*, 88(4):2547–2553 (1987).
11. Becke, A.D. *Physical Review A*, 88 (1988).
12. Becke, A.D. "Density-functional thermochemistry. III. The role of exact exchange," *Journal of Chemical Physics*, 98(7) (1993).
13. Berg, Jacqueline O., et al. "Identification of U III and U IV Lines," *Journal of the Optical Society of America*, 70(6):716–719 (1980).
14. Bethe, H. A. and E. E. Salpeter. *Quantum Mechanics of One- and Two-Electron Atoms*. Springer-Verlag, 1957.
15. Biémont, E., et al. "Relativistic Hartree-Fock and Dirac-Fock atomic structure calculations in Fr-like ions Ra⁺, Ac²⁺, Th³⁺, and U⁵⁺," *Journal of Physics B: Atomic and Molecular Optical Physics*, 37:4193–4204 (2004).

16. Bjorken, J. D. and S. D. Drell. *Relativistic Quantum Mechanics*. McGraw-Hill Book Company, 1964.
17. Blaise, Jean and Jean-François Wyart, "Selected Constants Energy Levels and Atomic Spectra of Actinides," 2004. <http://www.lac.u-psud.fr/Database/Contents.html>.
18. Blasse, G. "The Structure Sensitivity of the U⁶⁺ Ion Luminescence in Oxides," *Journal of the Electrochemical Society*, 124(8):1280–1284 (1977).
19. Blasse, G., et al. "The Luminescence of Hexavalent Uranium in Solids," *Journal of Luminescence*, 18/19:57–62 (1979).
20. Blaudeau, J.-P., et al. "Atomic Orbital Basis Sets for Use with Effective Core Potentials," *International Journal of Quantum Chemistry*, 77:516–520 (2000).
21. Blaudeau, J-P and L.A. Curtiss. "Optimized Gaussian Basis Sets for Use with Relativistic Effective (Core) Potentials," *International Journal of Quantum Chemistry*, 61:943–952 (1997).
22. Bleijenberg, K. C. "Charge transfer transitions within the octahedral uranate group," *Journal of Chemical Physics*, 73(2):617–621 (1980).
23. Brewer, Leo. "Energies of the Electronic Configurations of the Singly, Doubly, and Triply Ionized Lanthanides and Actinides," *Journal of the Optical Society of America*, 61(12):1666–1682 (1971).
24. Brooks, B. R., et al. "The Loop-Driven Graphical Unitary Group Approach: A Powerful Method for the Variational Description of Electron Correlation," *Physica Scripta*, 21:312–322 (1980).
25. Brozell, Scott R. *Spin-Orbit Configuration Interaction Calculations of Actinide and Lanthanide Systems*. PhD dissertation, Ohio State University, 1999.
26. Burns, Peter C., et al. "The Crystal Chemistry of Hexavalent Uranium: Polyhedron Geometries, Bond-Valence Parameters, and Polymerization of Polyhedra," *The Canadian Mineralogist*, 35:1551–1570 (1997).
27. Burns, Peter C., et al. "U⁶⁺ Minerals and Inorganic Phases: A Comparison and Hierarchy of Crystal Structures," *The Canadian Mineralogist*, 34:845–880 (1996).
28. Cao, X. and M. Dolg. "Theoretical prediction of the second to fourth actinide ionization potentials," *Molecular Physics*, 101(7):961–969 (2003).
29. Carnall, William T., et al. *Gmelin Handbook of Inorganic Chemistry* (8th Edition), A5. Springer-Verlag, 1982.
30. Ceperley, D. M. and B. J. Alder. "Ground State of the Electron Gas by a Stochastic Method," *Physical Review Letters*, 45(7):566–569 (1980).

31. Chrisiansen, P. A. "Basis sets in correlated effective potential calculations," *Journal of Chemical Physics*, 112(23):10070–10074 (2000).
32. Clark, Aurora E., et al. "Density and wave function analysis of actinide complexes: What can fuzzy atom, atoms-in-molecules, Mulliken, Löwdin, and natural population analysis tell us?," *Journal of Chemical Physics*, 121(6):2563–2570 (2004).
33. Clavaguéra, Carine, et al. "Modeling Complexes of the Uranyl Ion $\text{UO}_2\text{L}_2^{n+}$: Binding Energies, Geometries, and Bonding Analysis," *Journal of Chemical Physics A*, 107:4515–4525 (2003).
34. Clavaguéra, Carine, et al. "Calculation of harmonic and anharmonic vibrational wavenumbers for triatomic uranium compounds XUY," *Chemical Physics*, 302:1–11 (2004).
35. Cohen-Tannoudji, C., et al. *Quantum Mechanics, Volume I*. Hermann and John Wiley and Sons, Inc., 1977.
36. Conway, John G. and Earl F. Worden. "Isotope shift of uranium in the infrared region between 1817 and 5598 cm^{-1} ," *Journal of the Optical Society of America*, 1(6):788–794 (1984).
37. Cook, David B. *Handbook of Quantum Chemistry*. Dover Publications Inc., 2005.
38. Cordfunke, E. H. P. and D. J. W. IJdo. " α - and β - Na_2UO_4 : Structural and Thermochemical Relationships," *Journal of Solid State Chemistry*, 115:299–304 (1995).
39. de Jong, W. A., et al. "Fully relativistic correlated benchmark results for uranyl and a critical look at relativistic effective core potentials for uranium," *Theoretical Chemical Accounts*, 107:22–26 (2001).
40. den Berge, Sven Van, et al. "The Local Uranium Environment in Cesium Uranates: A Combined XPS, XAS, XRD, and Neutron Diffraction Analysis," *Journal of Solid State Chemistry*, 166:320–329 (2002).
41. Denning, R. G. *Electronic Structure and Bonding in Actinyl Ions*, 79, 217–273. Berlin: Springer-Verlag, 1992.
42. Denning, R. G., et al. "The electronic structure of the uranyl ion Part I. The electronic spectrum of $\text{Cs}_2\text{UO}_2\text{Cl}_4$," *Molecular Physics*, 32(2):419–442 (1976).
43. Denning, R. G., et al. "The electronic structure of the uranyl ion II. The electronic spectra of $\text{CsUO}_2(\text{NO}_3)_3$ and $\text{NaUO}_2(\text{CH}_3\text{COO})_3$," *Molecular Physics*, 37(4):1089–1107 (1979).
44. Denning, R. G., et al. "Covalency in the uranyl ion: A polarized x-ray spectroscopic study," *Journal of Chemical Physics*, 117(17) (2002).

45. Denning, R. G., et al. "The electronic structure of the uranyl ion III. Theory," *Molecular Physics*, 37(4):1109–1143 (1979).
46. Deurzen, C. H. H. Van, et al. "Uranium five (U V), the 1S_0 level, and a parametric analysis of the $5f^2$ configuration," *Journal of the Optical Society of America B*, 1(1):45–47 (1984).
47. Dirac, P. A. M. "The Quantum Theory of the Electron," *Proceedings of the Royal Society London, Series A*, 118:610–624 (1928).
48. Dirac, P. A. M. "The Quantum Theory of the Electron, Part II.," *Proceedings of the Royal Society London, Series A*, 118:351–361 (1928).
49. Docrat, T. I., et al. "X-ray Absorption Spectroscopy of Tricarbonatodioxouranate(V), $[\text{UO}_2(\text{CO}_3)_3]^{5-}$, in Aqueous Solution," *Inorganic Chemistry*, 38:1879–1882 (1999).
50. Dolg, Michael. *Effective core potentials*, 79, 479–508. Jülich: John von Neumann Institute for Computing, 2000.
51. Dolg, Michael and Xiaoyan Cio. *The Relativistic Energy-Consistent ab initio Pseudopotential Approach and Its Application to Lnathanide and Actinide Compounds*, 1–36. World Scientific, 2004.
52. Duch, W. "The Direct Configuration Interaction Method for General Multireference Expansions: Symmetric Group Approach," *Theoretica Chimica Acta*, 57:299–313 (1980).
53. Eliav, Ephraim and Uzi Kaldor. "Relativistic coupled-cluster method: Intrashell excitations in the f^2 shells of Pr^{3+} and U^{4+} ," *Physical Review A*, 51(1):225–229 (1995).
54. Ermler, W. C., et al. "Ab Initio Relativistic Effective Potentials with Spin-Orbit Operators. VI. Fr through Pu," *International Journal of Quantum Chemistry*, 40:829–846 (1991).
55. Fedorov, Dmitri G., et al. "An *ab initio* study of excited states of U and UF," *Journal of Chemical Physics*, 118(11):4970–4975 (2003).
56. Fefee, L. A., et al., "Clarkson Univeristy Relativistic Effective Potential Database."
57. Gagliardi, Laura and Björn O. Roos. "Uranium triatomic compounds XUY (X, Y = C, N, O): a combined multiconfigurational second-order perturbation and density functional study," *Chemical Physics Letters*, 331:229–234 (2000).
58. Gerloch, M. *Orbitals, Terms and States*. John Wiley and Sons, 1986.
59. Gill, Peter M. W., et al. "A standard grid for density functional calculations," *Chemical Physics Letters*, 209(5,6):506–512 (1993).

60. Green, Jennifer C., et al. "Electronic Structure of $M(\text{BH}_4)_4$, $M = \text{Zr, Hf, and U}$, by Variable Photon-Energy Photoelectron Spectroscopy and Density Functional Calculations," *Inorganic Chemistry*, 44:7781–7793 (2005).
61. Griffiths, Trevor R. and Vladimir A. Volkovich. "A review of the high temperature oxidation of uranium oxides in molten salts and in the solid state to form alkali metal uranates, and their composition and properties," *Journal of Nuclear Materials*, 274:229–251 (1999).
62. Grimme, Stefan. "Density functional calculations with configuration interaction for the excited states of molecules," *Chemical Physics Letters*, 259:128–137 (1996).
63. Grimme, Stefan and Mirko Waletzke. "A combination of Kohn–Sham density functional theory and multi-reference configuration interaction methods," *The Journal of Chemical Physics*, 111(13):5645–5655 (1999).
64. Han, Young-Kyu and Kimihiko Hirao. "Density functional studies of UO_2^{2+} and AnF_6 ($\text{An} = \text{U, Np, and Pu}$) using scalar-relativistic effective core potentials," *Journal of Chemical Physics*, 113(17) (2000).
65. Handy, N. C. and S. F. Boys. "Integration Points for the Reduction of Boundary Conditions," *Theoretical Chimica Acta*, 31:195–200 (1973).
66. Harrison, R. J. *Computational chemistry for nuclear waste characterization and processing: Relativistic quantum chemistry of actinides*. Technical Report, U.S. Department of Energy, 1999.
67. Herzberg, G. *Molecular Spectra and Molecular Structure I. Spectra of Diatomic Molecules*. Van Nostrand Reinhold Company, 1950.
68. Hess, Bernd A. *Valence-Only Effective Hamiltonians*, 79, 106–117. John Wiley and Associates, 2003.
69. Hoekstra, H. and S. Siegel. "Structural Studies on Li_4UO_5 and Na_4UO_5 ," *Journal of Inorganic Nuclear Chemistry*, 26:693–700 (1964).
70. Hohenberg, P. and W. Kohn. "Inhomogeneous Electron Gas," *Physical Review*, 136(3B):864–871 (1964).
71. Huber, K.P. and G. Herzberg. *NIST Chemistry WebBook*, chapter Constants of Diatomic Molecules. June 2005. NIST Standard Reference Database Number 69.
72. Ismail, Nina, et al. "Theoretical Studies of the actinides: method calibration for the UO_2^{2+} and PuO_2^{2+} ions," *Chemical Physics Letters*, 300:296–302 (1999).
73. Kaltsoyannis, N. "Relativistic Effects in organic and organometallic chemistry," *Journal of the Chemical Society, Dalton Transactions*, 1–11 (1997).
74. Kaltsoyannis, Nikolas. "Computational Study of Analogues of the Uranyl Ion Containing the $-\text{N}=\text{U}=\text{N}-$ Unit: Density Functional Theory Calculations on

- UO_2^{2+} , UON^+ , UN_2 , $\text{UO}(\text{NPH}_3)^{3+}$, $\text{U}(\text{NPH}_3)_2^{4+}$, $[\text{UCl}_4\text{NPR}_{32}]$ ($\text{R}=\text{H}, \text{Me}$), and $[\text{UOCl}_4\text{NP}(\text{C}_6\text{H}_5)_3]^-$,” *Inorganic Chemistry*, *39*:6009–6017 (2000).
75. Katz, J. J., et al. *The Chemistry of the Actinide Elements* (2nd Edition). Chapman and Hall Ltd., 196.
 76. Kleinschmidt, Martin, et al. “Spin-Orbit Coupling of DFT/MRCI Wavefunctions: Method, Test Calculations, and Application to Thiophene,” *Journal of Computational Chemistry*, *83*:824–833 (2002).
 77. Kleinschmidt, Martin, et al. “SPOCK.CI: A Multireference Spin Orbit Configuration Interaction Method for Large Molecules,” *Journal of Chemical Physics*, *124*(2006):124101 (2006).
 78. Koch, et al. *A Chemist’s Guide to Density Functional Theory* (2nd Edition). Weinheim, Federal Republic of Germany: Wiley-VCH, 2001.
 79. Kohn, W. and L. J. Sham. “Self-Consistent Equations Including Exchange and Correlation Effects,” *Physical Review A*, *140*(4A):1133–1138 (1965).
 80. Krol, D. M. and G. Blasse. “Luminescence and energy migration in Ba_2CaUO_6 ,” *Journal of Chemical Physics*, *69*(7):3124–3127 (1978).
 81. Lee, C., et al. “Development of Colle-Salvetti Correlation-energy Formula Into a Functional of the Electron Density,” *Physical Review B*, *37*(2) (1988).
 82. Lischka, Hans, et al. “High-level multireference methods in the quantum-chemistry program system COLUMBUS: Analytic MR-CISD and MR-AQCC gradients and MR-AQCC-LRT for excited states, GUGA spin-orbit CI and parallel CI density,” *Physical Chemistry Chemical Physics*, *3*:664–673 (2000).
 83. Lue, Christopher J., et al. “Electronic Spectroscopy of UO_2 Isolated in a Solid Ar Matrix,” *Journal of the American Chemical Society*, *126*:1812–1815 (2004).
 84. Mahurin, S. M., et al. “Spectroscopic determination of heterogeneities in uranyl-doped glasses,” *Journal of Non-Crystalline Solids*, *325*:70–75 (2003).
 85. Matsika, S., et al. “Electronic Structure and Spectra of Actinyl Ions,” *Journal of Physical Chemistry A*, *105*:3825–3828 (2001).
 86. Matsika, Spiridoula and Russell M. Pitzer. “Actinyl Ions in $\text{Cs}_2\text{UO}_2\text{Cl}_4$,” *J. Physical Chemistry A*, *105*:637–645 (2001).
 87. Mattsson, A. E. *Science*, *298* (2002).
 88. Messiah, A. *Quantum Mechanics*. Dover Publications, 1999.
 89. Miller, Mark L., et al. “Description and classification of uranium oxide hydrate sheet anion topologies,” *Journal of Materials Research*, *11*(12):3048–3056 (1996).

90. Miyabe, Masabumi, et al. "Total angular momenta of even-parity autoionizing levels and odd-parity high-lying levels of atomic uranium," *Journal of Physics B: Atomic, Molecular and Optical Physics*, 35 (2002).
91. Miyabe, Masabumi, et al. "Highly excited odd-parity levels of atomic uranium," *Journal of Physics B: Atomic, Molecular and Optical Physics*, 33:4957–4972 (2000).
92. Miyoshi, E., et al. *Recent Developments of Relativistic Model Core Potentials*, 37–64. World Scientific, 2004.
93. Morozov, A. M. and D. F. Smolina. "Incorporation of Uranium into Single Crystals of Tungstates with the Scheelite Structure," *Neorganicheskie Materialy*, 14(1):125–127 (1978).
94. Morozova, L. G. and P. P. Feofilov. "Temperature quenching of uranium luminescence in scheelite-type single crystals," *Optics and Spectroscopy*, 35(4):458–459 (1973).
95. M.S.Gordon and M.W.Schmidt. *Advances in electronic structure theory: GAMESS a decade later*. Amsterdam: Elsevier, 2005.
96. Mura, Michael E. and Peter J. Knowles. "Improved radial grids for quadrature in molecular density-functional calculations," *Journal of Chemical Physics*, 104(24):9848–9858 (1996).
97. Murray, Christopher W., et al. "Quadrature schemes for integrals of density functional theory," *Molecular Physics*, 78(4):997–1014 (1993).
98. M.W.Schmidt, et al. "General Atomic and Molecular Electronic Structure System," *Journal of Computational Chemistry*, 14:1347–1363 (1993).
99. Onopko, D. E., et al. "Origin of red luminescence in scheelite crystals activated with uranium," *Optics and Spectroscopy*, 38(6):658–659 (1975).
100. Palmer, Byron A. and Jr. Rolf Engleman. "Wavelengths and energy levels of doubly ionized uranium (U III) obtained using a Fourier-transform spectrometer," *Journal of the Optical Society of America B*, 1(4):609–625 (1984).
101. Pepper, M and B E Bursten. "The electronic structure of actinide-containing molecules: A challenge to applied quantum chemistry," *Chem. Rev.*, 91:719–741 (1991).
102. Perdew, John P. and Matthias Ernzerhof. "Rational for mixing exact exchange with density functional approximations," *Journal of Chemical Physics*, 105(22) (1996).
103. Perdew, John P. and Karla Schmidt. *Density Functional Theory and Its Applications to Materials*. American Institute of Physics, 2001.
104. Petersson, George A., et al. "On the Optimization of Gaussian Basis Sets," *Journal of Chemical Physics*, 118(3):1101–1109 (2003).

105. Pierloot, Kristine. "The CASPT2 method in inorganic electronic spectroscopy: from ionic transition metal to covalent actinide complexes," *Molecular Physics*, 101(13):2083–2094 (2003).
106. Pilar, Frank L. *Elementary Quantum Chemistry* (2nd Edition). Dover Publications Inc., 1990.
107. Pitzer, Kenneth S. "Relativistic Effects on Chemical properties," *Accounts of Chemical Research*, 12(8) (1979).
108. Pyykkö, P. "Relativistic Effects in Structural Chemistry," *Chemical Reviews*, 88:563–594 (1988).
109. Pyykkö, P. and J.-P. Desclaux. "Relativity and the periodic system of elements," *Acc. Chem. Res.*, 12:276–281 (1979).
110. R. Shepard, I. Shavitt, R. M. Pitzer, D. C. Comeau, M. Pepper, H. Lischka, P. G. Szalay, R. Ahlrichs, F. B. Brown, and J.-G. Zhao. "A Progress Report on the Status of the COLUMBUS MRCI Program System," *Int. J. Quantum Chem.*, 22:149–165 (1988).
111. Rabinowitch, Eugene and R. Linn Belford. *Spectroscopy and Photochemistry of Uranyl Compounds*. Pergamon Press Inc., 1964.
112. Raghavachari, K. and J. B. Anderson. "Electron Correlation Effects in Molecules," *Journal of Physical Chemistry*, 100:12960–12973 (1996).
113. Roos, B. "A New Method for Large-Scale CI Calculations," *Chemical Physics Letters*, 15(2):153–159 (1972).
114. Roothaan, C. C. J. "New Developments in Molecular Orbital Theory," *Reviews in Modern Physics*, 23:69–89 (1951).
115. Roothaan, C. C. J. "Self-Consistent Field Theory for Open Shells of Electronic Systems," *Reviews in Modern Physics*, 32:179–185 (1960).
116. Sawyer, J. O. "The crystal structure of α SrUO_{4,000}," *Journal of Inorganic Nuclear Chemistry*, 34:3268–3271 (1972).
117. Schnedier, Richard T. and Timothy E. Roxey. "Wavelengths of U III and U IV lines in the near ultraviolet," *Applied Optics*, 21(23):4204–4206 (1982).
118. Seijo, Luis and Zoila Barandiarán. "Ab initio theoretical studies on U³⁺ and on the structure and spectroscopy of U³⁺ substitutional defects in Cs₂NaYCl₆," *Journal of Chemical Physics*, 118 (2003).
119. Shavitt, I. *Annual Report on New Methods in Computational Quantum Chemistry and Their Application on Modern Super-computers*. Technical Report, NASA Ames Research Center, 1979.
120. Shavitt, I. *The Graphical Unitary Group Approach and Its Application to Direct Configuration Interaction Calculations*, 51–99. Springer-Verlag, 1981.

121. Shavitt, I. *The Unitary Group and the Electron Correlation Problem*, 279–293. 1983.
122. Shavitt, I. “The Graphical Representation in GUGA.” Unpublished lecture notes, 2005.
123. Shavitt, I. “Introduction to the Unitary Group Approach.” Unpublished lecture notes, 2005.
124. Shavitt, I. “Matrix-Element Calculus in GUGA.” Unpublished lecture notes, 2005.
125. Stoll, Hermann. “Large-core vs. small-core pseudopotentials: A case study for Au₂,” *Chemical Physics Letters*, 429:289–293 (2006).
126. Stoll, Hermann, et al. “Relativistic Energy-Consistent Pseudopotentials Recent Developments,” *Journal of Computational Chemistry*, 23:767–778 (2002).
127. Szabo, Attila and Neil S. Ostlund. *Modern Quantum Chemistry Introduction to Advanced Structure Theory*. Mineola, New York: Dover Publications, Inc., 1989.
128. Takahashi, Kazuo, et al. “Crystal Chemical and Thermodynamic Study on CaUO_{4-x}, (Ca_{0.5}Sr_{0.5}UO_{4-x}, and α -SrUO_{4-x} (x = 0 - 0.5),” *Journal of Solid State Chemistry*, 105:234–246 (1993).
129. Tanner, Peter A., et al. “Luminescence of the uranyl-ion-doped elpasolite lattice,” *Journal of Physics: Condensed Matter*, 13:189–194 (2001).
130. Tanner, Peter A., et al. “Luminescence of the uranyl-ion-doped strontium tetraborate (SrB₄O₇),” *Journal of the Physical Chemistry of Solids*, 58(7):1143–1146 (1997).
131. Tao, J. and J. P. Perdew. “Climbing the Density Functional Ladder: Nonempirical Meta-Generalized Gradient Approximation Designed for Molecules and Solids,” *Physical Review Letters*, 91(14):1464011–1464014 (2003).
132. Teterin, Yu A., et al. “Inner valence molecular orbitals and structure of the X-ray O_{4,5}(Th,U) emission spectra in thorium and uranium oxides,” *Journal of Electron Spectroscopy and Related Phenomena*, 96:229–236 (1998).
133. Teterin, Yury A., et al. “The structure of the valence electronic orbitals in uranium trioxide γ -UO₃,” *Journal of Nuclear Science and Technology*, 3:74–77 (2002).
134. Veal, B. W., et al. “X-ray photoemission spectroscopy study of hexavalent uranium compounds,” *Physical Review B*, 12(12):5651–5663 (1975).
135. Wang, Jiahu, et al. “Evaluation of $\langle S^2 \rangle$ in Restricted, Unrestricted Hartree-Fock and Density Functional Based Theories,” *Journal of Chemical Physics*, 102(8) (1995).

136. Wang, Zheming, et al. "Cryogenic Laser Induced Fluorescence Characterization of U(VI) In Hanford Vadose Zone Pore Waters," *Environmental Science and Technology*, 38:5591–5597 (2004).
137. Wanner, H. and I. Forest, editors. *Chemical Thermodynamics of Uranium*, 1. Chemical Thermodynamics. North-Holland Elsevier Science Publishers, 1992.
138. Wilson, S. *The Dirac Equation and Dirac Spectrum*, 1, 200–209. 2003.
139. Wyart, J. F., et al. "Analysis of the Spectrum of Four-Times-Ionized Uranium (U⁵⁺)," *Physica Scripta*, 22:389–396 (1980).
140. Yutsis, A. P., et al. *Mathematical Apparatus of the Theory of Angular Momentum*, 1, 390–429. 2003.
141. Zachariasen, W. H. "Crystal Chemical Studies of the 5f-Series of Elements. XXI. The Crystal Structure of Magnesium Orthouranate," *Acta Crystallographica*, 7:788–791 (1954).
142. Zhang, Z. and R. M. Pitzer *Journal of Physical Chemistry A*, 103:6880–6886 (1999).

Vita

Major Eric V. Beck graduated from Carson City High School in Carson City, Nevada in 1989. He completed a Bachelor of Science degree with a dual major in physics and mathematics at the University of Nevada, Reno in May 1993. He received his M.S. degree in Nuclear Engineering in March of 2003 from AFIT. Major Beck joined the United States Air Force in May of 1995, and was commissioned in August 1995 at Officer Training School, Maxwell Air Force Base (AFB), Alabama. His first assignment was at the Air Force Research Laboratory, Space Vehicles Directorate in the Astrodynamics branch, Kirtland AFB, lasting from October 1995 through April 1998. While stationed at Kirtland AFB, Major Beck co-authored the Orbit Analysis Software Survey. He also assisted data acquisition and analysis for high-accuracy orbit determination using angles-only data obtained from the low-cost RAVEN telescope. In addition, he functioned as the laboratory's representative to NASA Lewis Research Center's Breakthrough Propulsion Physics Steering Group. Following his assignment at Kirtland AFB, Maj Beck was assigned to the Air Force Information Warfare Center (AFIWC) at Lackland AFB, Texas. While stationed at AFIWC, Maj Beck served as a project engineer in Radio Frequency Measurements branch of the Systems and Analysis directorate. Here, he worked on test and measurement of local San Antonio radio and television signals, the MC-130H AN/APQ-170 multimode radar, and the C-130J AN/APN-241 multimode radar. Following this duty, Maj Beck moved to the Radar and Communications Analysis Flight of the 453rd Electronic Warfare Squadron, where he contributed to the Air War Over Serbia (AWOS) Radar Warning Receiver (RWR) effectiveness after-action report and C-17 collision avoidance system upgrade vulnerability analysis. He is currently serving as a Stockpile Associate for the Defense Threat Reduction Agency at Lawrence Livermore National Laboratory.

Permanent address: 2950 Hobson Way
Air Force Institute of Technology
Wright-Patterson AFB, OH 45433